

# GALAXY STRUCTURAL PARAMETERS: STAR FORMATION RATE AND EVOLUTION WITH REDSHIFT

M. TAKAMIYA<sup>1,2</sup>

Department of Astronomy and Astrophysics, University of Chicago, Chicago, IL 60637;  
 and Gemini 8 m Telescopes Project, 670 North Aohoku Place, Hilo, HI 96720

Received 1998 August 4; accepted 1998 December 21

## ABSTRACT

The evolution of the structure of galaxies as a function of redshift is investigated using two parameters: the metric radius of the galaxy ( $R_\eta$ ) and the power at high spatial frequencies in the disk of the galaxy ( $\chi$ ). A direct comparison is made between nearby ( $z \sim 0$ ) and distant ( $0.2 \lesssim z \lesssim 1$ ) galaxies by following a fixed range in rest frame wavelengths. The data of the nearby galaxies comprise 136 broad-band images at  $\sim 4500 \text{ \AA}$  observed with the 0.9 m telescope at Kitt Peak National Observatory (23 galaxies) and selected from the catalog of digital images of Frei et al. (113 galaxies). The high-redshift sample comprises 94 galaxies selected from the Hubble Deep Field (HDF) observations with the *Hubble Space Telescope* using the Wide Field Planetary Camera 2 in four broad bands that range between  $\sim 3000$  and  $\sim 9000 \text{ \AA}$  (Williams et al.).

The radius is measured from the intensity profile of the galaxy using the formulation of Petrosian, and it is argued to be a metric radius that should not depend very strongly on the angular resolution and limiting surface brightness level of the imaging data. It is found that the metric radii of nearby and distant galaxies are comparable to each other. The median value of the radius of the local sample is  $\langle R_\eta \rangle \sim 5 \pm 1 \text{ kpc}$ , and the median radius of the HDF sample is  $\langle R_\eta \rangle \sim 6 \pm 2 \text{ kpc}$  for  $q_0 = 0.5$ ,  $H_0 = 65 \text{ km s}^{-1} \text{ Mpc}^{-1}$ ; however, for  $q_0 = 0.1$ ,  $\langle R_\eta \rangle \sim 7 \text{ kpc}$  and for  $q_0 = 1$ ,  $\langle R_\eta \rangle \sim 5 \text{ kpc}$ . In the HDF, galaxies with redshifts larger than  $z > 0.6$  have flatter  $R_\eta$  distributions than galaxies with redshifts smaller than  $z \leq 0.6$ . However, the median  $R_\eta$  values of high- and low-redshift galaxies are consistent with each other. This result is consistent with the simulations of galaxy images at redshifts  $z = 0.35$ ,  $z = 0.5$ , and  $z = 0.9$ , which show that the metric sizes can be recovered within  $\pm 2 \text{ kpc}$ .

The flocculency or power at high spatial frequencies is quantified using a simple method that is based on surface photometry in one band and that depends on the size of the star-forming regions and on the intensity profile of the galaxy. In nearby galaxies, the flocculency is found to trace the star formation rate as  $\chi$  is correlated with optical colors ( $B - V$ ) and the strength of the hydrogen recombination lines ( $H\alpha$ ).

In the HDF, galaxies at redshifts smaller than  $z \sim 1$  and with fluxes brighter than  $B = 25$  have values of  $\chi$  similar to what is measured in nearby galaxies and to what is expected from simulations of distant galaxy images. Among the HDF galaxies, I find that at most 4% can be identified as dwarf galaxies with rates of star formation similar to NGC 4449 and NGC 1569. Most HDF galaxies are giants with star formation rates similar to those in nearby giant galaxies.

In summary, in this study I have introduced a method to measure the metric sizes and flocculency of the two-dimensional light distribution of galaxies. As a result, I find that the high spatial frequency power is related to the star formation rate. Further, I find that the sizes and power at high spatial frequencies of HDF galaxies remain largely unchanged between the present epoch and redshifts lower than  $z \sim 1$ .

*Subject headings:* galaxies: evolution — galaxies: fundamental parameters — galaxies: photometry — galaxies: structure

## 1. INTRODUCTION

Studies of the origin and nature of galaxies to constrain their evolution with cosmological time have focused primarily on deep multiwavelength photometric surveys, spectroscopic follow up, and on extensive modeling of the stellar content of galaxies (see reviews of Koo & Kron 1992; Ellis 1997, and references therein). The results show a large population of blue galaxies that exceeds the no-evolution prediction by a factor of 2 at  $B \sim 22 \text{ mag}$  and by a factor of up to 10 at  $B \sim 25 \text{ mag}$ . Given that the galaxies responsible

for the faint blue excess have apparent sizes typically of  $1''$ , a detail study of their morphologies had to await the delivery by the *Hubble Space Telescope* (HST) of subarcsecond resolution images.

In the context of galaxy counts, galaxy morphology has provided new insight to the problem of galaxy evolution (Glazebrook et al. 1995; Naim et al. 1995a; Abraham et al. 1996a; van den Bergh et al. 1996; Odewahn et al. 1996; Driver et al. 1998). By 1995, the morphologically segregated galaxy counts out to  $B \lesssim 25 \text{ mag}$  were interpreted as most of the evolution occurring in irregular galaxies, particularly in dwarf galaxies undergoing high rates of star formation (Glazebrook et al. 1995; Babul & Ferguson 1996). By 1998, the morphologically split galaxy counts out to  $B \lesssim 29 \text{ mag}$  suggest that the evolution of galaxies is due to a population of high-redshift spiral galaxies and that very few *true* irregu-

<sup>1</sup> Submitted in partial fulfillment of the requirements for the degree of Doctor of Philosophy, The University of Chicago.

<sup>2</sup> Visiting Astronomer, Kitt Peak National Observatory. KPNO is operated by AURA, Inc. under contract to the National Science Foundation.

lars are responsible for the faint blue galaxy excess (Driver et al. 1998; Ferguson & Babul 1998).

Although galaxy morphological classification is commonly used, we do not yet have a unified physical interpretation for the various shapes of galaxies and we cannot yet unambiguously classify the morphologies of galaxies (which depend on observed wavelength, inclination angle, and number of resolution elements across the image). Much as the classification of stellar spectra reflects primarily a sequence in temperature, if the properties chosen to define a classification system are relevant, the underlying physical processes controlling the morphology of galaxies may be revealed. This paper develops a technique designed to measure an image structural parameter, namely, the power at high spatial frequencies (hereafter referred to as  $\chi$ ) and attempts to give a simple physical interpretation to it.

To this date many galaxy classification systems have been proposed (see Sandage 1975 for a review). The systems in use today are all in some way related to the Hubble classification whose criteria for spirals are (1) “the relative size of the unresolved nuclear region,” (2) “the extent to which the arms are unwound,” and (3) “the degree of resolution in the arm” (Hubble 1926). Conventional classification is generally done by visually assessing each one of the above properties in the photometric  $B$  band.

A number of considerations must be taken into account when assigning morphological types and interpreting the results. First, the optical appearance of a galaxy is a strong function of wavelength. Galaxies that look regular at  $\sim 4500 \text{ \AA}$  where the morphological classification systems have been established can appear abnormal when observed in the rest frame UV (Giavalisco et al. 1996; O’Connell & Marcum 1997), which is often the rest frame wavelengths where distant galaxies are observed. Unless we know and account for the redshifts when classifying distant galaxies we will be comparing morphologies at different rest frames and there will be a bias toward identifying higher redshift galaxies as *irregular* types as the observed spectra map onto progressively shorter rest frame wavelengths. Second, the sample of galaxies used in the conception of the Hubble system contained galaxies of mostly *spiral* and *elliptical* types. The number of *irregular* galaxies available when the Hubble classification was devised did not exceed 3% (Hubble 1926), and even in the Revised Shapley-Ames Catalog of Bright Galaxies (RSA) (Sandage & Tammann 1981), which currently defines the morphological types, irregular galaxies amount to less than 5%. In contrast, when reaching faint surface brightness limits, dwarf irregulars dominate the volume (Tammann, Yahil, & Sandage 1979), and when probing galaxies at high redshifts with high angular resolution, irregular galaxies become still more numerous (Driver et al. 1995; Glazebrook et al. 1995; Abraham et al. 1996a; van den Bergh et al. 1996). The Hubble classification scheme was not intended to exploit the morphological properties of irregular galaxies.

### 1.1. Quantifying Galaxy Morphology

Recent classifications of galaxies into morphological types have proven to be particularly subjective. For instance, Naim et al. (1995b) and Abraham et al. (1996a, 1996b) had a sample of galaxies classified into Hubble types by a number of independent experts. The study of Naim et al. involved a sample of 831 galaxy scans made with the Automated Plate Measuring (APM) machine. The galaxies

that had typically magnitudes  $B \leq 17$  mag, and apparent diameters  $0.5 \geq D \geq 2'$  were classified by six experts. In a slightly different experiment, Abraham et al. (1996a, 1996b) had two experts classify a sample of 507 galaxies imaged with the *HST* with  $I < 22$  mag,  $0.2 < D < 4''$ , redshifts in the range  $0.1 < z < 0.6$ . In both studies there is agreement on average within roughly 2–3 Hubble types among the different classifiers. Most of the disagreement is found among images of either edge-on galaxies (inclination angles  $i \gtrsim 60^\circ$ ) or among galaxies of *irregular* and *peculiar* types ( $T > 7$ ). The limitations of the Hubble system in classifying irregular galaxies are especially evident when applied to distant galaxies. At redshifts above  $z \sim 0.4$  and  $I > 21$  most of the population of galaxies has been classified as irregulars, interacting, or merger systems including new classes such as the “blue nucleated galaxies” (Schade et al. 1996) and “chain galaxies” (Cowie, Hu, & Songaila 1995). As a result, the population responsible for the excess blue counts down to those limits has been identified as galaxies undergoing enhanced star formation (Dressler et al. 1994; Glazebrook et al. 1995; Abraham et al. 1996a). At even fainter flux limits  $I < 26$  and larger redshifts  $z \sim 1.5$ , the excess population has been identified with starbursting dwarfs and the precursors of present-day spirals (Driver et al. 1998). It is, then, unfortunate that visual classification of faint galaxies into irregular types has proven to be particularly subjective (Abraham et al. 1996b) and that Artificial Neural Networks classification is prone to failure (Naim et al. 1995a, 1995b). Perhaps part of the answer to the problem of interpreting distant galaxy images lies in the very fact that the classification of galaxies at high redshifts is not the same task as the classification at low redshifts.

Despite the shortcomings of galaxy classification mentioned above, Hubble morphological types are correlated, although with much scatter, with a number of global properties. The revised Hubble types correlate with the surface brightness,  $UBV$  colors, H I content, and H $\alpha$  emission (Buta 1992; Kennicutt 1992). Of special interest for galaxy evolution studies are the correlation between the composite spectral class and the relative size of the bulge and the disk (Morgan & Mayall 1957), and the correlation between the integrated  $UBV$  colors and the presence of tails, wisps, and bridges in disks (Larson & Tinsley 1978). However, a number of counterexamples exist. Far-infrared data reveal that early and late-type *spiral* galaxies span essentially the same range of massive star formation rates (SFRs; Devereux & Young 1991; Devereux & Hameed 1997). Optical data of clusters of galaxies reveal evidence for misleading morphological classifications suggesting that environment plays a decisive role in masking their *true* Hubble types (Abraham et al. 1994; Caldwell et al. 1996; Koopmann & Kenney 1998).

Motivated by the recent images of distant galaxies from *HST*, a number of groups have attempted to revise conventional galaxy classification systems to objectively classify galaxies at high redshifts (Naim et al. 1995a; Abraham et al. 1996b; Odewahn et al. 1996; Bouwens, Broadhurst, & Silk 1998a, 1998b). Two of the three Hubble classification criteria have been reexamined and extensively studied on a quantitative basis. The relative size of the bulge and the disk (Hubble’s criterion 1), usually referred to as the concentration index (CI), is reflected in the fractional flux within two predefined radii (Okamura, Kodaira, & Watanabe 1984; Kent 1985; Doi, Fukugita, & Okamura 1993; Abraham et

al. 1996b). The properties of the disks of galaxies have been studied mainly in terms of the spiral pattern (criterion 2) (Elmegreen & Elmegreen 1990). The knotty, scabrous appearance of the disk (criterion 3), however, has remained mostly unexplored. A parameter like the high spatial frequency power gives the associated structure a simple physical interpretation. As previously mentioned, the apparent structure of galaxies can be dramatically shaped by the presence of star formation within giant H II regions. This leads us to seek structural parameters that can be related to the present star formation rate to study directly the interplay between star formation and morphology.

### 1.2. Star Formation Indices

The most widely used method to estimate the star formation rate in galaxies is measuring H $\alpha$  emission. From the strength of the Balmer line, one can infer the total rate of Lyman continuum photons produced by the present stellar population (Osterbrock 1989). The Lyman continuum flux provides an estimate of the total number of massive stars ( $M > 10\text{--}15 M_{\odot}$ ). By assuming an initial mass function (IMF), the number of massive stars can be related to the total number of stars and, if the star formation rate has been constant over the lifetime of observed massive stars ( $\lesssim 10^7$  yr), one can infer the current star formation rate in units of  $M_{\odot} \text{ yr}^{-1}$ . Star formation rates range from essentially zero in quiescent galaxies to over  $100 M_{\odot} \text{ yr}^{-1}$  in luminous starburst galaxies (Kennicutt 1993). In our Galaxy, the present star formation rate is between  $\sim 3$  and  $10 M_{\odot} \text{ yr}^{-1}$  (Rana & Wilkinson 1986) based on the Lyman continuum photon flux of giant H II regions (Smith, Mezger, & Biermann 1978) and on supernova remnants and pulsars (Lacey & Fall 1985). Measurements of H $\alpha$  emission in nearby galaxies indicate star formation rates of  $0.1\text{--}1 M_{\odot} \text{ yr}^{-1}$  in S0–Sa to  $10 M_{\odot} \text{ yr}^{-1}$  in Sc–Irr galaxies (Kennicutt 1983); however, each type of galaxy covers a range in star formation rate.

The picture is that early-type galaxies had most of their star formation occurring in the past, whereas late-type galaxies have a star formation rate that has been on average constant with time with some cases showing evidence for a higher star formation rate in the present than in the past (Kennicutt 1983; Gallagher, Hunter, & Tutukov 1984; Sandage 1986; see, however, Kauffmann & Charlot 1998). What regulates such a difference in the star formation at early epochs? What maintains or quenches star formation at the present epoch? How can we explain the wide range in inferred star formation rates? Features in the structure of galaxies that directly relate to the star formation rate may help reveal the mechanisms that determine the thresholds of onset of star formation. One of the goals in this study is to show that the high spatial frequency power is empirically correlated with optical star formation indices.

When a galaxy is undergoing significant star formation, the light at optical wavelengths will be dominated by early-type stars and emission from gas. The most prominent morphological features will be the star-forming regions. The most widely used optical star formation rate indices are *UBV* colors and emission-line spectra. Integrated *UBV* colors measure the overall slope of the spectral energy distribution. They are sensitive to the presence of OB stars and their flux contribution can be used to estimate star formation rates (Quirk & Tinsley 1973; Searle, Sargent, & Bagnuolo 1973). For example, Larson & Tinsley (1978)

modeled how a galaxy's colors would change if it suddenly underwent a burst of star formation. These models show that normal galaxies have *UBV* colors that are consistent with monotonically decreasing SFRs, the duration of which is longer than  $5 \times 10^8$  yr. In contrast, the colors of peculiar galaxies have a large scatter and can be consistent with bursts of durations as short as  $\sim 2 \times 10^7$  yr involving as much as  $\sim 5\%$  of the total mass (Larson & Tinsley 1978).

Star formation rates are also commonly estimated from measurements of the H $\alpha$  emission. The Balmer emission traces the luminosity of high-mass stars ( $10\text{--}15 M_{\odot}$ ), which contribute to less than  $\sim 4\%$  to the total stellar mass of a Miller & Scalo initial mass function (Miller & Scalo 1979). Therefore to estimate the total mass involved in a star formation episode, the shape of the IMF at high masses has to be known, which has, however, large sources of uncertainty.

In addition to the uncertainties of the IMF, another source of uncertainty in the determination of the star formation rate is the extinction by dust. Dust extinction can absorb and scatter Lyman continuum photons before they cascade to H $\alpha$  photons. The near-infrared (NIR) hydrogen recombination lines in the Paschen and Brackett series can help in estimating the effects of dust extinction. However, because the strength of Pa $\alpha$  at gas temperatures in the range  $2000\text{--}25,000$  K is 6–10 times lower than that of H $\alpha$ , and because of the underlying continuum of A and B type stars, the NIR line strength is expected to be very small in normal galaxies and only measurable with high-resolution near-infrared spectroscopy (Calzetti 1997).

The integrated spectra of galaxies provide diagnostics of their stellar content and SFR. Emission lines of H $\alpha$   $\lambda 6563$ , H $\beta$   $\lambda 4861$ , [O II]  $\lambda 3727$ , and [O III]  $\lambda 5007$  have been measured and interpreted as tracers of the formation rate of massive stars in galaxies (Hunter, Gallagher, & Rautenkrantz 1982; Kennicutt 1983; Gallagher et al. 1984; Gallagher, Bushouse, & Hunter 1989; Kennicutt 1992; Kennicutt, Tamblyn, & Congdon 1994; Calzetti 1997). At redshifts beyond  $z \sim 0.5$  H $\alpha$  appears at wavelengths longer than  $1 \mu\text{m}$ , and measuring SFR with H $\alpha$  in galaxies at such large redshifts requires the use of near-infrared capabilities (see, e.g., Manucci & Beckwith 1995) or the use of other emission lines sensitive to SFR: H $\beta$   $\lambda 4861$  (Hunter et al. 1982; Gallagher et al. 1984, 1989) and [O II]  $\lambda 3727$  and [O III]  $\lambda 5007$  (e.g., Kennicutt 1994). The general trend is an increase in the scatter between H $\alpha$  and the lines mentioned above mainly due to the decrease in the line fluxes in the latter (Kennicutt et al. 1994).

Since star formation regions play an important role in a galaxy's morphology, the star formation rate and the galaxy's morphology may be intimately related. In this paper, I explore a morphological index, the high spatial frequency power ( $\chi$ ), which is related to the lumpiness or flocculency. One of the goals is to define  $\chi$  so that it differentiates objectively between galaxies containing low and high star formation rates and provides some order within the classification of irregular type galaxies. The final goal is to measure the metric sizes and  $\chi$  in nearby and distant samples of galaxies and look for variations in the structural parameters as a function of redshift.

In § 2 I present the observations, data reduction, and analysis of the nearby and distant galaxy samples. In § 3 I discuss the metric radius and present the definition of the structural parameter  $\chi$  used. In § 4 I present the result of  $\chi$  obtained in the HDF. In § 5 I present simulations of images

of galaxies seen at high redshifts to compare with the observed  $\chi$  values.

Throughout this paper, I use  $H_0 = 65 \text{ km s}^{-1} \text{ Mpc}^{-1}$  and  $q_0 = \frac{1}{2}$  unless otherwise stated.

## 2. DATABASES

### 2.1. Nearby Galaxies

#### 2.1.1. Data and Observations

The sample of nearby galaxies was taken from the publicly available Catalog of Digital Images (CDI) of Frei et al. (1996) and from observations with the 0.9 m telescope at Kitt Peak National Observatory (KPNO), hereafter the KPNO sample. The CDI contains images of 113 galaxies that are intended to span the full range of early and late-type galaxies with Hubble types between  $T = -5$  and  $T = 6$ . The CDI galaxies have heliocentric velocities smaller than  $\sim 3000 \text{ km s}^{-1}$ , total apparent  $B$ -band magnitudes smaller than  $B_T \simeq 13$ , and isophotal diameters  $D_{25}$  at a surface brightness level of  $\mu_B = 25 \text{ mag arcsec}^{-2}$  greater than  $100''$  as taken from the Third Reference Catalog of Galaxies (RC3; de Vaucouleurs et al. 1991). In the CDI, 31 galaxy images are in the Thuan-Gunn *gri* photometric bands (Thuan & Gunn 1976) with a pixel scale of  $1''.19 \text{ pixel}^{-1}$ , an instrumental gain of  $g = 2e^- \text{ ADU}^{-1}$  (analog-to-digital units), and readout noise of  $9e^-$ , and 82 galaxies are in the  $B_J R$  bands of the photometric system of Gullixson et al. (1995) with a pixel scale of  $1''.35 \text{ pixel}^{-1}$ , an instrumental gain of  $g = 11e^- \text{ ADU}^{-1}$ , and readout noise of  $90e^-$ . For a complete description of the observations see Frei et al. (1996). The images of both sets are well resolved with pixel scales sampling 20–300 pc. Only the Palomar data were obtained under photometric conditions.

Unlike the CDI sample, which was meant to represent the generic early and late Hubble morphological types and included only five galaxies with types  $T > 7$ , the KPNO sample was selected for their irregular morphologies. It includes 23 *irregular* galaxies, eight of which were selected from the Arp Catalog of Peculiar Galaxies (Arp 1966), seven from the list of Kennicutt (1992), and seven from the list of Gallagher et al. (1989). As an internal check, NGC 2403, a galaxy in the CDI sample, was included in the KPNO observations. Unfortunately, it was possible to observe only this one galaxy in common due to weather conditions during the run. The galaxies selected from the Arp Catalog have distorted morphologies and no companion galaxies. The galaxies selected from the list of Kennicutt have equivalent widths (EW) of  $\text{H}\alpha + [\text{N II}] > 35 \text{ \AA}$ , and from the list of Gallagher et al. have  $\text{H}\beta \text{ EW} > 9 \text{ \AA}$  ( $\text{H}\alpha + [\text{N II}] \gtrsim 84 \text{ \AA}$ ). Essentially, the KPNO sample was meant to augment the CDI with galaxies having signs of especially active star formation.

The images of the KPNO sample were observed during four consecutive nights between 1997 September 7 and 10 using the 0.9 m telescope in the Johnson  $BR$  photometric bands under nonphotometric conditions. Here I will only report on the results obtained with the  $B$ -band data. The galaxies were observed with the direct camera at  $f/7.5$  (Massey et al. 1996) with a field of view of  $23''.2 \times 23''.2$ , which when projected on the  $2048 \times 2048$  Tektronix CCD (T2KA) in the Cassegrain focus yields a scale of  $0''.68 \text{ pixel}^{-1}$ .

The instrumental gain was set at  $3.6e^- \text{ ADU}^{-1}$  with an expected readout noise of  $4e^-$ . Although the readout noise

was measured to be higher ( $9e^-$ ) than the nominal value, it remains much lower than the photon noise and does not affect our final measurements. The reason for this discrepancy was not known at the time this work was done (W. Schoening 1997, private communication). Exposure times of 10–15 minutes in the  $B$  band rendered typical sky levels between 600 and 900 ADU and total signal-to-noise ratios of the source larger than  $\sim 100$ . Owing to the non-photometric conditions flux calibration frames were not observed. The seeing, determined as the point-spread function (PSF) full width at half-maximum (FWHM) from stars in the field of view of the galaxy images, ranged from  $1''.41$  to  $1''.77$ .

Data reduction was done with IRAF<sup>3</sup> following recommended procedures (Massey 1997). The images were processed by choosing the overscan region on flat-field frames between columns 2052 and 2078 and subtracting a fitted vector of the overscan to each column of the images. Next all the zero dark exposure frames within each night were combined and subtracted from each image to correct for any residual bias level. To correct for variations in the response of each pixel, a master flat-field image was constructed from the median of one night's worth of flat fields and each object frame was divided by its corresponding master flat frame. Either dome flats or twilight flats were used to create the  $B$ -band flat field. When available, twilight flats were used, but most of the flat-field corrections were done with dome flats due to the cloudy conditions at dawn and dusk during the observations. The pixel-to-pixel variations in the flat frame images amount to less than 2%. The final images have gradients in the sky level of less than 0.1% across the field of view. The large dynamic range of the KPNO CCD of 65,535 ADU, which deviates from linearity at the 0.1% level at  $\sim 50,000 \text{ ADU}$ , ensured that, unlike the CDI, the images of the cores of the galaxies remain unsaturated.

Foreground stars were removed from each frame by constructing a point-spread function model from selected stellar objects within the image frame off the galaxy and scaling this model to account for the flux of each pointlike object. To a certain degree the selection of foreground stars is arbitrary. For example, the number of stars identified in the field of NGC 2403 in the CDI and KPNO sample differ from each other in the sense that Frei et al. (1996) find more foreground stars than I do. In many cases the disputed overlapping objects have FWHM larger than that of a point source and in one case (NGC 2403) these have been identified spectroscopically to be globular clusters at the galaxy (Battistini et al. 1984), which suggests that in other cases too they are part of the galaxy and not foreground stars. Although there is a fair amount of uncertainty in cleaning the galaxy image of foreground stars, the resulting difference in  $\chi$  is minimal at this level. Nevertheless, it is important to note that the excision of foreground stars is not trivial.

#### 2.1.2. Nearby Sample Characteristics

In Figure 1, the  $B - V$  color distribution of the complete sample of nearby galaxies is compared to that of the RC3 and Takamiya, Kron, & Kron (1995). The RC3 and Taka-

<sup>3</sup> IRAF is distributed by the National Optical Astronomy Observatories, which are operated by the Association of Universities for Research in Astronomy, Inc., under cooperative agreement with the National Science Foundation.

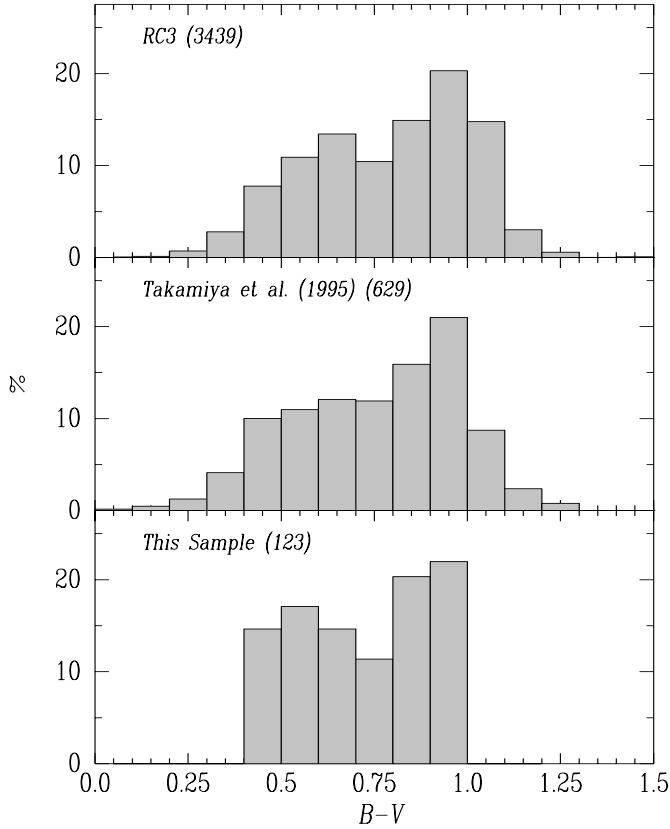


FIG. 1.— $B-V$  color distribution of nearby galaxies. *Top*: Subsample of RC3 galaxies with  $12 \leq B_T < 14$ . *Middle*: Subsample of Zwicky catalog galaxies with  $14 \leq B < 16$ . *Bottom*: CDI and KPNO samples used in this study. The total number of galaxies is given in parentheses.

miya et al. (1995) color distributions are argued to be representative in the local universe. The main difference between the  $B-V$  color distributions is that the CDI + KPNO contains no galaxies at both extremes in  $B-V$ : very red and very blue galaxies are missing. The galaxies in the CDI + KPNO sample were selected to define a complete morphological sample of nearby galaxies. This means that galaxies that are located nearby and that are bright were more likely to be included in the CDI + KPNO. The reasons for the lack of extreme  $B-V$  color galaxies in the CDI + KPNO sample are different at each end. At the blue end, the galaxies are missing because they are of very low surface brightness and therefore they become difficult to image at a sufficient signal-to-noise level to be useful for morphological classification. At the red end galaxies are missing because very red galaxies lie mostly within galaxy clusters, and at the flux levels reached by the CDI + KPNO there are only a few rich clusters. Assuming that galaxies at both extremes in  $B-V$  contribute very little to the total star formation rate in the local universe, the CDI + KPNO should suffice to explore the rate of star formation taking place locally.

Figure 2 shows the  $UBV$  colors of a subsample of galaxies of the CDI and KPNO observations. Plotted in Figure 2 are the total color indices  $[(U-B)_T^0]$  and  $[(B-V)_T^0]$  corrected for differential galactic and internal extinction and for redshift. The  $(U-B)_T^0$  and  $(B-V)_T^0$  colors refer to zero extinction in our Galaxy, zero extinction inside the galaxy (“face-on”), and zero redshift. The number of data points plotted is smaller than the number of galaxies in the

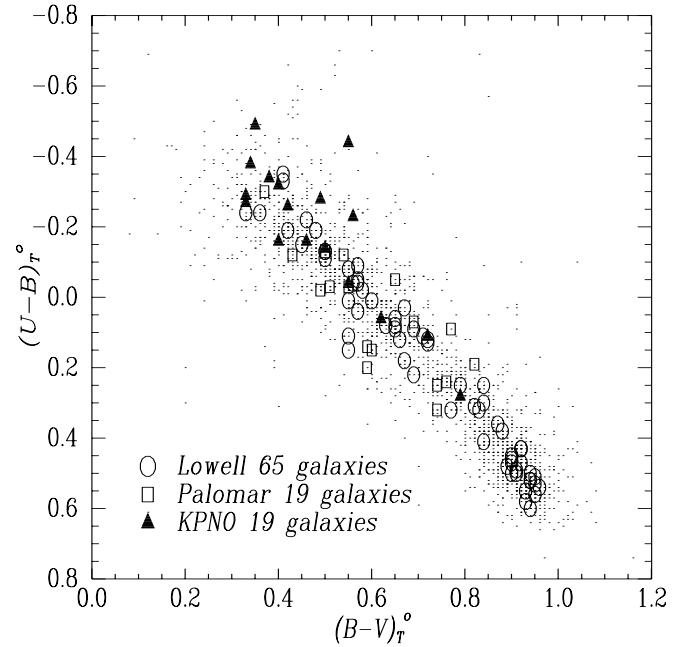


FIG. 2.— $UBV$  colors of the Frei et al. (1996) and KPNO samples. The extinction-corrected total apparent magnitudes  $(U_T^0 B_T^0 V_T^0)$  were taken from the RC3. The dots are 2248 galaxies with  $UBV$  colors in the RC3. From the 82 Lowell and 31 Palomar data, 65 (open circles) and 19 (open squares) galaxies, respectively, have RC3  $UBV$  magnitudes. From the 23 galaxies observed at KPNO, 19 (filled triangles) have RC3 entries.

catalog because not all of the galaxies have  $UBV$  entries in the RC3. As expected, the KPNO sample of galaxies has bluer colors than the CDI galaxies. Compared with the RC3 data, the CDI and KPNO galaxies cover most of the range in the  $UBV$  plane.

The values of  $H\alpha$  EW of 62 galaxies in the sample are compared with their  $(B-V)_T^0$  colors in Figure 3. The  $H\alpha$  emission data are a blend of  $H\alpha$  and the forbidden line  $[N II] \lambda\lambda 6548 + 6583$  with random errors of  $H\alpha + [N II]$  typically between 5% and 10% in bright galaxies to  $\pm 30\%$  in the weakest ( $3\sigma$ ) lines measured (Kennicutt 1992). In the sample of Kennicutt (1992) the ratio  $[N II]/H\alpha$  ranges anywhere from 70% to 0% and has a median value of 0.53. In a few cases  $H\beta$  measurements (Gallagher et al. 1989) are used to estimate  $H\alpha$  using the relationship determined by Kennicutt (1992):  $EW(H\alpha + [N II]) = 6 EW(H\beta) + 30$ , with a scatter about the mean relation of roughly  $\pm 30\%$ . In Figure 3, the  $(B-V)_T^0$  colors are from the RC3 and their associated errors are taken to be nominally 0.04.

In conclusion, Figures 2 and 3 show the expected trend of increasing  $H\alpha$  EW with bluer color and show that the data points with the bluest  $(U-B)_T^0$  and  $(B-V)_T^0$  colors and with the largest  $H\alpha$  EW are generally from the KPNO sample. Under the hypothesis that the morphology in the rest frame  $B$  band and the SFR estimated from optical colors or  $H\alpha$  emission are closely related to each other, later we introduce structural parameters chosen a priori to be related to the star formation rate that can be measured objectively and out to redshifts of  $z \sim 1$ .

## 2.2. Description of Hubble Deep Field Data

The sample of distant galaxies used in this study was taken from the Hubble Deep Field (HDF) images at  $\alpha = 12^h 36^m 49^s.5$  and  $\delta = +62^\circ 12' 58''$  (J2000.0) observed with the Hubble Space Telescope Wide Field Planetary Camera 2

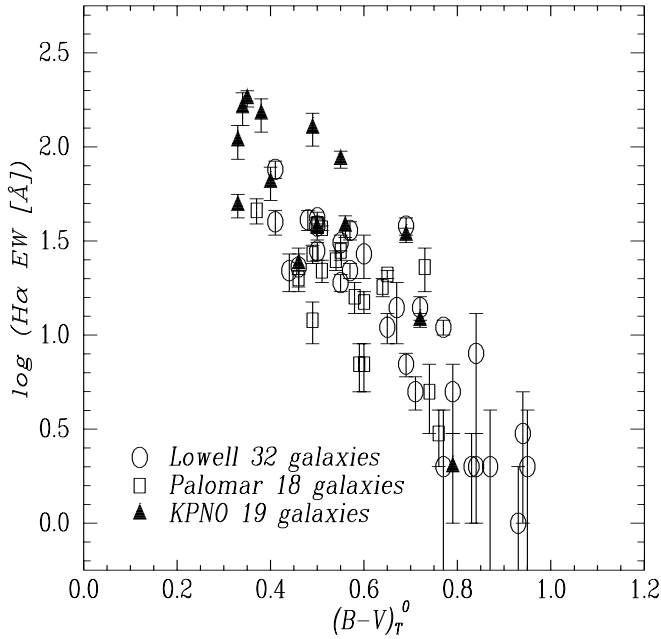


FIG. 3.— $H\alpha$  EW in  $\text{\AA}$  versus  $(B-V)_r^0$  color. Clearly shown is the trend that galaxies undergoing higher rate of star formation, i.e., larger  $H\alpha$  EWs, have bluer colors than quiescent galaxies. The errors in  $H\alpha$  are from the source catalogs mentioned in the text and the errors in the colors (not shown) are approximately 0.04 mag.

(*HST*/WFPC2) (Williams et al. 1997).<sup>4</sup> The HDF covers an area of  $2' \times 2'$  ( $0''.1 \text{ pixel}^{-1}$ ), which was selected to have high Galactic latitude ( $b = 54.8$ ), to have low extinction [ $E(B-V) = 0.00$ ], and to be devoid of bright sources and clusters of galaxies. The data taken in four bandpasses, F300W ( $U$ ), F415W ( $B$ ), F606W ( $V$ ), and F814W ( $I$ ), reach down to about 29 mag in the  $V$  and  $I$  bands (Cohen et al. 1996). A number of flanking fields have also been targeted as part of the HDF project with shorter integration times of 2500–5300 s; they will not be discussed in this study. This study will be concerned with galaxies imaged with the WFC due to its larger areal coverage ( $5.3 \text{ arcmin}^2$ ) compared to the PC ( $0.38 \text{ arcmin}^2$ ). The data were obtained with a nominal instrumental gain of  $7e^- \text{ ADU}^{-1}$  and readout noise of  $5e^-$ . The HDF program was undertaken partly to determine the nature of the faint blue galaxies by studying their morphologies at high resolution. In fact, the HDF optical images provide an unprecedented opportunity to study the structure of galaxies at redshifts  $0.2 < z < 4$

<sup>4</sup> Based on observations with the NASA/ESA *Hubble Space Telescope*, obtained at the Space Telescope Science Institute, which is operated by the Association of Universities for Research in Astronomy, Inc. under NASA contract NAS 5-26555.

because of the faint flux limit (29 mag), wide wavelength coverage (2500–9000  $\text{\AA}$ ), and high spatial resolution ( $\frac{1}{3}$ – $\frac{1}{2}$  kpc per pixel).

In this study I use the version 2 publicly available images that were processed using the “drizzling” technique developed by Andrew Fruchter and Richard Hook (Williams et al. 1997). The drizzling technique combines images of the same field accounting for geometric distortions of the optical system and stacking each frame shifted by fractional pixels. The final product is an image with pixel sizes 2.5 times smaller than the input frames. Image combination with the “drizzle” technique is not perfect. It causes the noise in one pixel to be correlated with the noise in an adjacent pixel and it introduces subtle changes in the PSF that translate into a  $\sim 10\%$  error in the detection and photometry of faint sources.

### 2.2.1. Limiting Surface Brightness Levels in the HDF

The limiting magnitude in the  $I$  band is  $\sim 3$  mag fainter than the deepest ground-based observations and  $\sim 1$  mag fainter than the deepest observations undertaken previously with the *HST* (Cohen et al. 1996). To have an idea of the faintest flux levels reached by the combined HDF data I present in Table 1 for each filter the number of frames ( $N_{\text{frames}}$ ), total exposure times ( $T_{\text{exp}}$ ) in seconds, AB magnitude zero points ( $Z$ ) corresponding to the flux of  $1 \text{ ADU s}^{-1}$ ,  $10 \sigma$  AB limiting magnitudes, and surface brightness levels at  $10$  and  $3 \sigma$ . The limiting magnitude will be defined in the same way as Williams et al. (1997):

$$m_{\text{lim}} = -2.5 \log \sigma + Z, \quad (1)$$

where effectively  $\sigma$  is the intensity fluctuation on a scale of 20 original WF pixels ( $0''.1 \times 0''.1 \times 20 = 0.2 \text{ arcsec}^2$ ). The surface brightness levels are then

$$\mu_{\text{lim}} = m_{\text{lim}} - 2.5 \log \left( \frac{1}{0''.1} \right)^2 \text{ mag arcsec}^{-2}. \quad (2)$$

The sources that contribute to  $\sigma$  are the Poisson noise of the sky and the instrumental noise. For example, consider the F606W band in which the sky count rate is expected to be  $0.090 e^- \text{ s}^{-1} \text{ pixel}^{-1}$  (Biretta 1996) in the WFC assuming  $\mu_V = 22.9 \text{ mag arcsec}^{-2}$ . For the exposures in the HDF the sky fluctuations should amount to  $\sigma_{\text{sky}} = 99.1e^-$ . The instrumental readout noise ( $5e^-$ ) for 103 frames (see Table 1) adds up to  $\sigma_r = (103 \times 5^2)^{1/2} = 50.7e^-$ . Hence, the expected fluctuation and limiting magnitudes are

$$\begin{aligned} \sigma^2 &= \sigma_{\text{sky}}^2 + \sigma_r^2 \Rightarrow \sigma = 111.4e^- = 15.9 \text{ ADU}, \\ m_{\text{lim}}(V) &= -2.5 \log (15.9 \times 10 \times \sqrt{20/109,050}) + 23.21 \\ &= 28.67 \text{ mag}, \end{aligned}$$

which is comparable to the measured value of 28.21 mag (see Table 1). Similarly, the expected limiting magnitudes in

TABLE 1  
CHARACTERISTICS OF HUBBLE DEEP FIELD IMAGES

Filter	$N_{\text{frames}}$	$T_{\text{exp}}$ (s)	$Z$	$10 \sigma m_{\text{lim}}^a$ (mag)	$10 \sigma \mu_{\text{lim}}^a$ (mag arcsec $^{-2}$ )	$3 \sigma \mu_{\text{lim}}^a$ (mag arcsec $^{-2}$ )
F300W.....	77	153,700	20.79	26.98	21.98	24.48
F450W.....	58	120,600	21.93	27.86	22.86	25.36
F606W.....	103	109,050	23.03	28.21	23.21	25.71
F814W.....	58	123,600	22.09	27.60	22.60	25.10

<sup>a</sup> AB magnitude.

TABLE 2  
HUBBLE DEEP FIELD: GALAXY PROPERTIES

IDENTIFICATIONS						F300W	F450W	F606W	F814W
Sawicki 1997	Cowie 1996	Williams et al. 1997	van den Bergh et al. 1996	$z_s^a$	$z_p^b$	$U^b$	$B^b$	$V^b$	$I^b$
(1)	(2)	(3)	(4)	(5)	(6)	(7)	(8)	(9)	(10)
20038 .....	...	2-082	2-033	2.267	2.40	26.28	24.53	24.47	24.49
20058 .....	004	2-121	...	0.475	0.45	25.98	23.27	21.50	20.43
20105 .....	122	2-153	2-074	...	0.95	25.27	24.97	24.61	23.68
20128 .....	115	2-180	2-096	...	1.25	25.47	24.88	24.67	23.96
20139 .....	082	2-201	2-099	...	1.55	25.29	24.51	24.31	23.83
20148 .....	076	2-210	2-085/086	...	0.70	24.62	24.13	23.57	22.80
20156 .....	037	2-264	2-134	0.478	0.45	24.07	23.46	22.66	22.09
20177 .....	...	2-236	2-127	...	1.55	25.53	24.95	24.71	24.35
20179 .....	066	2-246	2-116	0.958	1.25	25.22	24.52	24.09	23.14
20183 .....	009	2-251	...	0.960	0.65	24.72	23.37	22.33	21.25
20190 .....	043	2-256	2-121	...	1.50	25.48	24.61	24.19	23.48
20194 .....	017	2-264	2-135	0.475	0.50	24.84	23.50	22.28	21.47
20213 .....	127	2-270	2-139	0.130	0.15	25.40	24.56	24.11	23.87
20315 .....	006	2-404	...	0.199	0.15	21.91	20.68	20.04	19.68
20316 .....	000	2-456	...	0.089	0.10	22.73	19.84	18.82	18.20
20371 .....	075	2-449	2-243	2.845	2.40	25.67	23.94	23.70	23.41
20378 .....	142	2-454	2-242	...	2.30	26.48	24.67	24.60	24.25
20421 .....	022	2-514	2-280	0.752	0.70	24.38	23.56	22.76	21.75
20456 .....	051	2-531	2-278	...	1.10	25.29	24.59	24.07	23.08
20507 .....	061	2-585	2-299/301	...	2.40	27.33	24.98	24.60	23.95
20513 .....	105	2-591	2-313	...	1.70	25.86	24.97	24.88	24.61
20578 .....	010	2-652	...	0.557	0.60	24.20	23.44	22.05	21.10
20587 .....	084	2-661	2-352	...	0.95	24.68	24.36	23.95	23.13
20627 .....	070	2-702	2-383	...	0.55	25.25	24.66	23.82	23.11
20666 .....	039	2-736	2-403	1.355	1.70	24.03	23.25	23.04	22.74
20691 .....	099	2-762	2-416	...	0.45	24.82	24.53	23.73	23.34
20785 .....	046	2-860	2-482	...	1.00	24.48	23.92	23.38	22.45
20821 .....	...	2-906	2-520	...	1.05	24.62	24.13	23.57	22.80
20830 .....	...	2-903	2-513	...	2.35	26.68	24.79	24.59	24.52
20865 .....	087	2-950	2-535	...	0.45	25.73	24.88	24.04	23.43
20896 .....	057	2-982	2-553	1.148	1.50	24.39	23.79	23.38	22.70
30052 .....	131	3-118	3-056	0.511	2.25	26.06	24.66	24.43	24.32
30079 .....	024	3-143	3-090	0.475	0.50	24.55	23.69	22.70	21.94
30096 .....	113	3-174	3-111	0.089	2.00	24.91	24.10	23.59	23.19
30100 .....	064	3-180	3-135	...	0.30	25.08	24.58	24.06	23.78
30119 .....	073	3-203	3-128	0.319	0.30	24.10	23.56	22.90	22.59
30135 .....	054	3-221	3-153	0.952	1.10	25.53	24.71	24.23	23.16
30172 .....	...	3-258	3-169	...	0.50	25.29	24.77	24.07	23.58
30176 .....	094	3-259	3-174	...	1.95	25.25	24.44	23.74	23.17
30218 .....	013	3-321	...	0.680	0.60	27.02	24.84	22.88	21.39
30251 .....	007	3-350	...	0.642	0.70	23.71	22.80	21.89	20.89
30272 .....	030	3-355	3-294	...	1.10	25.55	24.83	24.37	23.19
30288 .....	015	3-386	...	0.474	0.45	22.74	22.11	21.31	20.73
30301 .....	033	3-400	3-296	0.474	0.50	23.27	22.94	22.23	21.73
30318 .....	056	3-405	3-283	0.320	0.30	23.89	23.44	22.83	22.59
30343 .....	...	3-430	...	1.150	1.15	24.63	24.44	24.34	23.93
30352 .....	095	3-443	3-312	0.950	1.15	25.31	24.65	24.37	23.37
30391 .....	031	3-486	3-350	0.790	0.85	24.51	23.81	23.02	21.90
30424 .....	027	3-534	...	0.321	0.40	23.61	22.78	21.85	21.30
30429 .....	003	3-610	...	0.518	0.50	27.43	23.42	21.50	20.21
30440 .....	068	3-551	3-376	0.560	0.55	25.08	24.47	23.72	23.03
30443 .....	180	3-550	3-379	2.775	2.10	26.56	25.00	25.21	25.04
30498 .....	...	3-597	3-406	...	1.10	25.42	24.99	24.90	24.37
30542 .....	019	3-659	3-426	0.299	0.30	25.04	23.36	22.26	21.56
30585 .....	086	3-696	3-475	0.401	0.45	24.81	24.44	23.63	23.16
30592 .....	174	3-704	3-481	...	1.75	24.83	24.32	24.31	24.23
30655 .....	052	3-773	3-512	0.561	0.50	24.49	23.88	23.06	22.45
30659 .....	081	3-777	...	0.500	0.50	24.52	24.18	23.40	22.89
30670 .....	018	3-790	...	0.550	0.55	26.06	24.09	22.49	21.33
30753 .....	091	3-863	3-581	0.682	0.75	24.69	24.46	24.00	23.34
30767 .....	097	3-875	3-589	...	3.20	26.06	24.74	23.98	24.20
30826 .....	...	3-943	3-629	0.321	0.25	25.22	24.30	23.59	23.23
40057 .....	047	4-120	4-056	0.953	0.80	25.17	24.92	24.63	24.00

TABLE 2—*Continued*

IDENTIFICATIONS						F300W	F450W	F606W	F814W
Sawicki 1997	Cowie 1996	Williams et al. 1997	van den Bergh et al. 1996	$z_s^a$	$z_p^b$	$U^b$	$B^b$	$V^b$	$I^b$
(1)	(2)	(3)	(4)	(5)	(6)	(7)	(8)	(9)	(10)
40106 .....	072	4-173	4-085	...	0.90	25.15	24.66	24.17	23.26
40162 .....	021	4-241	...	...	0.35	22.95	22.27	21.49	21.07
40178 .....	080	4-232	4-137	0.421	0.40	24.37	23.95	23.22	22.80
40186 .....	045	4-260	4-105	0.960	1.15	24.86	24.26	23.89	22.97
40187 .....	109	4-235	4-132	0.961	1.05	23.83	23.76	23.78	23.34
40224 .....	...	4-284	4-162	...	0.95	25.52	24.87	24.13	22.95
40335 .....	...	4-382	4-235	...	0.05	26.58	24.97	24.44	24.07
40345 .....	101	4-393	4-241	...	1.90	25.71	24.94	24.83	24.78
40350 .....	032	4-402	...	0.558	0.50	23.68	22.82	21.80	20.96
40392 .....	102	4-430	4-258	0.873	0.90	24.90	24.94	24.87	24.28
40408 .....	083	4-445	4-270	2.268	2.20	25.73	24.20	24.02	23.64
40425 .....	025	4-471	4-280	0.503	0.45	27.18	24.61	22.96	21.90
40430 .....	074	4-474	4-286	1.059	1.10	25.26	24.77	24.49	23.62
40500 .....	008	4-550	...	1.016	0.90	25.01	24.28	23.66	22.56
40515 .....	085	4-558	4-348	...	0.40	24.93	24.39	23.52	23.01
40522 .....	058	4-565	4-357	0.752	0.80	24.26	23.93	23.43	22.62
40569 .....	182	4-618	4-375	...	0.65	25.03	24.82	24.39	23.87
40586 .....	178	4-639	4-387	2.591	2.50	27.62	24.86	24.79	24.67
40603 .....	011	4-656	...	0.454	0.45	22.76	22.12	21.24	20.69
40651 .....	100	4-692	4-455	...	1.05	24.65	24.47	24.34	23.80
40674 .....	059	4-727	4-466	...	1.15	23.75	23.50	23.41	23.04
40686 .....	005	4-744	...	0.765	0.65	26.51	24.39	22.40	20.79
40709 .....	020	4-775	4-487	...	1.05	26.39	24.90	23.81	22.36
40733 .....	014	4-795	...	0.432	0.45	23.30	22.53	21.59	20.93
40792 .....	...	4-852	4-585	...	2.00	25.35	24.33	23.91	23.63
40818 .....	071	4-878	4-626	0.882	2.25	25.41	23.97	23.60	23.29
40822 .....	181	4-868	4-608	...	1.70	24.96	24.57	24.60	24.53
40845 .....	077	4-888	4-627	1.010	1.25	25.36	24.93	24.77	24.28
40877 .....	...	4-928	4-660	...	0.75	26.61	24.64	23.56	22.22
40882 .....	...	4-948	...	...	1.50	26.08	24.95	24.58	23.80
40901 .....	...	4-950	4-665	...	0.61	23.80	23.46	22.79	22.14

<sup>a</sup> Spectroscopic redshifts from Cowie 1996.

<sup>b</sup> Magnitudes and photometric redshifts from Sawicki 1997.

the other bands are  $m_{\text{lim}}(U) = 27.62$  mag,  $m_{\text{lim}}(B) = 28.17$  mag, and  $m_{\text{lim}}(I) = 27.92$  mag, which again agree with the measured values.

The structure of galaxies out to galactocentric radii comparable to the solar radius  $R_0$  can be studied out to  $z \sim 1$ . The surface brightness at the  $3\sigma$  level reached by the HDF data is comparable to the surface brightness of our Galaxy at the solar radius  $R_0$  (see Table 1). Several studies suggest that the surface brightness of the disk of our Galaxy is an exponential function of the galactocentric radius:  $I(R) = I_0 e^{R/R_d}$ , where  $R_d = 3.5$  kpc (de Vaucouleurs & Pence 1978). At the solar radius the surface brightness in the  $V$  band has been estimated to be  $\text{SB}(V) \sim 15 L_\odot(V) \text{ pc}^{-2}$  (de Vaucouleurs & Pence 1978; Bahcall & Soneira 1980). Given that in the  $V$  band  $1 L_\odot(V) \text{ pc}^{-2}$  corresponds to  $\mu_V = 26.34$  mag arcsec $^{-2}$ ,<sup>5</sup> at  $R_0$  the surface brightness is  $\mu_V = 23.40$  mag

arcsec $^{-2}$ . Observing at a redshift of  $z = 1$ , a region at  $R = R_0 = 2.43R_d$  will have a surface brightness observed in the  $I$  band of  $\text{SB} = 23.4 + 2.5 \log(1+z)^3 = 25.7$  mag arcsec $^{-2}$  assuming that the bandwidths of both filters match closely when redshifted to  $z$ , i.e.,  $\Delta\nu(I) = \Delta\nu(V) \times (1+z)^{-1}$ . Compared to the limiting surface brightness levels reached by the HDF data, the structure of disk galaxies like the Milky Way can be studied out to galactocentric distances of 8.5 kpc or 2.4 times the exponential disk scale length. Note that a conservative surface brightness limit of  $10\sigma$  will limit the study of the structure of galaxies at redshifts  $z = 0.5$  to a galactocentric radius of only  $R = \frac{1}{3}R_d$ .

### 2.2.2. HDF Source Catalogs

Several algorithms have been used to construct source catalogs from the HDF (e.g., Gwyn & Hartwick 1996; Williams et al. 1997; Abraham et al. 1996a; Sawicki, Lin, & Yee 1997). They all detect similar numbers of sources, for example, Sawicki et al. (1997) find 1577 nonstellar objects down to  $I = 28$  mag. For this study, I compiled a list from the work of Sawicki et al., who kindly provided me with their machine readable catalog that consists of  $UBVI$  magnitudes,  $X$ - $Y$  CCD pixel positions, and photometric redshifts.

A number of HDF galaxies have measured spectroscopic redshifts (Cowie 1996; Cohen et al. 1996; Steidel et al. 1996;

<sup>5</sup> The surface brightness can be expressed as  $\text{SB} = L/D^2 = 4\pi d^2 f(\theta d)^2$ , where  $L$  is the absolute luminosity,  $D$  is the size of a region in parsecs,  $f$  is the apparent flux at a distance  $d$ , and  $\theta$  is the angular size subtended by  $D$  at a distance  $d$  from us. Transforming the SB in the  $V$  band to  $cgs$  units gives  $\text{SB}_V = 1 L_\odot(V) \text{ pc}^{-2} = 5.64 \times 10^{-16} \text{ ergs}^{-1} \text{ cm}^{-2} \text{ arcsec}^{-2}$  given that  $L_\odot(V) = 2.86 \times 10^{33} \text{ ergs}^{-1}$  and  $M_V(\odot) = 4.77$  (Mihalas & Binney 1981). Using  $m_1 - m_2 = -2.5 \log(f_1/f_2)$  and identifying  $m_1 = \mu_V$ ,  $m_2 = M_V(\odot)$ ,  $f_1 = 5.64 \times 10^{-16} \text{ ergs}^{-1} \text{ cm}^{-2} \text{ arcsec}^{-2}$ , and  $f_2 = 2.86 \times 10^{33}/[4\pi(10 \text{ pc})^2]$  results in  $\mu_V = 26.34 \text{ mag arcsec}^{-2} \Leftrightarrow \text{SB}_V = 1 L_\odot(V)/\text{pc}^{-2}$ .



Lowenthal et al. 1997). High-redshift galaxies with  $z > 1$  have been especially targeted by Steidel et al. (1996) and Lowenthal et al. (1997). Galaxies with moderate redshifts have been published by Cohen et al. (1996) and Cowie (1996). Together, they comprise 70 galaxies with spectroscopically determined redshifts in the HDF, excluding stars (three) and excluding the flanking fields.

The exact number of sources in the HDF remains uncertain due to crowding problems. At  $B \leq 25$  the catalog of Sawicki contains 122 sources of which 28 could be considered subclumps of a larger structure. This uncertainty in the number of sources has the following implications. If a system is observed as a collection of substructures that are in fact unrelated to each other but are always identified as a single object then the apparent fluxes will be overestimated and the number of objects will be systematically underestimated. On the other hand, if a single source containing several high surface brightness regions is identified as a group of unrelated objects, then the opposite situation will occur where the fluxes will be underestimated and the number of sources overestimated, resulting in a steepening of the counts at fainter fluxes (Colley et al. 1996). It is unlikely that either one of these extreme situations will occur exclusively, rather both conditions may be present in source catalogs. Until additional information is gathered (e.g., spectroscopy) there is no strong reason to prefer to split or merge the systems in dispute. In this study each of the 28 sources are arbitrarily considered as part of a larger structure, resulting in a total number of galaxies of 94.

Table 2 contains data of the 94 HDF galaxies. The entries are as follows. *Columns (1)–(4)*.—Galaxy identification numbers from the catalogs of Sawicki et al. (1997), Cowie (1996), Williams et al. (1997), and van den Bergh et al. (1996), as indicated. *Column (5)*.—Spectroscopic redshift of Cowie (1996) unless otherwise indicated. *Column (6)*.—Photometric redshift from Sawicki et al. (1997). *Columns (7)–(10)*.—AB magnitudes from Sawicki et al.

### 3. STRUCTURAL PARAMETERS OF GALAXIES

The classification of galaxies based on their appearance is difficult. It requires years to master the art of galaxy classification and even so when done by different individuals the results do not always concur (van den Bergh 1989; Naim et al. 1995b; Abraham et al. 1996b). It has long been realized that an outstanding problem in classical galaxy classification is its qualitative and subjective nature (Mihalas & Binney 1981). The problem is being tackled by identifying the fundamental physical parameters that dictate the way galaxies are shaped (Driver et al. 1995; Abraham et al. 1996a; Naim et al. 1995a). Since galaxies are very complex systems, this task has proven to be far from easy. The origin and evolution of galaxies are orchestrated by a number of processes involving a diversity of parameters among which are the total mass, characteristic size, bolometric luminosity, angular momentum, and gas surface density. We envision a classification of galaxies that is multidimensional and panchromatic and we can start by investigating a few of its dimensions.

Considering the large number of observational quantities that characterize galaxies (fluxes, colors, and spectra from the X-ray to the radio wave bands, rotation curves, surface brightnesses, etc.), it is surprising that only one parameter related to the image structure, namely, the Hubble type, is so commonly used and so widely accepted. The systematics

present in conventional galaxy classification and the complexity of the morphologies of galaxies force us to search for a number of diverse observables, the most fundamental of which can be later singled out, for instance, by performing a principal component analysis (Whitmore 1984). Although the Hubble system brings about order among the majority of disks and spheroids, *irregulars* make up an eclectic group whose principal morphological features remain difficult to organize and identify. Information amassed from ever increasing galaxy databases impelled the introduction and implementation of new parameters at low and high redshifts: the concentration index (CI) (Morgan 1958, 1959; Okamura et al. 1984; Kent 1985; Doi et al. 1993; Abraham et al. 1994, 1996b) and the asymmetry (A) (Abraham et al. 1996b). The concentration index is in fact Hubble's first criterion so that its trend with morphological type is expected. The asymmetry parameter deals with a signal of lower amplitude and has been only recently measured with the *Hubble Space Telescope* at cosmologically interesting redshifts. A new parameter, the high spatial frequency power  $\chi$ , is explored in this study which, like the asymmetry, involves a low-amplitude signal. Both quantities are similar in that they have been defined with the intent to measure processes involving star formation, but they are different in their formal definition, and, as will be seen later, they ultimately measure different properties.

#### 3.1. Metric Size

Under the hypothesis that the modulation of the optical light distribution in galaxies is due to the presence of O and B type stars, the power at high spatial frequencies should correlate with the flux from star-forming regions. To measure this power we are challenged to define a suitable spatial scale length that separates the high- and low-frequency components of an image. I use the so called  $\eta$  function (Petrosian 1976) to define a characteristic length that in turn will supply a scaled aperture size to measure fluxes and an estimate of the sizes of star-forming regions. The characteristic lengths determined this way are metric sizes that are less affected by the limiting surface brightness level reached and are consequently useful for applications at high redshifts. Metric sizes are preferable over isophotal ones because the physical length of the latter decreases with increasing redshift.

To illustrate the difference between isophotal and metric radii consider galaxies with exponential disk profiles

$$I(\theta) = I_0 e^{-\theta/\theta_d},$$

where  $I_0$  is the central surface brightness. Assuming that  $\theta_d$  is defined so that it is insensitive to the conditions in which the data were taken (a weak function of angular resolution and signal-to-noise ratio) and assuming further that the profiles of galaxies do not evolve with cosmological time, then the disk scale length  $\theta_d$  remains an intrinsic property of the intensity profile and defines a metric size. On the other hand, the isophotal size is defined as the angular size at which the intensity attains a given value, typically  $\mu_i = 25$  mag arcsec $^{-2}$ .

At a redshift  $z$ , the intensity profile can be rewritten as

$$I(\theta, z) = \frac{I_0}{(1+z)^4} e^{-\theta(z)/\theta_d}.$$

Setting its value to a surface brightness level, say  $\mu_i = 25$  mag arcsec $^{-2}$ , which corresponds to  $I_i = 6.3 L_\odot \text{ pc}^{-2}$ , the

ratio between the isophotal and metric radii becomes

$$\frac{\theta_i}{\theta_d} = \ln\left(\frac{I_0}{I_i}\right) - 4 \ln(1+z),$$

with the isophotal radius measuring systematically smaller sizes than the metric radius. Similarly, considering a Hubble intensity profile

$$I(\theta) = \frac{I_0}{(1 + \theta/\theta_d)^2},$$

$$\frac{\theta_i}{\theta_d} = \frac{1}{(1+z)^2} \sqrt{\frac{I_0}{I_i}} - 1.$$

Assuming that both profile types have central intensities  $I_0 = 138 L_\odot \text{ pc}^{-2}$  at redshifts as low as  $z = 0.1$  the isophotal radius is 15%–25% smaller than the metric radius. Isophotal sizes are easily measured and widely used, but they clearly do not characterize any metric property of the galaxies.

The  $\eta$  function, first introduced by Petrosian (1976) as a tool to estimate metric sizes, is defined as the ratio of the average surface brightness up to a radius  $R$  to the surface brightness at  $R$ . By means of the  $\eta$  function several studies have attempted to measure galaxy evolution in surface brightness (Petrosian 1976) and angular diameters (Djorgovski & Spinrad 1981), whereas others have attempted to determine the form of the surface brightness decline with redshift to measure the expansion of the universe (e.g., Sandage & Perlmutter 1991; Kjaergaard, Jorgensen, & Moles 1993; Pahre, Djorgovski, & Carvalho 1996). Here I employ the  $\eta$  function to characterize sizes intrinsic to the galaxies and adopt the redefinition of Kron (1995), which is the inverse of Petrosian's definition:

$$\eta(R) = \frac{I(R)}{\langle I(R) \rangle}, \quad (3)$$

where in practice  $I(R)$  is the intensity measured within an annulus at a radius  $R$  from the center of the galaxy and  $\langle I(R) \rangle$  is the average intensity within  $R$ , i.e., the total intensity up to a radius  $R$  divided by the area. With this definition for intensity profiles that decrease with  $R$ , at the center of the galaxy  $\eta(R=0) = 1$ , and at large distances from the center,  $\eta(R \rightarrow \infty) \rightarrow 0$ . The formal error in  $\eta$  given by standard error propagation formulae (Bevington 1969) is

$$\sigma_\eta^2 = \eta^2 \left( \frac{\sigma_I^2}{I^2} + \frac{\sigma_{\langle I \rangle}^2}{\langle I \rangle^2} \right), \quad (4)$$

where  $\sigma_I^2$  and  $\sigma_{\langle I \rangle}^2$  are the photometric errors of  $I(R)$  and  $\langle I(R) \rangle$ , respectively.

The metric size  $R_\eta$  is chosen as the smallest radius where the function  $\eta$  attains the value  $\frac{1}{3}$ , i.e.,  $R_\eta \equiv R(\eta = \frac{1}{3})$ .<sup>6</sup> The value of  $\eta = \frac{1}{3}$  was chosen because it is far enough from the center not to be affected by resolution, yet close enough to the center to avoid the signal being dominated by sky.

The Petrosian radius  $R_\eta$  can be expressed in terms of the more familiar exponential disk scale length  $R_d$ . Assuming a surface brightness profile of the form  $I(R) = I_0 \exp^{-R/R_d}$ , where  $R$  is the galactocentric radius and  $I_0$  is the central

surface brightness,  $\eta(R)$  takes the form

$$\eta(R) = \frac{1}{2} \left( \frac{R}{R_d} \right)^2 \left( \exp^{R/R_d} - \frac{R}{R_d} - 1 \right)^{-1} \quad (5)$$

at  $\eta = \frac{1}{3}$ ,  $R_\eta = 2.65 R_d$ , which in our Galaxy corresponds to roughly 9.3 kpc (Binney & Tremaine 1987) and which incidentally matches nicely the radius at the  $3 \sigma$  level surface brightness limit of the HDF data.

### 3.1.1. Method

In practice, the  $\eta$  functions are constructed using elliptical apertures. These are isophotal ellipse contours fitted to the galaxy image using the task ellipse in IRAF/STSDAS (Jedrzejewski 1987; Busko 1996), which at each semimajor axis measures, among many other parameters, the isophotal intensity ( $I_e$  in ADU) at a given semimajor axis, the root mean square deviation [ $e(I_e)$ ] of the fit, the number of data points ( $n_e$ ) in the fit, the total flux ( $F_e$  in ADU), and total number of valid pixels inside the ellipse ( $N_e$ ).

In addition to the quantities ellipse computes, I determine the sky level (sky) in (ADU pixel<sup>-1</sup>) and its standard deviation ( $\sigma_{\text{sky}}$ ) with the optimal filtering algorithm in the IRAF task FITSKYPARS within an annulus of 20–30 pixels far from the outskirts of the galaxy. The choice of the radius of the region in which the sky is calculated is critical and was chosen around that point where the integrated light of the galaxy as a function of galactocentric radius is flat. Finally, it was verified that the encircled energy profiles of the sky-subtracted images have a slope of zero at and beyond the chosen radius.

Given the detector's gain  $g$  (e<sup>-</sup> ADU<sup>-1</sup>), the intensity and the average intensity in e<sup>-</sup> are

$$I(R) = (I_e - \text{sky})g, \quad (6)$$

$$\langle I(R) \rangle = \left( \frac{F_e}{N_e} - \text{sky} \right)g. \quad (7)$$

The associated errors of  $I(R)$  and  $\langle I(R) \rangle$  for  $N$  number of frames and a readout noise of  $rd$  are

$$\sigma_I^2 = (n_e I_e + \text{sky})g + \{[e(I_e) + \sigma_{\text{sky}}]g\}^2 + rd^2 N, \quad (8)$$

$$\sigma_{\langle I(R) \rangle}^2 = \left( \frac{F_e g}{N_e^2} + \text{sky} \right)g + (\sigma_{\text{sky}} g)^2 + rd^2 N. \quad (9)$$

At each radius  $\sigma_\eta(R)$  is computed using equations (4), (8), and (9).

The Petrosian radius is iteratively computed. During the first iteration, the ellipses are fitted starting at a semimajor axis length, which is  $\frac{1}{2}$  times the length of the image size. The  $\eta$  values are computed with equations (3), (6), and (7) and fitted as a function of  $R$  with weights equal to  $\sigma_\eta$ . A first guess of the metric radius  $R_\eta^0$  and improved values of the position angle, ellipticity, center position, and pixel step sizes are recorded and used as input parameters for the second iteration, which starts at  $R_\eta^0$ . In this way, the ellipse fit is forced to closely resemble the galaxy near the metric radius. Each  $\eta$  profile is fitted primarily within the region  $0.1 < \eta < 0.6$  with a Spline3 polynomial of order 1 or a Legendre polynomial of order 2. The task ELLIPSE fails in some occasions in fitting the center of the galaxy appropriately, which translated into unreliable values of the  $\eta$  function at radii smaller than 4 pixels. In addition, highly irregular galaxies like NGC 0023 or NGC 0488 cannot be fitted with concentric ellipses and therefore have  $\eta$  profiles

<sup>6</sup> In the definition of the  $\eta$  function expressed in magnitudes,  $\eta = \frac{1}{3}$  corresponds to  $\eta_{\text{mag}} = 2.5 \log(\eta^{-1}) = 1.2 \text{ mag}$ .

that can only be regarded as approximate. The errors in  $R_\eta$  are estimated from the  $\eta$  functions directly. For the entire nearby galaxy sample these errors average 40% but are typically 20%–27%. The metric radii of the nearby galaxies are presented in Table 3 ( $g$  band), Table 4 ( $B_J$  band), and Table 5 ( $B$  band). The columns of the tables are as follows. *Column (1).*—Galaxy name. *Column (2).*—Petrosian metric radius and errors. *Column (3).*—Core radius (see § 3.2). *Column (4).*—Projected angle of a 1 kpc-sized length. *Column (5).*—Isophotal semimajor axis length at the  $\mu_B = 25$  mag arcsec $^{-2}$  surface brightness level from the RC3. *Column (6).*— $\chi$  value using  $w = R_\eta^{2/3}$ . *Column (7).*— $\chi$  value using  $w = \frac{1}{2}R_\eta$ . *Column (8).*— $\chi$  value using a fixed 2 kpc-sized window. *Column (9).*— $\chi$  from the isophotal ellipse model. All scale sizes are in units of arcseconds. The metric radii measured in the  $V$  band and the  $UBVI$  fluxes of the HDF galaxies are presented in Table 6. The first four columns are the same as in Table 3 but *Columns (5)–(8)* contain the  $I$ ,  $V$ ,  $B$ , and  $U$  AB magnitudes determined within an aperture of radius  $R_T = 1.5R_\eta$ .

### 3.1.2. Results

Shown in Figure 4 are the  $\eta$  functions of three galaxies: NGC 3077, NGC 4449, and NGC 2403. They are all located at fairly small distances from us: NGC 3077 at 3.7 Mpc, NGC 4449 at 3.8 Mpc, and NGC 2403 at 3.7 Mpc. These

galaxies broadly represent the three types of  $\eta$  profiles found in the entire sample of galaxies. In general, galaxies with centrally concentrated and smooth intensity profiles have  $\eta$  functions like that of NGC 3077, whereas galaxies with insignificant bulges resemble that of NGC 2403. As in the case of NGC 4449, in other galaxies  $\eta(R)$  is not a monotonically decreasing function of  $R$ . The increase of the intensity relative to the average intensity can be traced to the presence of very bright cores, rings, bars, or star-forming regions. In the exceptional case when  $\eta$  assumes the value of  $\frac{1}{3}$  at very small radii ( $\sim 2''$ ), the galaxy was excluded from this study (NGC 7469, a Seyfert galaxy).

The  $\eta$  function varies only mildly with wavelength. Measured in a blue and a red band, the  $\eta$  profiles in Figure 4 show only small variations as a function of wavelength. Since the  $\eta$  functions define the value of the metric size, it is important for our purposes to consider the dependence of  $R_\eta$  with wavelength. The values of  $R_\eta$  of 14 galaxies that span a wide range in the  $UBV$  plane and that have available images in the  $B_J$  and  $R$  bands are shown in Figure 5. The metric radii  $R_\eta$  vary by about 20% between the  $B_J$  and  $R$  bands with 75% of the data having ranges less than 15% in  $R_\eta$ .

The resulting  $R_\eta$  of the nearby sample can be compared with the isophotal diameters compiled in the RC3. Figure 6 clearly shows that the metric and isophotal radii measure

TABLE 3  
 $g$ -BAND SAMPLE: STRUCTURAL PARAMETERS

NAME (1)	$R_\eta$ (arcsec) (2)	$R_c$ (arcsec) (3)	$R_h$ (arcsec) (4)	$R_{25}^a$ (arcsec) (5)	$\chi$			
					$R_\eta^{2/3}$ (6)	$\frac{1}{2}R_\eta$ (7)	2 kpc (8)	Model (9)
NGC 2403.....	265 $^{+66}_{-53}$	67	56	656	0.16	0.14	0.15	0.12
NGC 2541.....	114 $^{+86}_{-35}$	29	24	189	0.19	0.18	0.19	0.21
NGC 2903.....	152 $^{+11}_{-17}$	38	24	378	0.16	0.15	0.14	0.15
NGC 3031.....	111 $^{+36}_{-16}$	55	56	807	0.07	0.03	0.14	0.03
NGC 3198.....	150 $^{+42}_{-28}$	38	20	255	0.18	0.16	0.14	0.16
NGC 3319.....	73 $^{+27}_{-26}$	36	18	185	0.10	0.09	0.10	0.10
NGC 4178.....	120 $^{+60}_{-11}$	30	12	154	0.18	0.18	0.15	0.21
NGC 4189.....	62 $^{+5}_{-9}$	15	12	72	0.15	0.14	0.14	0.24
NGC 4192.....	194 $^{+50}_{-21}$	50	12	293	0.17	0.17	0.10	0.22
NGC 4216.....	48 $^{+21}_{-12}$	24	12	244	0.11	0.08	0.12	0.24
NGC 4254.....	105 $^{+12}_{-16}$	26	12	161	0.19	0.19	0.14	0.26
NGC 4258.....	198 $^{+28}_{-15}$	50	30	559	0.12	0.11	0.10	0.12
NGC 4303.....	74 $^{+40}_{-22}$	19	12	194	0.17	0.16	0.14	0.29
NGC 4321.....	90 $^{+44}_{-23}$	23	12	222	0.13	0.13	0.10	0.19
NGC 4394.....	54 $^{+27}_{-12}$	26	12	109	0.08	0.07	0.07	0.08
NGC 4414.....	70 $^{+32}_{-16}$	18	19	109	0.18	0.14	0.17	0.16
NGC 4498.....	54 $^{+37}_{-16}$	13	12	89	0.14	0.12	0.13	0.14
NGC 4501.....	137 $^{+23}_{-26}$	35	12	208	0.12	0.12	0.09	0.14
NGC 4527.....	131 $^{+48}_{-56}$	44	8	185	0.12	0.13	0.09	0.17
NGC 4535.....	174 $^{+42}_{-45}$	44	12	212	0.18	0.18	0.13	0.22
NGC 4548.....	118 $^{+59}_{-25}$	60	12	161	0.09	0.09	0.07	0.13
NGC 4559.....	183 $^{+31}_{-32}$	46	17	321	0.16	0.15	0.12	0.17
NGC 4569.....	184 $^{+19}_{-17}$	46	12	286	0.10	0.10	0.06	0.09
NGC 4571.....	98 $^{+40}_{-46}$	26	12	109	0.15	0.15	0.14	0.16
NGC 4579.....	89 $^{+38}_{-38}$	44	12	177	0.07	0.07	0.06	0.08
NGC 4651.....	55 $^{+42}_{-13}$	14	12	119	0.11	0.08	0.09	0.09
NGC 4654.....	113 $^{+16}_{-17}$	29	12	147	0.14	0.13	0.11	0.15
NGC 4689.....	77 $^{+22}_{-20}$	19	12	128	0.10	0.09	0.09	0.08
NGC 4725.....	145 $^{+57}_{-50}$	36	11	321	0.09	0.10	0.06	0.08
NGC 5033.....	60 $^{+41}_{-17}$	15	15	321	0.14	0.10	0.14	0.19
NGC 5055.....	194 $^{+82}_{-38}$	49	26	378	0.12	0.11	0.10	0.12

<sup>a</sup> RC3 isophotal radius.

TABLE 4  
J-BAND SAMPLE: STRUCTURAL PARAMETERS

NAME (1)	$R_\eta$ (arcsec) (2)	$R_c$ (arcsec) (3)	$R_h$ (arcsec) (4)	$R_{25}^a$ (arcsec) (5)	$\chi$			
					$R_\eta^{2/3}$ (6)	$\frac{1}{2}R_\eta$ (7)	2 kpc (8)	Model (9)
NGC 2683.....	$115^{+9}_{-8}$	57	34	280	0.20	0.11	0.25	0.16
NGC 2715.....	$107^{+11}_{-15}$	27	11	147	0.16	0.16	0.12	0.19
NGC 2768.....	$66^{+15}_{-7}$	34	9	244	0.05	0.03	0.02	0.02
NGC 2775.....	$43^{+13}_{-7}$	22	9	128	0.04	0.03	0.03	0.03
NGC 2976.....	$128^{+9}_{-12}$	3	55	177	0.22	0.13	0.38	0.11
NGC 2985.....	$26^{+10}_{-7}$	12	11	137	0.05	0.04	0.07	0.08
NGC 3077.....	$65^{+12}_{-6}$	16	55	161	0.21	0.08	0.45	0.15
NGC 3079.....	$177^{+36}_{-38}$	45	12	238	0.29	0.29	0.14	0.40
NGC 3147.....	$24^{+7}_{-10}$	12	5	117	0.03	0.03	0.03	0.07
NGC 3166.....	$16^{+3}_{-3}$	8	9	144	0.08	0.03	0.13	0.06
NGC 3184.....	$161^{+42}_{-36}$	38	23	222	0.16	0.16	0.13	0.06
NGC 3344.....	$123^{+23}_{-19}$	31	23	212	0.15	0.15	0.13	0.15
NGC 3351.....	$69^{+17}_{-17}$	34	18	222	0.10	0.08	0.09	0.10
NGC 3368.....	$55^{+26}_{-12}$	28	15	228	0.06	0.03	0.06	0.07
NGC 3377.....	$30^{+5}_{-11}$	30	19	157	0.05	0.02	0.14	0.04
NGC 3379.....	$24^{+5}_{-2}$	22	15	161	0.03	0.02	0.08	0.04
NGC 3486.....	$72^{+36}_{-17}$	18	20	212	0.17	0.12	0.15	0.15
NGC 3556.....	$208^{+39}_{-18}$	53	19	261	0.23	0.22	0.16	0.24
NGC 3596.....	$63^{+12}_{-7}$	16	11	119	0.12	0.11	0.09	0.14
NGC 3623.....	$150^{+24}_{-38}$	38	16	293	0.11	0.10	0.07	0.16
NGC 3631.....	$49^{+33}_{-17}$	12	12	150	0.15	0.13	0.13	0.20
NGC 3672.....	$96^{+17}_{-13}$	24	7	125	0.14	0.15	0.07	0.20
NGC 3675.....	$97^{+44}_{-45}$	26	18	177	0.10	0.08	0.08	0.13
NGC 3726.....	$140^{+19}_{-19}$	35	16	185	0.15	0.15	0.12	0.15
NGC 3810.....	$70^{+16}_{-15}$	18	14	128	0.16	0.13	0.12	0.18
NGC 3877.....	$113^{+14}_{-12}$	28	15	165	0.17	0.14	0.12	0.23
NGC 3893.....	$63^{+5}_{-8}$	16	14	134	0.16	0.13	0.13	0.18
NGC 3938.....	$109^{+17}_{-12}$	27	16	161	0.15	0.14	0.11	0.18
NGC 3953.....	$140^{+20}_{-22}$	35	12	208	0.12	0.12	0.09	0.13
NGC 4013.....	$77^{+62}_{-29}$	39	16	157	0.14	0.11	0.13	0.16
NGC 4030.....	$57^{+15}_{-9}$	15	9	125	0.11	0.11	0.09	0.13
NGC 4088.....	$128^{+28}_{-28}$	32	18	173	0.25	0.23	0.21	0.31
NGC 4123.....	$99^{+15}_{-17}$	24	9	131	0.18	0.19	0.12	0.20
NGC 4125.....	$40^{+9}_{-8}$	38	9	173	0.03	0.02	0.03	0.01
NGC 4136.....	$81^{+17}_{-14}$	20	22	119	0.15	0.13	0.14	0.14
NGC 4144.....	$123^{+25}_{-26}$	31	50	181	0.32	0.13	0.55	0.14
NGC 4157.....	$130^{+XX}_{-XX}$	32	18	67	0.24	0.20	0.18	0.21
NGC 4242.....	$154^{+XX}_{-XX}$	38	26	150	0.16	0.15	0.15	0.04
NGC 4340.....	$28^{+20}_{-8}$	14	12	106	0.06	0.02	0.10	0.07
NGC 4365.....	$31^{+9}_{-7}$	30	12	208	0.04	0.03	0.04	0.04
NGC 4374.....	$30^{+6}_{-5}$	27	12	194	0.02	0.01	0.03	0.03
NGC 4406.....	$40^{+14}_{-10}$	40	12	267	0.02	0.02	0.02	0.02
NGC 4429.....	$65^{+27}_{-23}$	32	12	169	0.06	0.04	0.05	0.06
NGC 4442.....	$23^{+5}_{-3}$	22	12	137	0.05	0.02	0.11	0.06
NGC 4449.....	$93^{+16}_{-11}$	23	66	185	0.30	0.16	0.54	0.23
NGC 4450.....	$93^{+30}_{-32}$	23	12	157	0.07	0.07	0.05	0.05
NGC 4472.....	$47^{+15}_{-4}$	46	12	307	0.02	0.02	0.02	0.01
NGC 4477.....	$27^{+12}_{-10}$	24	12	114	0.04	0.02	0.06	0.06
NGC 4486.....	$53^{+12}_{-10}$	51	12	250	0.02	0.02	0.02	0.02
NGC 4487.....	$99^{+44}_{-35}$	24	14	125	0.12	0.12	0.10	0.13
NGC 4526.....	$53^{+10}_{-8}$	26	12	217	0.05	0.03	0.05	0.05
NGC 4564.....	$22^{+4}_{-5}$	22	12	106	0.04	0.02	0.13	0.07
NGC 4593.....	$77^{+30}_{-21}$	38	5	117	0.06	0.07	0.04	0.11
NGC 4594.....	$99^{+59}_{-32}$	49	12	261	0.12	0.11	0.07	0.12
NGC 4621.....	$30^{+10}_{-6}$	27	12	161	0.03	0.01	0.05	0.03
NGC 4636.....	$43^{+13}_{-7}$	40	14	181	0.02	0.02	0.02	0.01
NGC 4710.....	$70^{+11}_{-11}$	35	12	147	0.21	0.14	0.16	0.20
NGC 4731.....	$122^{+27}_{-44}$	31	9	198	0.20	0.20	0.11	0.23
NGC 4754.....	$19^{+26}_{-9}$	19	12	137	0.03	0.02	0.11	0.06
NGC 4826.....	$134^{+26}_{-10}$	34	32	300	0.11	0.08	0.10	0.01
NGC 4861.....	$113^{+57}_{-42}$	28	16	119	0.20	0.19	0.17	0.20
NGC 4866.....	$68^{+47}_{-17}$	34	12	189	0.10	0.07	0.08	0.10
NGC 5005.....	$70^{+31}_{-10}$	35	14	173	0.09	0.07	0.07	0.10
NGC 5204.....	$92^{+46}_{-26}$	23	36	150	0.19	0.14	0.25	0.14

TABLE 4—*Continued*

NAME (1)	$R_\eta$ (arcsec) (2)	$R_c$ (arcsec) (3)	$R_h$ (arcsec) (4)	$R_{25}^a$ (arcsec) (5)	$\chi$			
					$R_\eta^{2/3}$ (6)	$\frac{1}{2}R_\eta$ (7)	2 kpc (8)	Model (9)
NGC 5248.....	$88^{+44}_{-35}$	22	12	185	0.14	0.14	0.12	0.19
NGC 5322.....	$31^{+13}_{-6}$	30	7	177	0.03	0.03	0.03	0.03
NGC 5334.....	$123^{+66}_{-58}$	31	9	125	0.17	0.17	0.15	0.19
NGC 5364.....	$147^{+50}_{-26}$	36	11	203	0.15	0.15	0.09	0.12
NGC 5371.....	$115^{+13}_{-38}$	28	5	131	0.12	0.13	0.07	0.15
NGC 5377.....	$46^{+36}_{-26}$	23	8	111	0.04	0.04	0.04	0.09
NGC 5585.....	$130^{+27}_{-54}$	32	36	173	0.15	0.12	0.15	0.14
NGC 5669.....	$93^{+47}_{-37}$	23	9	119	0.20	0.20	0.13	0.21
NGC 5701.....	$30^{+10}_{-5}$	30	9	128	0.03	0.02	0.04	0.05
NGC 5746.....	$96^{+17}_{-23}$	49	8	222	0.14	0.14	0.05	0.31
NGC 5792.....	$107^{+24}_{-17}$	27	7	208	0.14	0.15	0.08	0.28
NGC 5813.....	$61^{+30}_{-33}$	30	7	125	0.04	0.04	0.04	0.04
NGC 5850.....	$74^{+36}_{-31}$	36	5	128	0.08	0.08	0.05	0.10
NGC 5985.....	$111^{+16}_{-14}$	27	5	165	0.09	0.10	0.05	0.11
NGC 6015.....	$111^{+37}_{-23}$	27	16	161	0.15	0.14	0.13	0.15
NGC 6118.....	$124^{+27}_{-38}$	31	8	140	0.12	0.14	0.07	0.13
NGC 6384.....	$104^{+24}_{-24}$	26	8	185	0.12	0.13	0.08	0.12
NGC 6503.....	$86^{+6}_{-5}$	22	45	212	0.27	0.12	0.55	0.14

<sup>a</sup> RC3 isophotal radius.

different lengths, especially for the redder galaxies, in the sense that the metric radius is smaller than the isophotal radius.

Very red and very blue galaxies tend to have smaller  $R_\eta$  values in kiloparsecs. As seen in Figure 7, galaxies with  $(B-V)_T^0 > 0.8$  and  $(B-V)_T^0 < 0.5$  have  $1 < R_\eta \text{ kpc}^{-1} < 10$  and galaxies with intermediate colors [ $0.5 < (B-V)_T^0 < 0.8$ ] have systematically larger radii:  $4 < R_\eta \text{ kpc}^{-1} < 20$ . Galaxies with centrally concentrated surface brightness

profiles have  $\eta$  functions that decrease more rapidly with increasing radius (e.g., NGC 3077). In comparison, galaxies with profiles like NGC 2403 have  $\eta$  functions that roll over at a relatively larger radius than NGC 3077. Although the exponential disk profiles and  $r^{1/4}$  law are parameterized with a metric scale length, the exponential disk scale length and the effective radius are difficult to compare with  $R(\eta = \frac{1}{2})$  as they define different properties in the integrated light of the galaxies.

TABLE 5

B-BAND SAMPLE: STRUCTURAL PARAMETERS

NAME (1)	$R_\eta$ (arcsec) (2)	$R_c$ (arcsec) (3)	$R_h$ (arcsec) (4)	$R_{25}^a$ (arcsec) (5)	$\chi$			
					$R_\eta^{2/3}$ (6)	$\frac{1}{2}R_\eta$ (7)	2 kpc (8)	Model (9)
NGC 0023.....	$16^{+2}_{-2}$	7	3	64	0.13	0.11	0.11	0.21
NGC 0488.....	$36^{+16}_{-9}$	18	6	161	0.05	0.05	0.04	0.06
NGC 0520.....	$117^{+47}_{-74}$	29	6	128	0.37	0.39	0.28	0.63
NGC 1012.....	$48^{+18}_{-10}$	12	14	81	0.23	0.15	0.24	0.18
NGC 1036.....	$14^{+3}_{-2}$	7	17	46	0.24	0.09	0.62	0.24
NGC 1569.....	$27^{+8}_{-5}$	7	93	173	0.51	0.18	0.96	0.38
NGC 2403.....	$245^{+66}_{-33}$	61	103	687	0.22	0.21	0.28	0.20
NGC 6217.....	$56^{+33}_{-11}$	14	10	93	0.20	0.19	0.18	0.26
NGC 6412.....	$65^{+10}_{-7}$	16	10	77	0.21	0.21	0.20	0.00
NGC 6643.....	$91^{+14}_{-23}$	22	9	119	0.21	0.21	0.18	0.22
NGC 6764.....	$73^{+30}_{-69}$	18	5	72	0.19	0.20	0.13	0.39
NGC 7244.....	$13^{+3}_{-3}$	6	2	21	0.11	0.08	0.08	0.18
NGC 7448.....	$52^{+8}_{-7}$	13	6	83	0.22	0.20	0.17	0.23
NGC 7468.....	$12^{+3}_{-2}$	3	6	27	0.31	0.19	0.48	0.17
NGC 7469 <sup>b</sup> .....	$2^{+2}_{-0}$	1	3	45	0.16	0.07	0.79	0.37
NGC 7673.....	$14^{+3}_{-2}$	3	3	40	0.25	0.23	0.19	0.51
ARP 002.....	$69^{+22}_{-24}$	17	19	85	0.37	0.35	0.36	0.41
ARP 081.....	$44^{+28}_{-12}$	22	2	0	0.16	0.18	0.08	0.43
ARP 158.....	$27^{+4}_{-4}$	7	3	77	0.39	0.39	0.30	0.72
ARP 209.....	$20^{+2}_{-3}$	5	3	29	0.22	0.20	0.14	0.34
I ZW 207.....	$33^{+27}_{-19}$	8	3	0	0.54	0.54	0.32	0.95
UGC 12547.....	$27^{+6}_{-7}$	7	3	38	0.18	0.18	0.13	0.23
VV 790a.....	$9^{+2}_{-2}$	2	2	13	0.20	0.15	0.15	0.36

<sup>a</sup> RC3 isophotal radius.<sup>b</sup> Metric radius formulation fails.

TABLE 6  
HDF *V*-BAND METRIC RADII AND *UBVI* PHOTOMETRY

Name (1)	$R_\eta$ (arcsec) (2)	$R_c$ (arcsec) (3)	$R_h$ (arcsec) (4)	$I$ (mag) (5)	$V$ (mag) (6)	$B$ (mag) (7)	$U$ (mag) (8)
20038.....	$0.44^{+0.20}_{-0.04}$	0.20	0.16	24.75	24.75	24.78	26.52
20058.....	$0.32^{+0.04}_{-0.04}$	0.24	0.19	21.08	22.16	23.93	26.60
20105.....	$0.60^{+0.30}_{-0.08}$	0.16	0.15	23.65	24.66	25.03	25.35
20128.....	$0.36^{+0.04}_{-0.04}$	0.08	0.15	24.14	25.03	25.02	25.53
20139.....	$0.20^{+0.04}_{-0.04}$	0.16	0.15	24.10	24.52	24.71	25.49
20148.....	$1.56^{+0.46}_{-0.40}$	0.40	0.16	22.67	23.44	23.92	24.33
20156.....	$0.32^{+0.04}_{-0.04}$	0.24	0.19	22.39	22.94	23.64	24.23
20177.....	$0.24^{+0.04}_{-0.04}$	0.16	0.15	24.63	24.95	25.13	25.75
20179.....	$1.92^{+0.48}_{-0.48}$	0.48	0.15	22.74	23.62	23.97	25.06
20183.....	$0.16^{+0.04}_{-0.04}$	0.16	0.15	22.32	23.17	24.06	25.46
20190.....	$0.64^{+0.26}_{-0.08}$	0.16	0.15	23.57	24.29	24.68	25.56
20194.....	$1.68^{+0.12}_{-0.08}$	0.40	0.19	21.47	22.41	23.52	24.65
20213.....	$0.40^{+0.04}_{-0.04}$	0.32	0.43	24.10	24.32	24.74	25.56
20315.....	$2.64^{+0.04}_{-0.04}$	0.68	0.31	19.61	19.92	20.50	21.67
20316.....	$0.76^{+0.04}_{-0.04}$	0.72	0.58	18.50	19.12	20.12	22.98
20371.....	$0.32^{+0.04}_{-0.04}$	0.32	0.18	23.63	23.91	24.13	25.84
20378.....	$0.76^{+0.14}_{-0.24}$	0.36	0.16	24.17	24.36	24.55	26.33
20421.....	$0.60^{+0.30}_{-0.08}$	0.28	0.16	21.97	22.99	23.77	24.45
20456.....	$0.52^{+0.18}_{-0.04}$	0.12	0.15	23.15	24.15	24.67	25.24
20507.....	$1.48^{+0.60}_{-0.76}$	0.36	0.17	23.37	23.82	24.00	25.73
20513.....	$0.36^{+0.04}_{-0.04}$	0.16	0.15	24.73	24.91	24.92	25.68
20578.....	$1.08^{+0.04}_{-0.04}$	0.52	0.18	21.20	22.09	23.11	24.12
20587.....	$1.40^{+0.60}_{-0.36}$	0.36	0.15	23.16	23.96	24.33	24.72
20627.....	$1.00^{+0.40}_{-0.08}$	0.48	0.18	23.08	23.77	24.60	25.27
20666.....	$1.08^{+0.42}_{-0.20}$	0.28	0.15	22.10	22.38	22.49	23.06
20691.....	$1.00^{+0.50}_{-0.12}$	0.48	0.19	23.31	23.69	24.48	24.61
20785.....	$1.00^{+0.20}_{-0.08}$	0.24	0.15	22.45	23.36	23.84	24.34
20821.....	$0.88^{+0.20}_{-0.16}$	0.24	0.16	23.41	24.04	24.19	24.60
20830.....	$0.44^{+0.04}_{-0.04}$	0.12	0.17	24.55	24.59	24.72	26.43
20865.....	$1.00^{+0.10}_{-0.08}$	0.48	0.19	23.45	24.03	24.87	25.55
20896.....	$1.64^{+0.45}_{-0.76}$	0.40	0.15	22.69	23.27	23.50	23.84
30052.....	$0.24^{+0.04}_{-0.04}$	0.16	0.18	24.49	24.58	24.79	26.20
30079.....	$0.92^{+0.04}_{-0.04}$	0.44	0.19	21.98	22.70	23.66	24.44
30096.....	$1.96^{+1.00}_{-0.60}$	0.48	0.58	22.75	22.95	23.20	23.88
30100.....	$0.52^{+0.25}_{-0.04}$	0.48	0.24	23.75	24.02	24.58	25.03
30119.....	$0.80^{+0.04}_{-0.04}$	0.40	0.23	22.58	22.82	23.41	23.86
30135.....	$1.04^{+0.52}_{-0.36}$	0.24	0.15	22.83	23.59	23.96	24.28
30172.....	$0.80^{+0.40}_{-0.16}$	0.40	0.18	23.73	24.13	24.90	25.44
30176.....	$1.40^{+0.36}_{-0.20}$	0.36	0.16	23.19	23.69	24.38	24.88
30218.....	$0.56^{+0.40}_{-0.08}$	0.48	0.16	21.79	23.27	25.23	28.44
30251.....	$1.20^{+0.04}_{-0.08}$	0.32	0.17	20.91	21.90	22.83	23.63
30272.....	$0.32^{+0.08}_{-0.04}$	0.24	0.15	23.55	24.65	25.05	25.64
30288.....	$1.44^{+0.04}_{-0.04}$	0.36	0.19	20.71	21.26	22.12	22.63
30301.....	$2.40^{+0.60}_{-0.68}$	0.60	0.19	21.29	21.73	22.41	22.74
30318.....	$0.60^{+0.04}_{-0.04}$	0.28	0.23	22.59	22.77	23.29	23.64
30343.....	$0.76^{+0.30}_{-0.04}$	0.20	0.15	23.36	24.33	24.36	24.62
30352.....	$1.84^{+1.04}_{-0.92}$	0.44	0.15	22.87	23.65	24.21	23.59
30391.....	$0.96^{+0.45}_{-0.20}$	0.24	0.16	21.99	22.99	23.66	24.07
30424.....	$1.96^{+0.48}_{-0.28}$	0.48	0.23	21.29	21.70	22.50	23.13
30429.....	$1.92^{+0.68}_{-0.32}$	0.96	0.18	20.33	21.51	23.21	25.69
30440.....	$0.88^{+0.04}_{-0.04}$	0.40	0.17	22.86	23.54	24.30	25.06
30443.....	$0.56^{+0.25}_{-0.16}$	0.28	0.17	24.83	24.86	24.92	26.28
30498.....	$0.36^{+0.04}_{-0.04}$	0.32	0.15	24.47	24.97	25.09	25.72
30542.....	$0.92^{+0.04}_{-0.04}$	0.88	0.24	21.57	22.25	23.36	24.81
30585.....	$0.40^{+0.04}_{-0.04}$	0.32	0.20	23.29	23.74	24.56	24.97
30592.....	$0.48^{+0.36}_{-0.12}$	0.20	0.15	24.21	24.26	24.26	24.86
30655.....	$1.16^{+0.60}_{-0.16}$	0.32	0.17	22.44	23.01	23.67	23.77
30659.....	$0.56^{+0.34}_{-0.08}$	0.24	0.18	23.31	23.79	24.59	24.89
30670.....	$0.52^{+0.04}_{-0.04}$	0.48	0.18	21.60	22.74	24.37	26.67
30753.....	$0.44^{+0.04}_{-0.04}$	0.40	0.16	23.43	24.06	24.53	24.75
30767.....	$0.72^{+0.18}_{-0.04}$	0.20	0.18	23.88	24.00	24.26	25.83
30826.....	$1.00^{+0.08}_{-0.04}$	0.48	0.23	23.26	23.59	24.25	25.09
40057.....	$0.80^{+0.08}_{-0.08}$	0.20	0.15	22.45	23.24	23.53	23.91
40106.....	$0.64^{+0.16}_{-0.08}$	0.28	0.15	23.35	24.27	24.79	25.28

TABLE 6—*Continued*

Name (1)	$R_\eta$ (arcsec) (2)	$R_c$ (arcsec) (3)	$R_h$ (arcsec) (4)	$I$ (mag) (5)	$V$ (mag) (6)	$B$ (mag) (7)	$U$ (mag) (8)
40162.....	$0.80^{+0.04}_{-0.04}$	0.40	0.22	21.20	21.62	22.41	23.05
40178.....	$0.96^{+0.12}_{-0.08}$	0.52	0.20	22.84	23.26	24.05	24.46
40186.....	$2.16^{+0.96}_{-0.96}$	0.56	0.15	22.24	23.37	23.43	23.52
40187.....	$0.24^{+0.04}_{-0.04}$	0.16	0.15	23.58	23.98	23.96	24.04
40224.....	$0.72^{+0.28}_{-0.20}$	0.64	0.15	23.00	24.19	24.93	25.42
40335.....	$0.48^{+0.32}_{-0.04}$	0.48	0.97	24.21	24.58	25.10	26.72
40345.....	$0.60^{+0.30}_{-0.16}$	0.28	0.16	24.31	24.39	24.47	25.41
40350.....	$0.80^{+0.04}_{-0.04}$	0.40	0.18	21.68	22.15	22.68	23.01
40392.....	$1.04^{+0.46}_{-0.16}$	0.28	0.16	23.28	24.10	24.33	24.44
40408.....	$0.56^{+0.24}_{-0.08}$	0.28	0.16	23.76	24.13	24.31	25.77
40425.....	$0.32^{+0.04}_{-0.04}$	0.24	0.18	22.18	23.25	24.90	27.29
40430.....	$1.60^{+0.40}_{-0.40}$	0.40	0.15	23.21	24.01	24.05	24.49
40500.....	$2.36^{+0.64}_{-0.64}$	0.60	0.15	21.23	22.21	22.78	23.48
40515.....	$1.16^{+0.56}_{-0.28}$	0.28	0.20	23.00	23.50	24.34	24.47
40522.....	$0.44^{+0.04}_{-0.04}$	0.40	0.16	22.81	23.61	24.12	24.46
40569.....	$0.68^{+0.42}_{-0.20}$	0.64	0.17	24.06	24.57	25.05	25.32
40586.....	$0.32^{+0.20}_{-0.04}$	0.24	0.17	24.97	25.07	25.10	27.87
40603.....	$1.12^{+0.04}_{-0.04}$	0.28	0.19	20.73	21.31	22.22	22.85
40651.....	$4.16^{+2.00}_{-1.80}$	1.04	0.15	22.71	23.46	23.50	23.72
40674.....	$0.36^{+0.04}_{-0.04}$	0.32	0.15	23.15	23.52	23.61	23.86
40686.....	$0.48^{+0.22}_{-0.04}$	0.48	0.16	21.26	22.87	24.90	26.63
40709.....	$0.96^{+0.48}_{-0.28}$	0.24	0.15	22.49	23.95	24.98	25.74
40733.....	$1.00^{+0.04}_{-0.04}$	0.24	0.19	21.05	21.70	22.65	23.36
40792.....	$0.76^{+0.26}_{-0.04}$	0.36	0.16	23.57	23.95	24.34	25.45
40818.....	$0.32^{+0.18}_{-0.04}$	0.32	0.16	23.50	23.81	24.18	25.72
40822.....	$0.48^{+0.22}_{-0.12}$	0.20	0.15	24.65	24.75	24.76	25.13
40845.....	$1.08^{+0.20}_{-0.12}$	0.32	0.15	23.34	23.99	24.21	24.62
40877.....	$0.40^{+0.20}_{-0.04}$	0.40	0.16	22.54	23.89	24.96	27.16
40882.....	$0.76^{+0.38}_{-0.28}$	0.20	0.15	23.35	24.09	24.49	25.59
40901.....	$0.96^{+0.04}_{-0.04}$	0.24	0.17	22.25	22.96	23.70	23.99

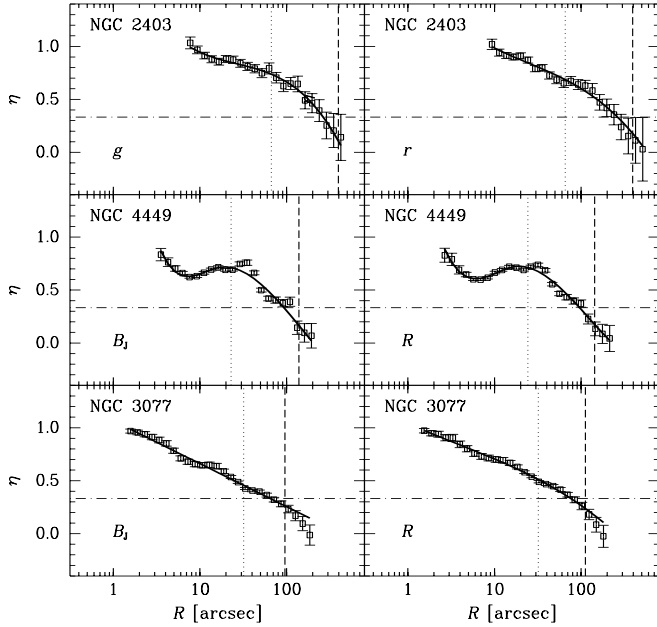


FIG. 4.— $\eta$  functions of NGC 2403, NGC 4449, and NGC 3077. The radius  $R$  is the semimajor axis of the galaxy. The error bars are  $1\sigma$  errors (see text). The left column shows the  $\eta$  functions determined in a blue band image, and the right column those determined in a red band. NGC 3077 and NGC 4449 have images in the  $B_j$  and  $R$  bands, and NGC 2403 in the  $g$  and  $r$  band. The dotted line marks the position of the core radius ( $R_c$ ), and the dashed line that of the total radius ( $R_T$ ). The  $\eta = \frac{1}{2}$  level that defines  $R_\eta$  is explicitly shown by the dot-dashed line. For NGC 2403  $R_c = 66''$ ,  $R_T = 397''.5$ , for NGC 4449  $R_c = 23''$ ,  $R_T = 139''.8$ , and for NGC 3077  $R_c = 32''.4$ ,  $R_T = 97''.2$ . The solid lines are fits to the data as explained in the text.

Concerning the high-redshift HDF data, Williams et al. (1997) measure radii ( $R_1$ ) using the FOCAS package (Valdes 1982).  $R_1$  is the intensity-weighted first-moment radius determined from pixels within the detection isophote and is essentially a metric radius. The first-moment radius is a function of the radius  $R$  that is measured relative to the center positions of the galaxy and the intensity  $I(x, y)$ :

$$R_1 = \sum R I(x, y) / \sum I(x, y). \quad (10)$$

In contrast, the metric radius used in this study is measured from the  $\eta$  profiles of the galaxies. A sample of the profiles of HDF galaxies is presented in Figure 8. Figure 9 shows the difference between the metric radii  $R_1$  and  $R_\eta$ . Systematically,  $R_\eta$  measures larger sizes than  $R_1$ .

### 3.1.3. Flux Measurement

Although the structural parameters presented in this study are independent of the photometric zero points, our photometric techniques involve somewhat unfamiliar steps. It is therefore important to compare our photometric results to the values obtained by others.

The metric radius provides a simple aperture definition to measure galaxy fluxes. The  $g$ -band fluxes measured within metric apertures using the IRAF task `polyphot` are compared with the total Johnson  $B$ -band magnitudes from the RC3 ( $B_T$ ) in Figure 10. The uncertainties in  $B_T$  are 0.2 mag.

The data of the Palomar set of the CDI have relative errors of 0.05%, i.e., completely negligible compared to other sources of errors (e.g., sky subtraction and flat-fielding).

As has been mentioned before, the Lowell set and the

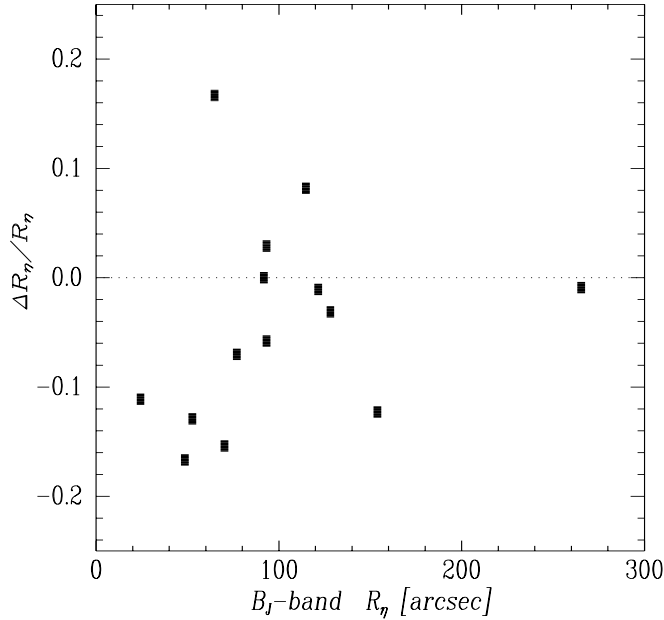


FIG. 5.—Dependence of the metric radius with wavelength. The normalized difference of the metric radii (semimajor axis lengths) in the blue and red bands:  $\Delta R_\eta/R_\eta \equiv (R_\eta^B - R_\eta^R)/R_\eta^B$  as a function of the radius in the blue band ( $R_\eta$ ). Except for NGC 2403 at  $R_\eta > 200''$ , which was observed through  $g$  and  $r$ , the rest are values measured in the  $B_J$  and  $R$  bands.  $R_\eta$  is in units of arcseconds.

KPNO sample were obtained under nonphotometric conditions and are therefore excluded from the plot in Figure 10. A linear fit through the data points results in a slope of 0.95 with a standard deviation of 0.20 mag. Even though the

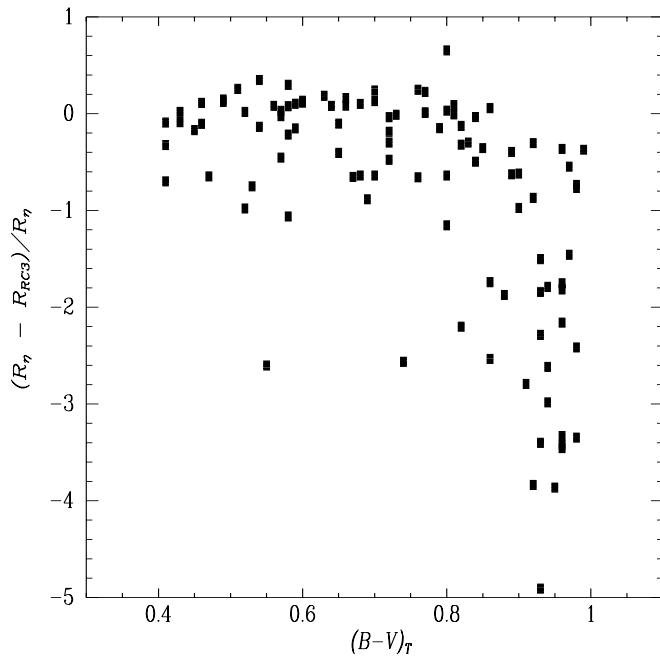


FIG. 6.—Comparison of metric and isophotal diameters as a function of color. Plotted are the nearby galaxies with available RC3  $(B-V)_T$  colors. Galaxies redder than  $(B-V)_T > 0.8$  have measured metric sizes that are systematically smaller than their isophotal sizes. The two lower points at  $\Delta R/R \sim -2.6$  are NGC 5033 [ $(B-V)_T = 0.55$ ] and NGC 2985 [ $(B-V)_T = 0.74$ ] and the point at  $\Delta R/R \sim 0.65$  and  $(B-V)_T = 0.8$  is NGC 4157.

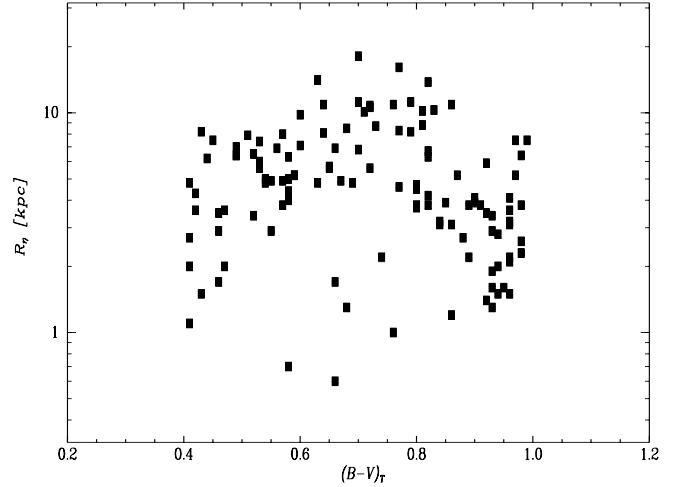


FIG. 7.—Metric radius as a function of  $(B-V)_T$  color. Galaxies with colors in the range  $0.6 < (B-V)_T < 0.8$  tend to have the largest physical radii in kiloparsecs in the sample. The reddest galaxies do not have the largest metric sizes.

$g$ -band and  $B$ -band fluxes are measured within different apertures, the percentage difference in magnitudes  $[(g - B_T)/g]$  shows no trend with the size of the aperture.

With respect to the HDF data, both Sawicki et al. (1997) and I measure fluxes using metric apertures and the resulting AB magnitudes are directly compared in Figure 11. The AB magnitude system is defined as  $m_{AB} = -2.5 \times \log f_\nu - 48.60$ , where  $f_\nu$  is the flux in  $\text{ergs cm}^{-2} \text{s}^{-1} \text{Hz}^{-1}$  and the constant is chosen such that  $AB = V$  for an object with a flat spectrum (Oke & Gunn 1983). Sawicki et al. measure “total” fluxes using the Picture Processing Package (PPP) (Yee 1991), which uses certain characteristics of the growth curve to define the fluxes, very similar to that of the total asymptotic magnitudes in the RC3, and

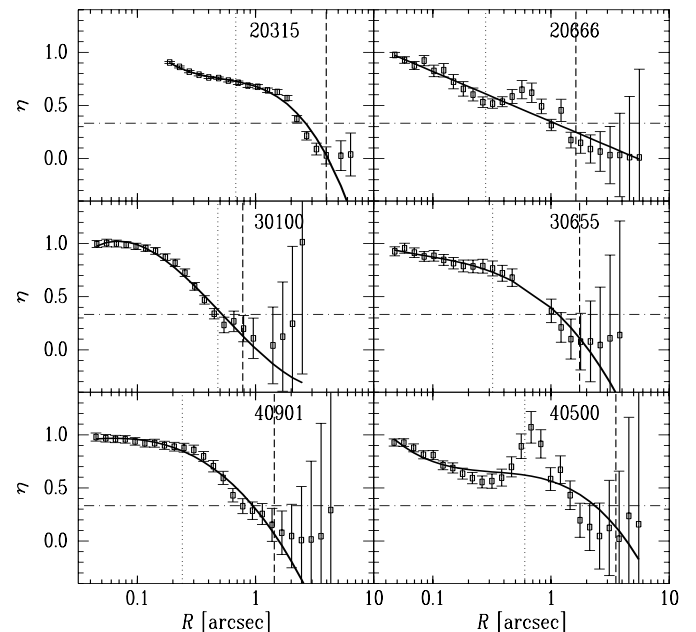


FIG. 8.— $\eta$  functions of HDF galaxies. The identification numbers of the galaxies are indicated in each panel. The profiles were measured in the  $V$  band. See the legend of Fig. 4 for a description of the plots.



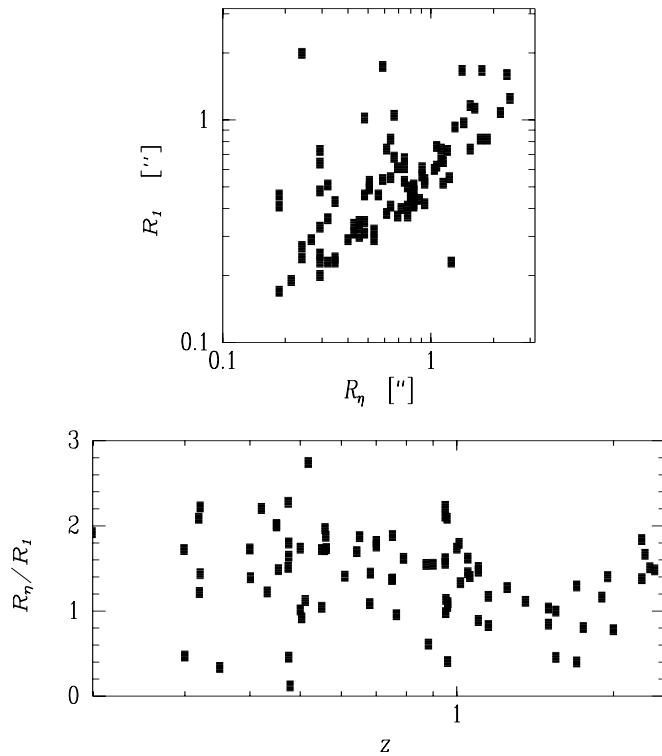


FIG. 9.—Comparison of galaxy sizes in the HDF. Not shown in the lower panel are galaxies with redshifts smaller than 0.2.

consequently can be associated with a metric radius. Therefore, we expect the PPP fluxes and the fluxes measured using  $R_\eta$  to be very similar. I compute AB magnitudes using the photometric zero points given by Ferguson (1996) but averaged over all the WF chips given that the difference between the zero points in each WF chip are smaller than

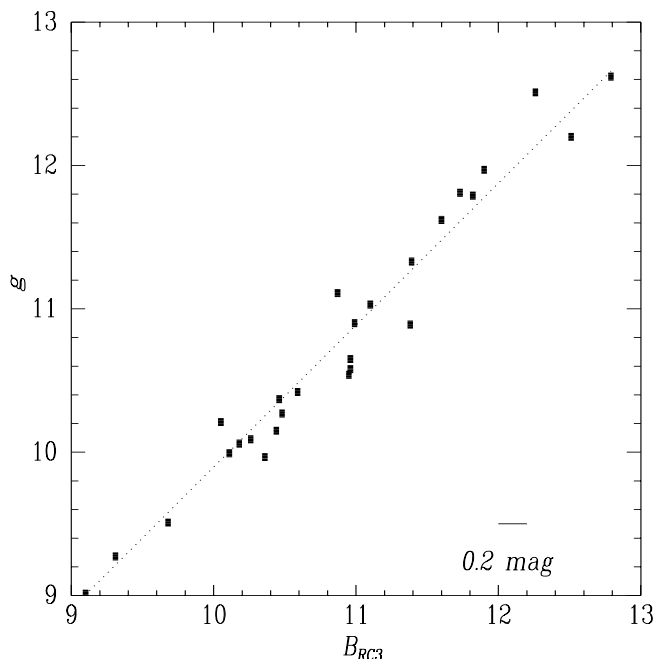


FIG. 10.—Comparison of  $g$ -band fluxes (this work) and  $B$ -band magnitudes (RC3). Typical errors in  $B_{RC3}$  amount to  $\sim 0.2$  mag and in  $g$  the Poisson errors are smaller than the size of the points ( $< 0.005$  mag).

0.03 mag. The AB magnitudes zero points used are presented in Table 1. In general there is good agreement between both measurements although, as seen in Figure 11, the agreement is worst in the  $U$  band where the galaxies tend to be fainter. The data points with the largest residuals in the  $U$  band (Fig. 11, *open squares*) also tend to have the largest residuals in the other bands. Linear fits, excluding these data points, result in standard deviations of 0.40, 0.32, 0.28, and 0.26 mag in the  $U$ ,  $B$ ,  $V$ , and  $I$  bands, respectively. The data points are plotted along with a best linear fit with the standard deviations listed above, and a line with slope equal to one for reference. The agreement is good, but the large systematic scatter more prominent in  $B$  may reflect the treatment of the superpositions of source in the PPP, which was neglected in this study.

### 3.2. Normalized High Spatial Frequency Power: $\chi$

Having defined and developed a method to measure characteristic lengths and fluxes, we turn to the problem of quantifying the high spatial frequency power ( $\chi$ ), which is the flux contained within scales smaller than that of the largest star-forming regions. To keep this quantity distance independent, it is normalized by the total flux of the galaxy. Defined in this fashion, the structural parameter  $\chi$  depends on an associated length (e.g.,  $R_\eta$ ,  $R_d$ ,  $D_c$ ) and should be related to the current star formation rate in galaxies.

To estimate  $\chi$  I construct a high spatial frequency image, which is the difference between a low spatial frequency image and the original image. Fluxes are measured within elliptical apertures of the absolute residual ( $f_h$ ) and original ( $f$ ) images and their ratio defines the quantity  $\chi$ :

$$\chi = \frac{f_h}{f}. \quad (11)$$

Typically, the central regions of galaxies contain high spatial frequency flux from a bulge component and Population I stars. Although there is ample evidence from spectroscopic and narrowband imaging data that star formation is present in the cores of galaxies (see, e.g., Devereux & Hameed 1997), in general in broadband images the contribution from each of these stellar populations cannot be distinguished unambiguously. Therefore the computation of  $\chi$  excludes the flux in the nuclear regions of the galaxy. Depending on the shape of the  $\eta$  profile, the adopted nuclear radius  $R_c$  scales with  $R_\eta$  with a factor 1,  $\frac{1}{2}$ , or  $\frac{1}{4}$ . Galaxies with profiles like NGC 2403 (see Fig. 4) have core sizes  $R_c = \frac{1}{4}R_\eta$ ; galaxies with profiles like NGC 3031 have  $R_c = \frac{1}{2}R_\eta$ ; and galaxies with profiles like NGC 3077 have  $R_c = 1R_\eta$ .

The outer edge of the galaxies is set to  $R_T = 1.5 \times R_\eta$ . The flux within this outer limit includes more than  $\sim 90\%$  of the total flux of the galaxy as illustrated in the growth curves in Figure 12. In summary,  $\chi$  measures the flocculency within an annulus of outer radius  $R_T$  and inner radius  $R_c$ , both of which are simple multiples of  $R_\eta$ .

#### 3.2.1. Methods

Two methods were used to construct the low spatial frequency images. One method, more suitable for symmetrical images, uses isophotal ellipse fits of the original image to construct a smooth, noiseless model of the low-frequency galaxy. A second method consists of median filtering the original image with a sliding square window, the size of

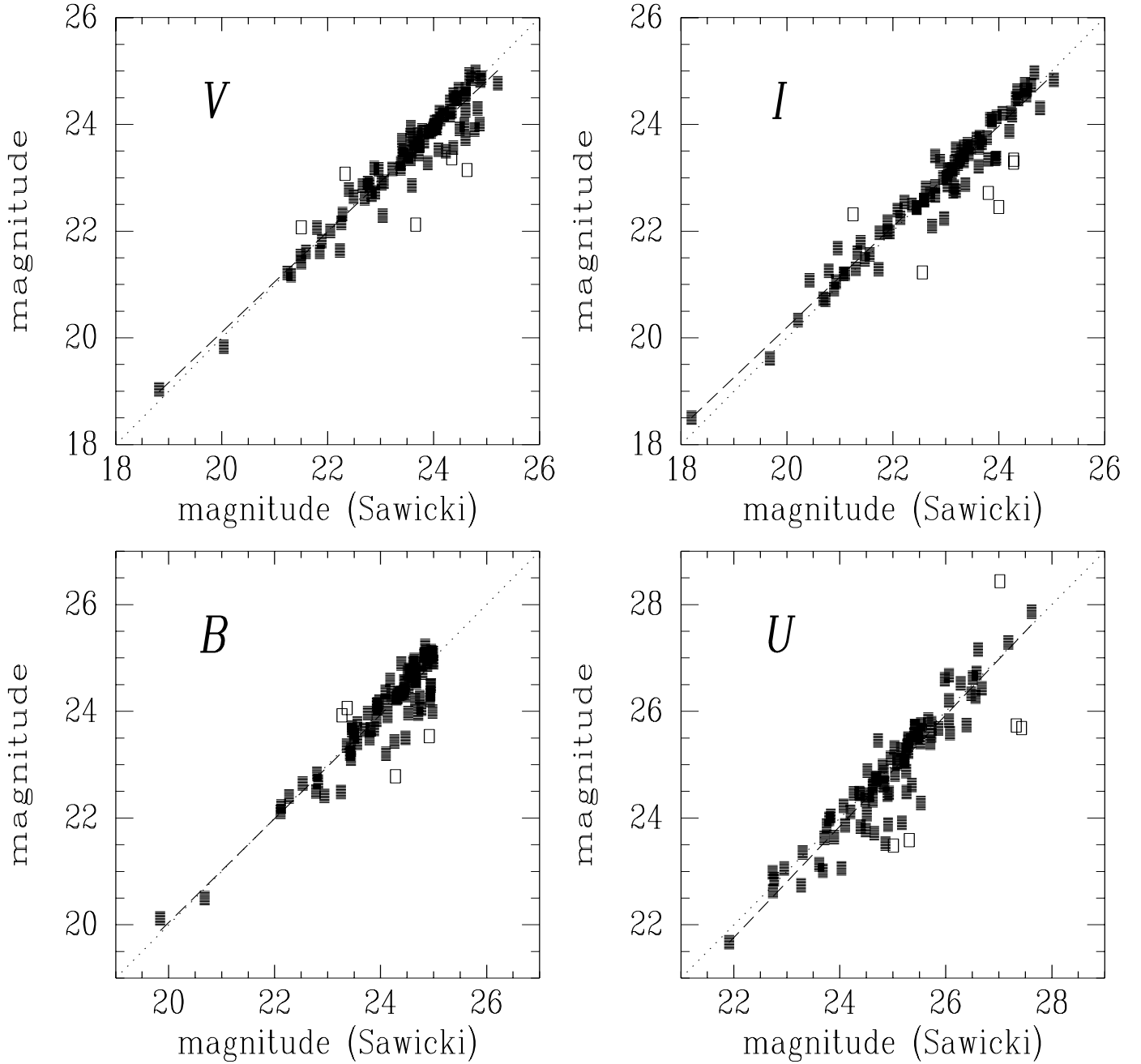


FIG. 11.—Comparison of magnitudes in the HDF. The results in all four bands are presented with the magnitudes determined by Sawicki et al. (1997) in the horizontal axis and those determined in this work in the vertical axis. The magnitudes are referred to the AB photometric system. The dashed line shows the best fit to the data, and the dotted line shows, for reference, a line with slope of 1. The open squares indicate the data points with the largest deviations to the fit in the U band. They were excluded from the fits in all the four bands.

which is scaled by  $R_\eta$ . Both methods will be discussed in the following.

The ellipse model method consists of constructing a noiseless model of the galaxy. The same resulting isophotal fits produced in the construction of the  $\eta$  function in § 3.1 are used, namely, the one-dimensional intensity distribution as a function of polar angle ( $\theta$ ):

$$I = \sum_{i=0}^n [A_i \sin(i\theta) + B_i \cos(i\theta)] .$$

Near the galaxy center, the fits are done in steps of a few pixels to subpixels, and toward the edges the steps are

coarser, up to 20 pixels. The resulting table of radii and intensities is interpolated with a cubic spline function to resample all radii. The intensities at each radius taken from the resampled fits are used to model a two-dimensional smooth, noiseless image: the low spatial frequency image. Example isophotal models and the residual high spatial frequency image for NGC 3810 are displayed in Figure 13.

The construction of the isophotal model resembles those produced by other authors (Odewahn 1997) who use, however, higher order harmonics ( $< 8$ ) than used here ( $\leq 2$ ). The work presented here includes up to second-order harmonics because when including third and fourth orders the

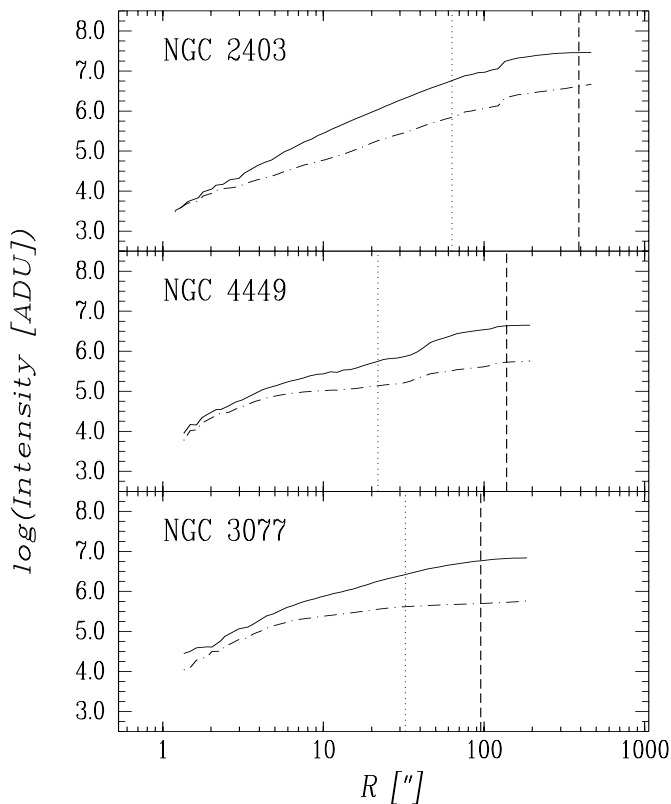


FIG. 12.—Illustration of growth curves of nearby galaxies. Shown are the cumulative intensities in ADU as a function of galactocentric radius  $R$  in arcseconds for three galaxies: NGC 2403, NGC 3077, and NGC 4449. The intensities of the original image (*solid line*) and the high spatial frequency image using the  $w = R^{2/3}$  method (*dot-dashed line*) are shown. The inner ( $R_i$ ) and the outer ( $R_o$ ) radii are indicated by the dotted and dashed vertical lines, respectively. The outer radius does not contain all of the light of the galaxy, but it does include more than 90% of the light.

reconstructed image contains spurious features (Fig. 13d). When using even higher order harmonics (fifth and sixth), the model resembles the original image very closely, in fact reproducing even the high-frequency patterns that, for our purposes, should not be contained in the smooth model.

The ellipse model method requires that the two-dimensional light distribution be well approximated by ellipses. For most irregular galaxies and a large number of spiral galaxies such fits are unrealistic. Consequently it is desirable to try other methods to estimate  $\chi$  that do not depend on the harmonic orders or on the details of the interpolation function. An alternative method to estimate  $\chi$  is to filter the image, for instance using a two-dimensional Fourier filter (Burkhead & Matuska 1980) or a sliding window (Isserstedt & Schindler 1986). In either case, a characteristic length is needed to set the size of the filtering window.

In this study, I chose to use the median filtering method primarily because of the simplicity of the coding. Other filtering methods in Fourier space or using wavelets are as valid and should be further explored (see, however, Lazzati 1995). To determine how the derived values of  $\chi$  depend on the size of the sliding window, I used different square window sizes ranging from 5 pixels to roughly 200 pixels. Families of  $\chi$  values for a few galaxies are shown in Figure 14. As expected, very small windows result in  $\chi \rightarrow 0$  and very large windows give  $\chi \rightarrow 1$ .

There are many choices for a definition of the size of the sliding window. The diameters of giant star-forming regions measured in the Milky Way and external galaxies are typically smaller than 1–2 kpc (van den Bergh 1981; Kennicutt & Hodge 1984; Hodge 1987; Kennicutt 1988; Elmegreen et al. 1994). Choosing filtering window sizes that encompass a projected 2 kpc size at the distance of the galaxy results in values of  $\chi$ , which depend on knowing the distance to the galaxy and, more importantly, assumes that galaxies have sizes of star-forming regions that, contrary to what has been discussed previously, are independent of the properties of the galaxies. We seek instead filtering windows with axis lengths  $w = aR_\eta^b$ . The result in the Appendix ( $D_c \propto R_\eta^{0.6-0.7}$ ) motivates the case of  $b \neq 1$ . As a compromise of the results reported in § 3.1, a filtering window of the form  $w = R_\eta^{2/3}$  is considered, where  $w$  and  $R_\eta$  are expressed in kiloparsecs.

Although it is not ideal to define a structural parameter that strongly depends on the distance to the galaxy, for comparison a projected 2 kpc-sized window is also considered in this study. Along with the two  $\chi$  values measured with the window sizes discussed above, I also present results obtained using a window size  $w = \frac{1}{2}R_\eta$  and using the ellipse model. In general these four points are located before the steep rise of  $\chi$  with  $w$  in Figure 14, so that in principle any one is a reasonable choice. The resulting values of  $\chi$  with the different methods are presented in Figure 15. The case is less compelling for the isophotal and 2 kpc-sized window, as has been argued above. Owing to the existing relation between the sizes of star-forming regions and metric radii (Fig. 36), I restrict the discussion of  $\chi$  to values measured with  $w = R_\eta^{2/3}$ . The values of  $\chi$  for the 135 nearby galaxies are presented in Tables 3, 4, and 5.

The  $\chi$  values determined using all four different methods are compared with two star formation indices in Figure 16. The correlations between  $\chi$  and SFR indices are low, which reflects the fact that  $\chi$  measures a small absolute quantity. From all the methods, the results using the ellipse model correspond to the highest  $\chi$  values, with the most deviant points corresponding to asymmetrical galaxies (NGC 4242, NGC 4826, NGC 5746). The fixed 2 kpc-sized window overestimates  $\chi$  for the redder galaxies and for the nearer galaxies. The SFR indices considered in the comparison are the  $B-V$  color and the H $\alpha$  EW. All the methods indicate that  $\chi$  is related to the star formation rate in galaxies. The method that uses a window size that depends on the metric radius as a power of  $\frac{2}{3}$  ( $w = R_\eta^{2/3}$ ) has a number of nice features that makes it preferable over the others. It has the smallest scatter, especially in galaxies with redder colors and smaller H $\alpha$  EWs. Another feature is that, unlike the model method, it does not depend on whether the shape of the galaxy can be well approximated by elliptical isophotes at all radii. Finally, given the empirical relations between the largest star-forming regions and the metric radii in equation (A1) it is more difficult to argue in favor of the  $\frac{1}{2}R_\eta$  method. These reasons suggest that the best choice of the filtering window size has the form  $R_\eta^{2/3}$ .

This choice, however, does not preclude contamination to the high spatial frequency image from structures such as spiral arms or rings. The flux within these coherent structures is expected to increase the values of  $\chi$ . The ellipse model method does a better job at separating spiral patterns and rings from the high spatial frequency image. When comparing the results of the model method with the

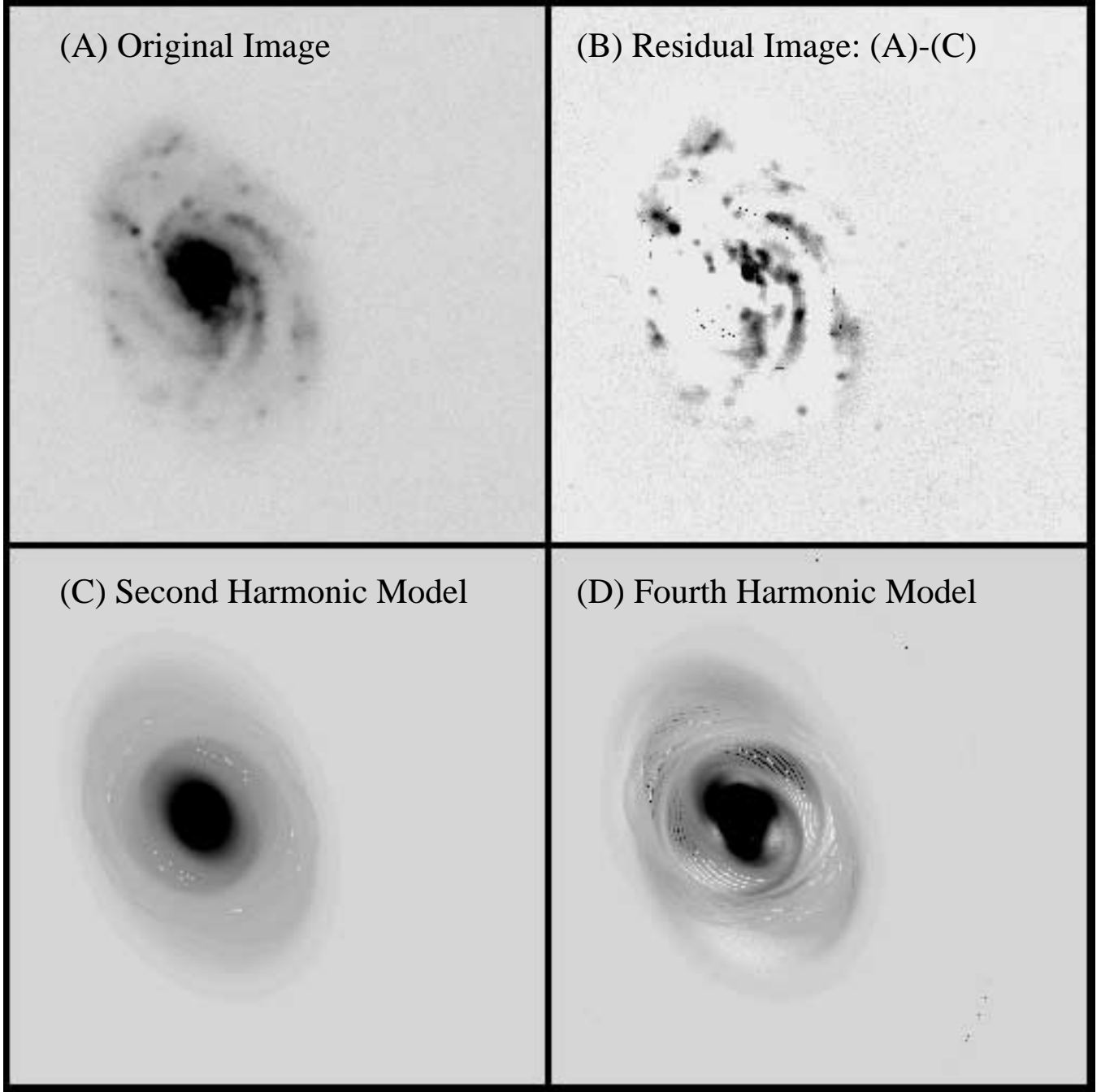


FIG. 13.—Isophotal models of NGC 3810 are shown in (c) and (d) with low and high harmonic orders, respectively. (a) Shows the original  $B_J$ -band image of NGC 3810, and (b) shows the difference between the original image and the low-order model in (c).

method using  $w = R_\eta^{2/3}$ , there is no indication of an over-estimation of  $\chi(R_\eta^{2/3})$  (Fig. 16). The contributions to  $\chi$  of spiral arms and rings are within the estimated errors of  $\chi$ .

As for the multiplicative factor, it was chosen so that  $w$  corresponds to the knee feature in the curve of  $\chi$  versus  $w$  (see Fig. 14). The result is that  $a \sim 1$  for all galaxies when  $R_\eta$  and  $w$  are expressed in kiloparsecs.

In summary, to compute the value of  $\chi$  for a galaxy, first the  $\eta$  profile is constructed and the radius at which  $\eta$  reaches  $\frac{1}{3}$  defines the galaxy's characteristic length  $R_\eta$ . Second, the image is median filtered using a window size of  $w = R_\eta^{2/3}$  to construct a smooth model of the galaxy and its residual map. Fluxes of the original image and of the absolute values

of the residual image are measured within annuli of semi-major axis length between  $R_c$  and  $R_T$ . The ratio of these fluxes equals  $\chi$ . Overall,  $\chi$  does appear to be a reasonable quantity to measure the flocculency as it is larger in galaxies that look lumpier, as illustrated in Figure 17, and that have bluer  $B - V$  colors and larger H $\alpha$  EWs.

### 3.2.2. Sources of Error in $\chi$

In this section, I will discuss the influence on the measurement of  $\chi$  of the bandpass of the image used, the angular resolution in the image, the signal-to-noise ratio in the image, and the contribution of the core flux to the total flux of the galaxy.

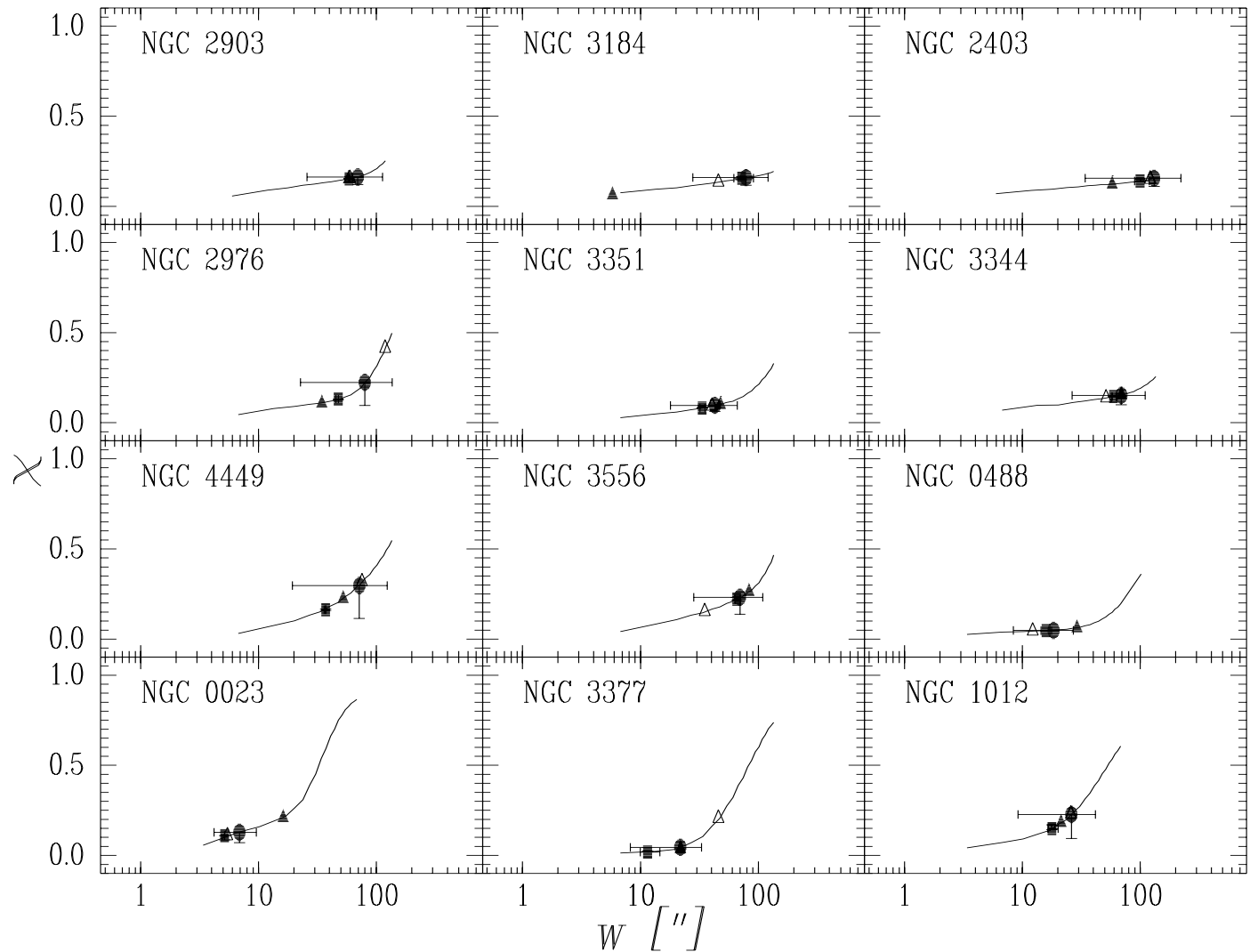


FIG. 14.—Families of  $\chi(w)$  for a number of galaxies are plotted. Identified are four values of  $\chi$  from the isophotal model (filled triangle) and from median filtering using the projected 2 kpc-sized window (open triangle),  $\frac{1}{2}R_n$  (filled square), and  $R_n^{2/3}$  (filled circle).

**Bandpass.**—Optical images taken at different rest frame wavelengths reveal different structures in galaxies (O’Connell & Marcum 1997). Broadband images at  $\sim 4000$  Å show O and B type stars that trace star-forming regions. On the other hand, at longer wavelengths around  $\sim 7000$  Å both old and young stellar populations contribute to the flux of the galaxy. This difference is manifested as lower

values of  $\chi$  in the  $R$  band than in the  $B_J$  band (Fig. 18) and, as will be shown in § 6, is consistent with what is found in the HDF sample (Fig. 25). The metric radius is an important parameter in determining  $\chi$ . A dependence of the metric radius on wavelength could be related to a dependence of  $\chi$  on wavelength. However, for the wavelength range considered in this study (4000–7000 Å), the metric radius changes undetectably (Fig. 5). Therefore the metric radius does not introduce the trend of  $\chi$  with wavelength in the range under study. In summary, the systematic decrease of  $\chi$  with increasing wavelengths does reflect the familiar result that galaxies appear lumpier at shorter wavelengths.

**Angular Resolution.**—Images with lower angular resolution were simulated to study the effects introduced in  $\chi$  of the decrease in resolution. The values of  $\chi$  change only slightly when artificially decreasing the angular resolution of an image. This was found in a subsample of 27 galaxies with Hubble morphological types ranging from  $-5$  to  $11$ . The effect of lower resolution is illustrated in Figure 19, which presents the results obtained on NGC 4449. The original image of NGC 4449 in the  $B_J$  band with an angular scale of  $1''.35 \text{ pixel}^{-1}$  was binned by 2–5 times to simulate a decrease in angular resolution. The simulated pixels

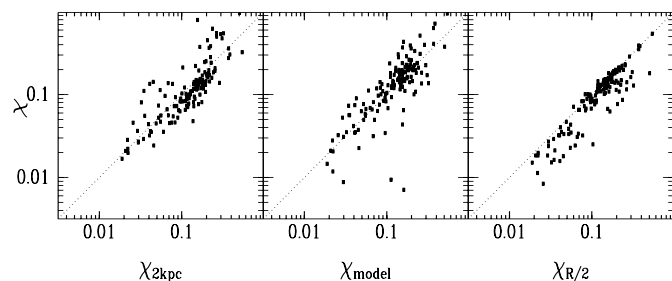


FIG. 15.—Values of  $\chi$  for each method. In each panel, the vertical axis is the  $\chi$  value using a window size equal to  $R_n^{2/3}$ . The horizontal axis corresponds to each of the other three methods described in the text. For reference, the dotted line with slope 1 is shown.

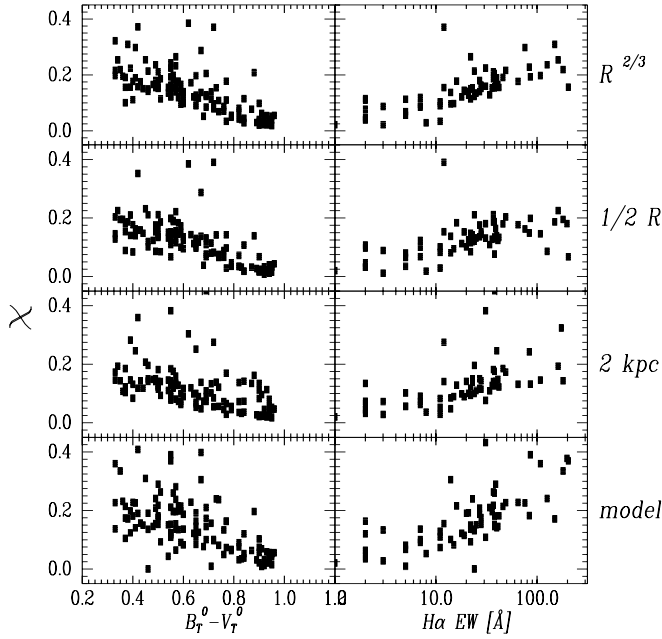


FIG. 16.—High spatial frequency powers extracted using four different methods (described in the text) compared with two star formation indices, the  $B - V$  color, and the  $H\alpha$  EWs.

measure  $2''.69$ ,  $5''.35$ ,  $10''.56$ , and  $13''.2$ , which correspond to projected scales of  $\sim 40$  pc,  $\sim 80$  pc,  $\sim 160$  pc, and  $\sim 200$  pc, respectively. Depending on the redshift of the galaxy, in the HDF each pixel of size  $0''.04$  corresponds to roughly 20–1000 pc. The sizes of the images are in decreasing order: 157, 79, 40, and 32 pixels on a side.

The difference in  $\chi$  between the unbinned and the binned images increases in absolute value with increasing binning factor. Denoting by  $\chi_b$  where  $b = 2, 4, 8$  the value of  $\chi$  for a binning  $b$ , the 27 galaxies show medians and standard deviations of  $(\chi - \chi_2)_{1/2} = -0.04$  with  $\sigma_{\chi - \chi_2} = 0.05$ ,  $(\chi - \chi_4)_{1/2} = -0.08$  with  $\sigma_{\chi - \chi_4} = 0.05$ , and  $(\chi - \chi_8)_{1/2} = -0.2$  with  $\sigma_{\chi - \chi_8} = 0.25$ . Large decreases in angular resolution affect  $\chi$  mildly as long as the resolution element is smaller than  $\sim 160$  pc.

**Noise.**—The range in background noise of the nearby galaxy images is wide. However, within this range, there is no systematic trend between  $\chi$  and noise (Fig. 20). For a given data set,  $\chi$  is largely unaffected by the level of the sky noise.

**Core Flux.**—In addition to galaxies with active nuclei, amidst the cores of many galaxies there is ongoing star formation (e.g., Devereux & Hameed 1997). Crowding of stars in the cores of galaxies limits the usefulness of the method developed in this study in the central parts of galaxies. To study the innermost regions of galaxies, not only should the angular resolution be very high (mapping a few parsecs) but a different method should be used to study the high spatial frequency distribution of matter in the cores of galaxies. In this method, we are forced to exclude the core region altogether and constrain the measurement of the *flocculency* to the disk of galaxies. The core flux can contribute to a large percentage of the total flux. For example, broadband images of a bulge-dominated galaxy and a galaxy containing a single high surface brightness star-forming region can be indistinguishable from one another by our technique. As a result, both galaxies will have very

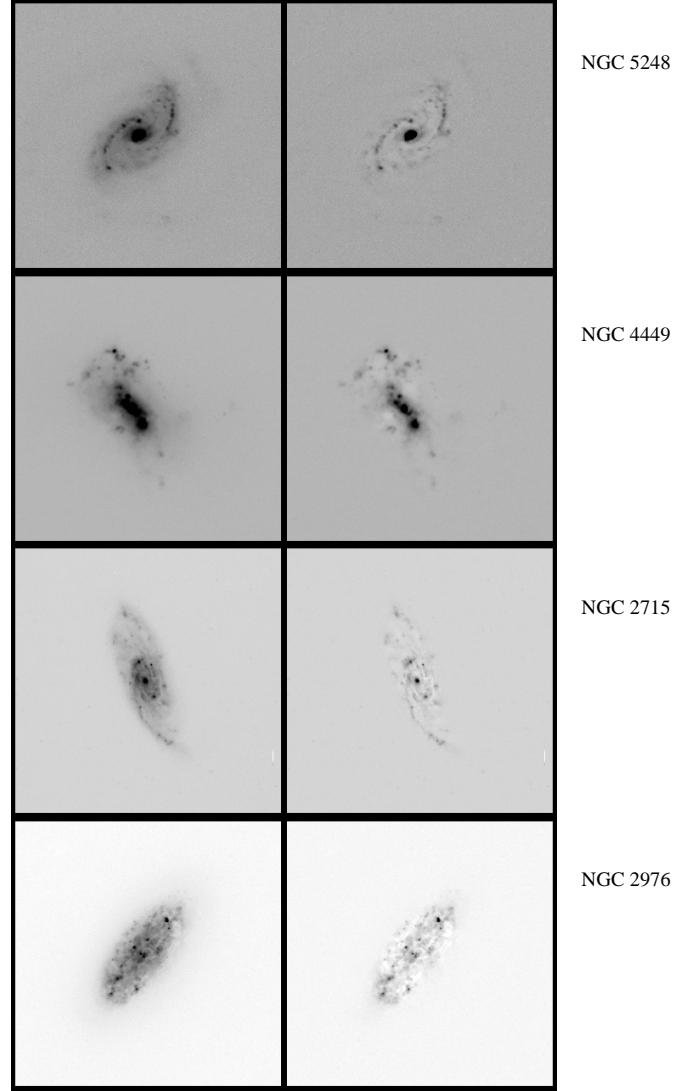


FIG. 17.—Illustration of high spatial frequency images of nearby galaxies.

similar values of  $\chi$  in spite of the differences in the galaxies. To exclude this possibility, the core flux is removed from the calculation of  $\chi$ . The core region is an elliptical aperture defined by the semimajor axis length  $R_c$ .  $R_c$  is a function of  $R_\eta$  and the  $\eta$  profile.  $R_c$  takes the value  $\frac{1}{4}R_\eta$  when the  $\eta$  profile is of the form of NGC 2403,  $\frac{1}{2}R_\eta$  when it is like NGC 3031, and  $1R_\eta$  when it is like NGC 3077. The central region of each galaxy is carefully examined to verify that the chosen core aperture does in fact exclude the core flux. In some galaxies with NGC 3031-type profiles it was found that the core apertures were either too big or too small. In these cases the apertures were enlarged to  $1R_\eta$  or diminished to  $\frac{1}{4}R_\eta$ . Note that  $R_c$  can only have the values  $\frac{1}{4}R_\eta$ ,  $\frac{1}{2}R_\eta$ , and  $1R_\eta$  with the exception of two galaxies: NGC 2976 and NGC 4527. NGC 2976 has no detectable core. The core of NGC 4527 was better fit with  $R_c = \frac{1}{3}R_\eta$ . In the entire sample of 135 galaxies, 12% have  $R_c = 1R_\eta$ , 24% have  $R_c = \frac{1}{2}R_\eta$ , and 62% have  $R_c = \frac{1}{4}R_\eta$ . The effect of correcting for the core contribution is shown in Figure 21. This correction affects mostly the lowest values of  $\chi$ , which, as expected, can be artificially overestimated since cores can have significant power in small scales.

TABLE 7  
B<sub>J</sub>-BAND SAMPLE: CI

NAME	CI	
	This Study	Abraham et al. 1996b
NGC 2715.....	0.335	0.166
NGC 2768.....	0.515	0.473
NGC 2775.....	0.466	0.447
NGC 2976.....	0.299	0.155
NGC 2985.....	0.498	0.433
NGC 3077.....	0.490	0.205
NGC 3079.....	0.444	0.369
NGC 3147.....	0.440	0.385
NGC 3166.....	0.595	0.408
NGC 3184.....	0.229	0.139
NGC 3344.....	0.357	0.190
NGC 3351.....	0.439	0.428
NGC 3368.....	0.555	0.402
NGC 3377.....	0.490	0.746
NGC 3379.....	0.541	0.733
NGC 3486.....	0.476	0.195
NGC 3556.....	0.321	0.146
NGC 3596.....	0.377	0.186
NGC 3623.....	0.424	0.352
NGC 3631.....	0.346	0.211
NGC 3672.....	0.381	0.195
NGC 3675.....	0.419	0.259
NGC 3726.....	0.255	0.090
NGC 3810.....	0.458	0.187
NGC 3877.....	0.413	0.286
NGC 3893.....	0.441	0.179
NGC 3938.....	0.400	0.163
NGC 3953.....	0.397	0.267
NGC 4013.....	0.247	0.404
NGC 4030.....	0.508	0.240
NGC 4088.....	0.308	0.162
NGC 4123.....	0.296	0.147
NGC 4125.....	0.504	0.729
NGC 4136.....	0.340	0.155
NGC 4144.....	0.384	0.207
NGC 4157.....	0.430	0.226
NGC 4242.....	0.236	0.146
NGC 4340.....	0.472	0.461
NGC 4365.....	0.529	0.739
NGC 4374.....	0.533	0.710
NGC 4406.....	0.479	0.739
NGC 4429.....	0.500	0.469
NGC 4442.....	0.593	0.761
NGC 4449.....	0.442	0.133
NGC 4450.....	0.462	0.255
NGC 4472.....	0.530	0.754
NGC 4477.....	0.516	0.661
NGC 4486.....	0.534	0.778
NGC 4487.....	0.303	0.149
NGC 4526.....	0.586	0.523
NGC 4564.....	0.576	0.791
NGC 4593.....	0.457	0.402
NGC 4594.....	0.465	0.431
NGC 4621.....	0.533	0.715
NGC 4636.....	0.484	0.747
NGC 4710.....	0.588	0.371
NGC 4731.....	0.300	0.151
NGC 4754.....	0.583	0.767
NGC 4826.....	0.383	0.223
NGC 4861.....	0.243	0.229
NGC 4866.....	0.392	0.514
NGC 5005.....	0.480	0.420
NGC 5204.....	0.328	0.174
NGC 5248.....	0.381	0.238
NGC 5322.....	0.529	0.768

TABLE 7—Continued

NAME	CI	
	This Study	Abraham et al. 1996b
NGC 5334.....	0.208	0.183
NGC 5364.....	0.360	0.204
NGC 5371.....	0.333	0.175
NGC 5377.....	0.515	0.522
NGC 5585.....	0.358	0.230
NGC 5669.....	0.321	0.162
NGC 5701.....	0.567	0.754
NGC 5746.....	0.488	0.636
NGC 5792.....	0.374	0.238
NGC 5813.....	0.484	0.507
NGC 5850.....	0.434	0.437
NGC 5985.....	0.343	0.171
NGC 6015.....	0.391	0.213
NGC 6118.....	0.272	0.142
NGC 6384.....	0.427	0.219
NGC 6503.....	0.479	0.137

### 3.3. Comparison of $\chi$ with Other Structural Parameters

Recently two quantitative structural parameters, the concentration index (CI) and the asymmetry (A), have been defined for the purpose of identifying the nature of distant galaxies observed with the *HST* (Abraham et al. 1996a). The relationships of these parameters to the high spatial frequency power  $\chi$  and star formation rate indices are compared in this section.

Different ways to define the concentration index result in essentially equivalent parameters (Okamura et al. 1984) and the bulge-to-disk ratio and concentration index are well correlated with each other (Kent 1985). In the following we will use the definition of Abraham et al. (1994) of the concentration index. They define CI as the flux within two radii:

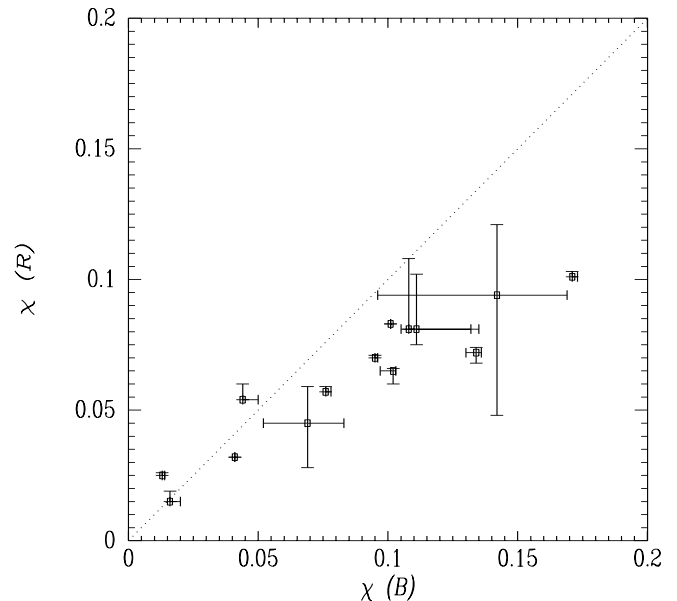


FIG. 18.—Dependence of  $\chi$  on wavelength. High spatial frequency power measured in a red band [ $\chi(R)$ ] and a blue band [ $\chi(B)$ ]. The error bars reflect the uncertainty in  $R_*$ . For reference, a line with slope of 1 is plotted (dotted line).

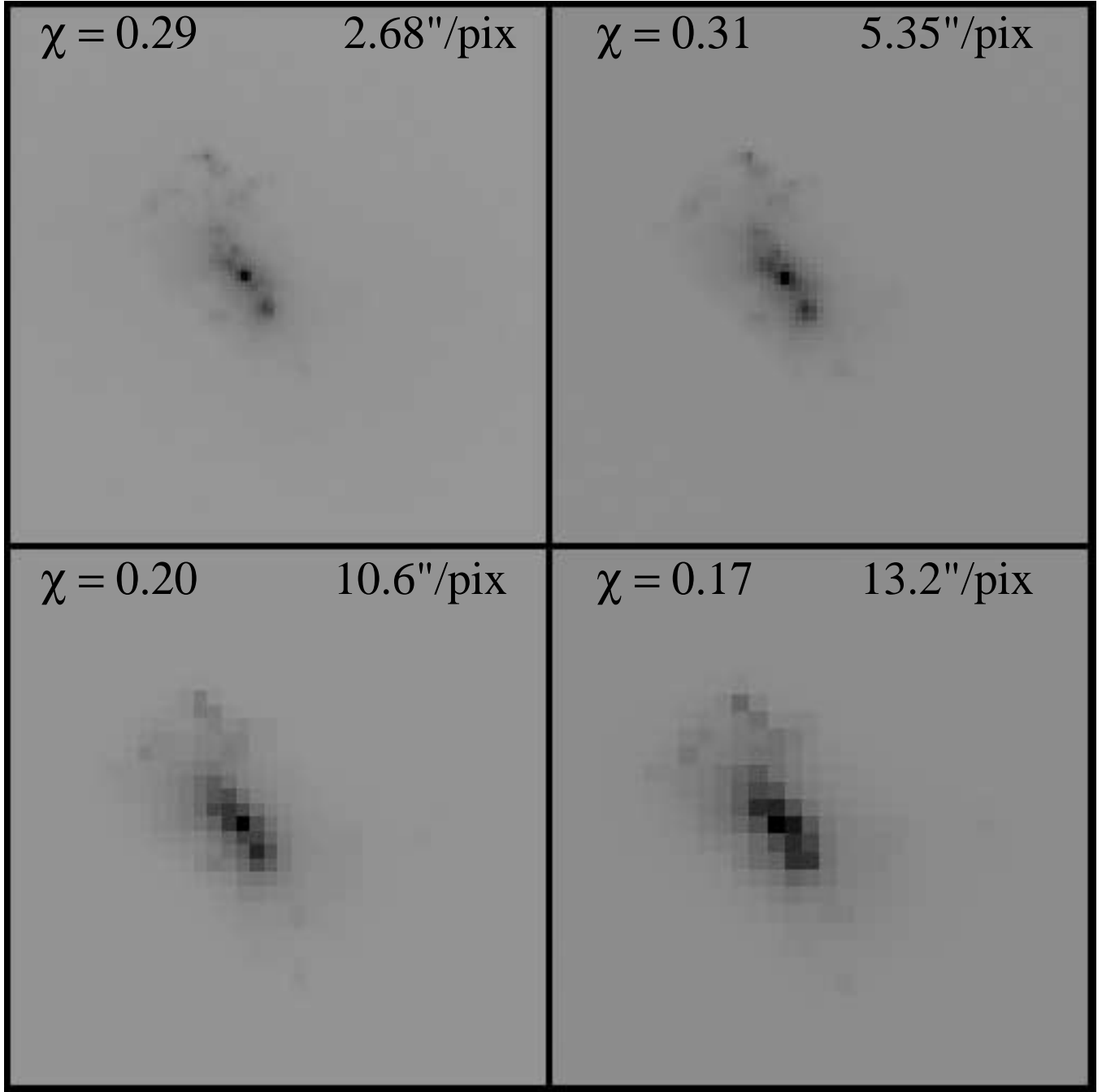


FIG. 19.—Effect of decreasing the angular resolution on NGC 4449. Indicated in each panel are the resolution per pixel and measured values of  $\chi$

$$\text{CI} = \frac{\int_0^{r_2} r' I(r') dr'}{\int_0^{r_1} r' I(r') dr'}.$$

Abraham et al. (1994) use  $r_1 = r$  and  $r_2 = \alpha r$  ( $\alpha = 0.3$ ); instead I use  $r_1 = R_c$  and  $r_2 = R_T$ .

An asymmetry parameter was introduced in the context of galaxy structure (Abraham et al. 1996b). The idea behind this parameter, as its name suggests, is to measure the degree of azimuthal symmetry<sup>7</sup> present in the galaxy. The asymmetry has been defined as the absolute value of the residual flux after subtracting the original image from itself rotated by 180°. To obtain a dimensionless parameter the residual flux is normalized by the total flux.

In Figure 22, I show the concentration index and asymmetry parameter against  $(B-V)_T^0$  and H $\alpha$  emission. As expected, the overall trends are that bulge-dominated galaxies have redder  $(B-V)_T^0$  colors and smaller H $\alpha$  EW. The concentration index turns out to be a very useful parameter as it links the stellar composition of the galaxy with its appearance in a quantitative way. However, it has been suggested that the wide range in current star formation rates compared to the small range in concentration index indicate that the latter is not probing directly current star formation, but rather the past average star formation

<sup>7</sup> Comment: as opposed to the asymmetry parameter,  $\chi$  measures irregularity in terms of the lumpiness.



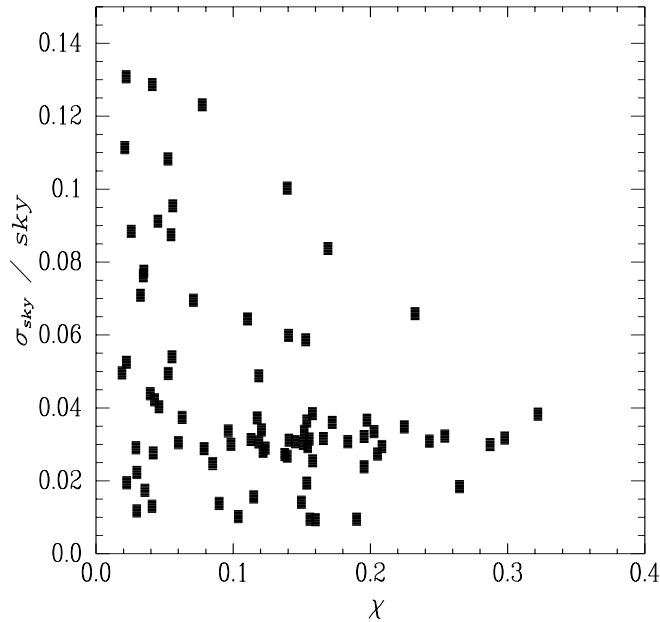


FIG. 20.—Dependence of  $\chi$  on sky noise. Plotted are  $\chi$  and the ratio of the sky noise ( $\sigma_{\text{sky}}$ ) over the sky level measured within an area of  $7.2 \times 11.5$  of the  $B_J$ -band data of the Frei et al. (1996) sample.

history (Kennicutt et al. 1994). If this is the case and the shapes of galaxies are a strong function of the current star formation rate, then other structural parameters should be explored.

The asymmetry, like the  $\chi$  parameter, is by construction sensitive to the presence of irregularities such as H II regions, tails, bridges, and dust lanes indicative of recent star formation and should complement the information extracted from CI and  $\chi$ . For example, the asymmetry parameter is high in galaxies that are smooth but highly

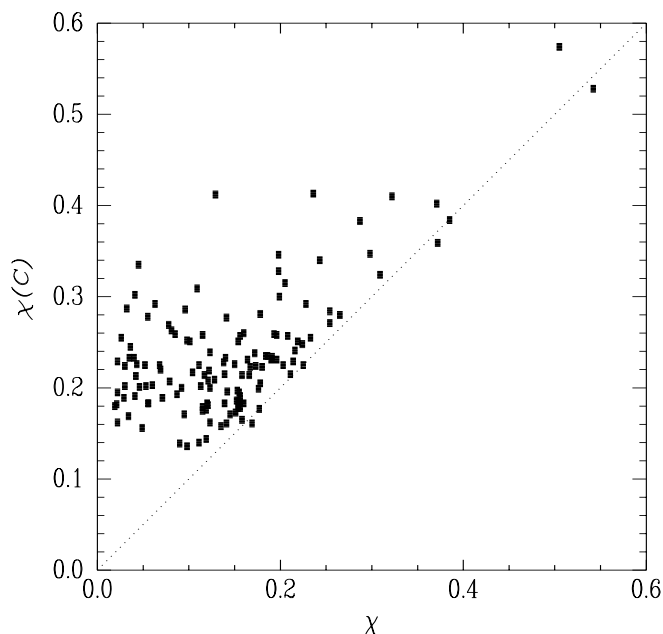


FIG. 21.—Dependence of  $\chi$  on core flux. The vertical axis  $\chi(C)$  is measured over the whole galaxy including the core flux. The horizontal axis is the nominal value of  $\chi$ , i.e., corrected for the contribution of the core. For reference, a slope of 1 line (dotted line) is plotted.

asymmetric (NGC 5746) ( $A = 0.2$ ,  $\chi = 0.14$ ). On the other hand, galaxies that are symmetric but lumpy (e.g., NGC 3184:  $A = 0.01$ ,  $\chi = 0.16$ ) have small values of  $A$  but large values of  $\chi$ . The asymmetry parameter measures a small amplitude signal that makes it harder to determine with precision. The trends of the asymmetry with color and H $\alpha$  EW seen in Figure 22 are not as evident as in the case of CI.

Abraham et al. (1996a, 1996b) measure the concentration indices of 82 galaxies in the CDI sample. These measurements agree with the CI measurements done in this study (Fig. 23). Nevertheless there are a number of substantial departures that may be the result of choosing different core radii. There are notable deviations pointed out in Figure 23. NGC 4866 (*asterisk*) by inspection is morphologically similar to NGC 4429 (*open circle*) yet Abraham et al.'s value assigns a concentration index that is closer to the morphologically very different NGC 3877 (*open square*). Another departure pointed out in Figure 23 is NGC 4013 (*open triangle*). This galaxy is viewed edge-on and contains mostly a core; however, the values of the concentration indices are very different. For a direct case-by-case comparison, I provide the data of Figure 23 in Table 7.

We can now directly compare the  $\chi$  parameter with the concentration index and asymmetry parameter. The  $\chi$ -A-CI planes in Figure 24 verify that  $\chi$  and CI are correlated with each other in the sense that smooth galaxies are centrally concentrated. However, there are a number of galaxies that lie off this band of  $\chi$ -CI. These galaxies are lumpier than expected for their degree of concentration. There is no evident relationship between  $\chi$  and  $A$ . There are many galaxies that are symmetric and lumpy, i.e., small  $A$  and large  $\chi$ : NGC 3184, NGC 5334, NGC 4242, NGC 3184, NGC 5669, NGC 4861, but there are a few galaxies that are asymmetric and smooth: NGC 3377, NGC 4526, NGC 5746, and NGC 3077.

#### 4. $\chi$ AT HIGH REDSHIFT

The parameter  $\chi$  is defined with the expectation that it is related to the star formation rate in galaxies. As illustrated in Figure 16, all methods used to calculate  $\chi$  show the trend that higher values of  $\chi$  do reflect higher rates of star forma-

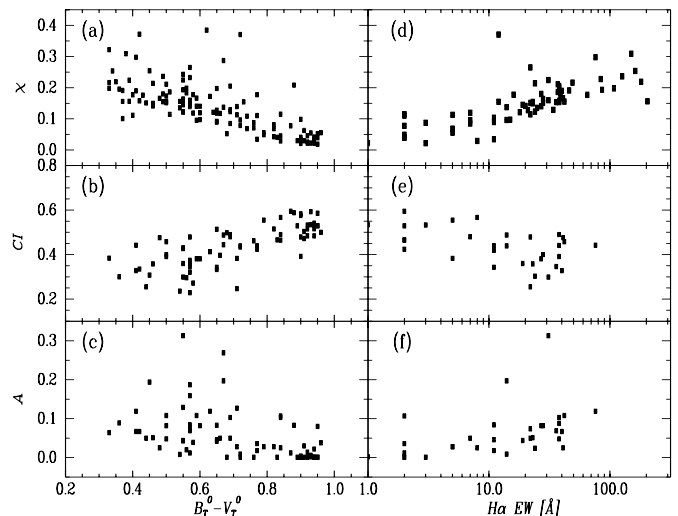


FIG. 22.—Asymmetry, concentration index, and  $\chi$  parameters compared to star formation rate indices.

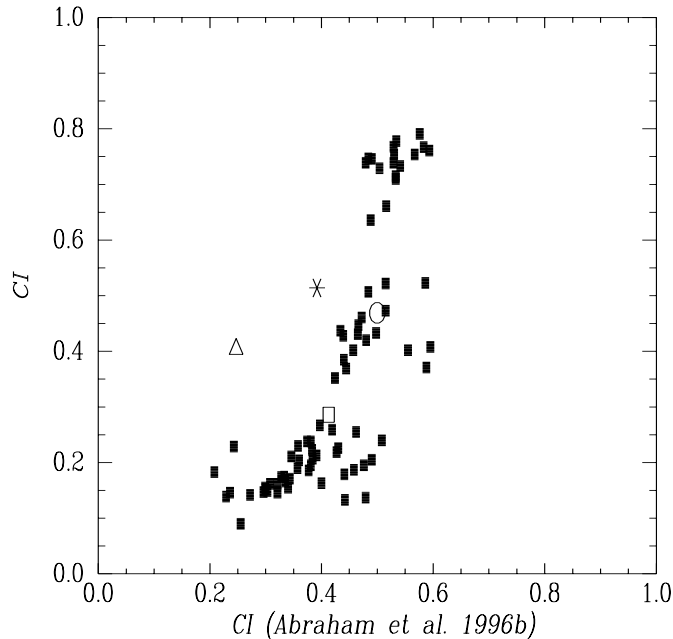


FIG. 23.—Comparison of concentration indices. Two galaxies with notable departures are pointed out: NGC 4866 (*asterisk*) and NGC 4013 (*open triangle*). Also indicated are NGC 4429 (*open circle*) and NGC 3877 (*open square*).

tion as measured by the  $B-V$  color and  $H\alpha$  EW. Next the method developed to estimate  $\chi$  is applied to the images of distant galaxies.

The amount of information that can be extracted from a two-dimensional image depends on the available number of information elements (pixels) and the width of the point-spread function (PSF). If a galaxy extends across few pixels and is sampled by only a few PSFs, very little useful structural information can be extracted. Further, when the noise increases or the surface brightness limit increases there will be a bias toward the higher surface brightness regions and, as a result, we perceive galaxies to be selectively more lumpy (Ellis 1997). With these issues in mind, one has to be

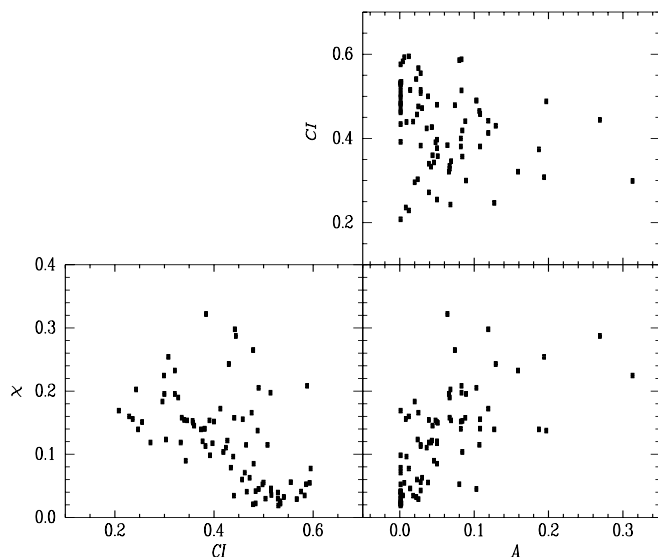


FIG. 24.— $\chi$ -A-CI planes. The values of CI and A are taken from the study of Abraham et al. (1996a, 1996b).

cautious when interpreting results concerning the morphology of high-redshift galaxies if their angular sizes are small compared to the size of the filtering window. For example, a distant galaxy detected as a single bright star-forming region is structurally indistinguishable from a core-dominated galaxy. Without multicolor or spectroscopic data, both could have similar  $\chi$  values and both will be classified as ellipticals.

The HDF data offer the advantage of studying  $\chi$  in multiple bands. The values of  $\chi$  in all four  $UBVI$  bands are presented in Table 8 for the 94 galaxies with  $B \leq 25$  mag. These data are plotted as a function of redshift in Figure 25. At shorter wavelengths  $\chi$  increases and has a larger dispersion. In the  $U$  band some values are artificially high because of the low signal-to-noise ratio. (From the definition of  $\chi$  in eq. [11], when both the numerator and denominator approach zero,  $\chi \rightarrow \infty$ . The numerator almost always differs from zero, since it is the sum of the absolute values in the residual image, and in fact when considering pure sky frames  $\chi$  increases beyond 1.)

The value of  $\chi$  is compared to the morphological types determined by van den Bergh et al. (1996) and optical colors ( $B-V$  and  $V-I$ ) measured by Sawicki (1997) in Figure 26. The data plotted are for the HDF sample with redshifts smaller than 1.2. Consistent with the trends found in the nearby sample of galaxies in Figure 16 suggesting a relation between the star formation rate and  $\chi$ , there are trends with the morphological types and colors in the sense that higher  $T$  types and bluer optical colors have larger  $\chi$ . There is,

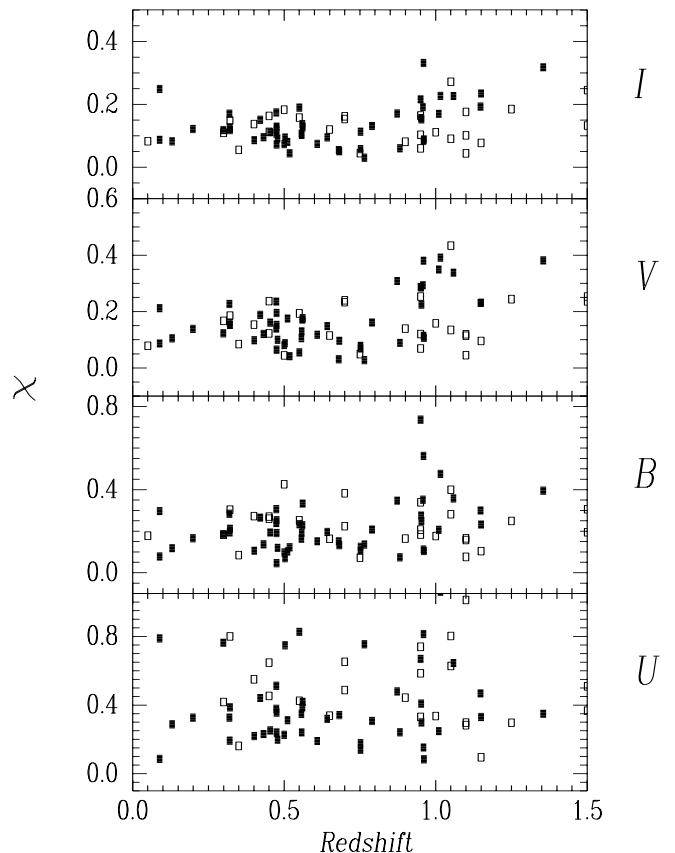


FIG. 25.— $UBVI$  high spatial frequency powers in the HDF as a function of redshift. Spectroscopic redshifts (*filled squares*) and photometric redshifts (*open squares*) are plotted. The range and dispersion of  $\chi$  increases with shorter wavelengths.

TABLE 8  
HDF-BAND SAMPLE:  $\chi$

NAME	$\chi(I)$				$\chi(V)$				$\chi(B)$				$\chi(U)$			
	$R_{\eta}^{2/3}$	$\frac{1}{2}R_{\eta}$	2 kpc	Model	$R_{\eta}^{2/3}$	$\frac{1}{2}R_{\eta}$	2 kpc	Model	$R_{\eta}^{2/3}$	$\frac{1}{2}R_{\eta}$	2 kpc	Model	$R_{\eta}^{2/3}$	$\frac{1}{2}R_{\eta}$	2 kpc	Model
20038.....	0.16	0.08	0.04	1.10	0.13	0.05	0.02	0.41	0.17	0.09	0.05	1.82	0.31	0.44	0.41	42.60
20058.....	0.07	0.04	0.12	0.11	0.06	0.03	0.11	0.04	0.05	0.04	0.07	12.64	0.24	0.29	0.21	...
20105.....	0.10	0.08	0.05	0.20	0.12	0.08	0.07	0.16	0.18	0.17	0.15	2.37	0.33	0.31	0.28	11.59
20128.....	0.19	0.05	0.10	0.44	0.24	0.04	0.13	0.48	0.25	0.07	0.15	2.21	0.30	0.17	0.23	13.57
20139.....	0.08	0.01	0.08	0.36	0.10	0.02	0.10	0.13	0.11	0.04	0.11	2.62	0.14	0.11	0.14	21.46
20148.....	0.16	0.15	0.10	0.30	0.23	0.22	0.13	0.29	0.38	0.37	0.26	2.79	0.65	0.64	0.61	14.67
20156.....	0.09	0.02	0.16	0.24	0.10	0.05	0.17	0.05	0.12	0.03	0.19	6.23	0.20	0.17	0.24	39.89
20177.....	0.07	0.02	0.07	0.41	0.18	0.02	0.10	0.07	0.11	0.04	0.11	2.31	0.09	0.09	0.09	15.49
20179.....	0.19	0.15	0.07	0.38	0.29	0.27	0.10	0.41	0.35	0.31	0.21	2.35	1.14	1.11	1.07	26.09
20183.....	0.08	0.02	0.08	0.33	0.11	0.03	0.11	0.29	0.11	0.03	0.11	7.09	0.15	0.12	0.15	82.51
20190.....	0.13	0.05	0.05	0.25	0.24	0.12	0.06	0.17	0.19	0.10	0.10	2.99	0.37	0.29	0.29	26.34
20194.....	0.12	0.08	0.07	0.27	0.15	0.13	0.05	0.22	0.25	0.23	0.22	7.62	1.18	1.18	1.18	67.05
20213.....	0.08	0.01	0.36	0.57	0.11	0.04	0.45	0.13	0.12	0.06	0.34	3.72	0.29	0.34	0.36	30.92
20315.....	0.12	0.11	0.06	0.76	0.14	0.14	0.07	0.22	0.17	0.16	0.11	3.55	0.33	0.32	0.26	36.95
20316.....	0.09	0.02	0.31	0.33	0.09	0.03	0.31	0.03	0.08	0.02	0.29	5.69	0.09	0.09	0.13	...
20371.....	0.06	0.02	0.02	0.55	0.10	0.04	0.03	0.22	0.07	0.04	0.04	2.46	0.48	0.38	0.38	44.33
20378.....	0.17	0.12	0.10	0.75	0.23	0.14	0.07	0.32	0.22	0.18	0.15	1.94	1.39	1.37	1.51	43.44
20421.....	0.11	0.08	0.05	0.22	0.08	0.05	0.05	0.25	0.12	0.10	0.07	4.55	0.14	0.12	0.11	24.07
20456.....	0.10	0.04	0.04	0.29	0.11	0.08	0.06	0.26	0.17	0.09	0.09	3.19	0.28	0.24	0.24	19.12
20507.....	0.30	0.25	0.08	0.60	0.39	0.34	0.09	0.56	0.41	0.36	0.16	1.64	1.78	1.71	1.64	36.99
20513.....	0.20	0.07	0.12	0.92	0.21	0.04	0.11	0.33	0.25	0.11	0.18	1.76	0.33	0.25	0.30	11.77
20578.....	0.11	0.07	0.03	0.32	0.11	0.09	0.05	0.35	0.16	0.13	0.10	6.64	0.35	0.34	0.36	52.99
20587.....	0.16	0.15	0.08	0.19	0.25	0.21	0.11	0.25	0.34	0.32	0.21	2.56	0.59	0.59	0.45	13.65
20627.....	0.16	0.07	0.07	0.40	0.19	0.14	0.09	0.40	0.25	0.17	0.17	4.45	0.43	0.36	0.36	30.49
20666.....	0.32	0.23	0.08	1.15	0.38	0.28	0.10	0.74	0.39	0.31	0.12	2.14	0.35	0.28	0.13	12.13
20691.....	0.11	0.08	0.08	0.59	0.12	0.10	0.08	0.23	0.26	0.21	0.21	4.32	0.45	0.43	0.43	14.80
20785.....	0.11	0.07	0.04	0.13	0.16	0.11	0.05	0.16	0.18	0.15	0.12	2.93	0.34	0.31	0.27	16.34
20821.....	0.15	0.11	0.09	0.35	0.24	0.22	0.15	0.26	0.22	0.20	0.17	1.85	0.49	0.43	0.41	10.30
20830.....	0.22	0.09	0.05	1.14	0.27	0.12	0.05	0.39	0.27	0.14	0.08	1.91	0.59	0.51	0.47	37.07
20865.....	0.16	0.09	0.12	0.32	0.24	0.14	0.14	0.14	0.27	0.20	0.23	4.65	0.65	0.58	0.62	28.35
20896.....	0.19	0.17	0.11	0.39	0.23	0.23	0.10	0.29	0.30	0.27	0.20	2.15	0.47	0.46	0.46	10.76
30052.....	0.08	0.01	0.15	0.96	0.18	0.02	0.18	0.14	0.10	0.05	0.18	2.57	0.31	0.29	0.27	33.23
30079.....	0.13	0.06	0.09	0.42	0.20	0.15	0.11	0.43	0.19	0.13	0.15	5.28	0.36	0.31	0.33	31.15
30096.....	0.25	0.23	0.24	0.83	0.21	0.17	0.20	0.22	0.30	0.28	0.29	2.34	0.79	0.78	0.79	17.58
30100.....	0.11	0.05	0.14	0.77	0.17	0.08	0.20	0.38	0.18	0.12	0.20	3.53	0.42	0.44	0.40	26.53
30119.....	0.17	0.08	0.17	0.94	0.23	0.12	0.23	0.16	0.28	0.16	0.28	3.28	0.33	0.21	0.33	16.14
30135.....	0.16	0.13	0.08	0.51	0.29	0.25	0.11	0.69	0.28	0.24	0.17	2.48	0.41	0.39	0.38	11.16
30172.....	0.18	0.16	0.16	0.61	0.04	0.03	0.03	0.21	0.43	0.40	0.40	4.16	1.39	1.38	1.38	24.62
30176.....	0.18	0.15	0.11	0.66	0.22	0.19	0.11	0.23	0.36	0.34	0.25	4.21	0.88	0.86	0.82	23.31
30218.....	0.05	0.02	0.02	0.33	0.03	0.02	0.02	0.03	0.15	0.16	0.16	15.45	...	...	...	...
30251.....	0.10	0.08	0.03	0.13	0.15	0.13	0.06	0.18	0.20	0.18	0.12	5.20	0.32	0.31	0.26	35.35
30272.....	0.04	0.02	0.02	0.15	0.04	0.03	0.03	0.07	0.08	0.07	0.07	3.32	0.30	0.30	0.30	19.26
30288.....	0.11	0.09	0.06	0.62	0.14	0.13	0.07	0.37	0.24	0.22	0.16	5.53	0.38	0.35	0.28	31.46
30301.....	0.17	0.17	0.09	0.56	0.24	0.24	0.09	0.28	0.31	0.31	0.18	3.91	0.51	0.51	0.41	17.77
30318.....	0.13	0.04	0.18	0.87	0.16	0.10	0.22	0.17	0.19	0.08	0.26	3.29	0.19	0.09	0.25	15.18
30343.....	0.23	0.13	0.08	0.62	0.23	0.14	0.08	0.19	0.23	0.15	0.12	1.86	0.33	0.28	0.27	9.19
30352.....	0.22	0.22	0.18	0.00	0.29	0.29	0.22	0.00	0.74	0.74	0.60	...	0.67	0.67	0.62	...
30391.....	0.13	0.09	0.05	0.17	0.16	0.14	0.07	0.22	0.21	0.17	0.12	3.69	0.31	0.28	0.26	17.65
30424.....	0.12	0.11	0.06	0.58	0.15	0.14	0.08	0.18	0.21	0.20	0.15	4.28	0.39	0.38	0.33	25.27
30429.....	0.04	0.05	0.01	0.12	0.04	0.04	0.02	0.05	0.12	0.13	0.10	10.74	1.33	1.33	1.32	...
30440.....	0.14	0.06	0.06	0.21	0.17	0.12	0.07	0.13	0.23	0.14	0.14	4.58	0.39	0.28	0.28	34.54
30443.....	0.18	0.12	0.12	1.13	0.19	0.11	0.07	0.55	0.19	0.13	0.11	1.77	0.76	0.76	0.69	24.30
30498.....	0.18	0.19	0.19	0.35	0.12	0.08	0.08	0.22	0.16	0.18	0.18	1.84	1.01	0.97	0.97	13.16
30542.....	0.12	0.08	0.10	0.24	0.12	0.08	0.10	0.25	0.19	0.16	0.18	6.01	0.76	0.75	0.76	49.34
30585.....	0.09	0.01	0.15	0.36	0.10	0.04	0.16	0.12	0.11	0.06	0.15	4.96	0.22	0.18	0.22	25.39
30592.....	0.12	0.07	0.07	1.22	0.18	0.09	0.06	0.64	0.14	0.08	0.08	1.70	0.23	0.21	0.21	12.03
30655.....	0.13	0.10	0.07	0.75	0.18	0.16	0.08	0.31	0.33	0.27	0.18	3.76	0.42	0.35	0.29	12.41
30659.....	0.07	0.03	0.07	0.38	0.08	0.05	0.08	0.09	0.10	0.06	0.10	4.80	0.23	0.18	0.23	21.16
30670.....	0.19	0.13	0.13	1.25	0.06	0.03	0.03	0.06	0.23	0.20	0.20	10.56	0.83	0.88	0.88	97.73
30753.....	0.05	0.04	0.05	0.08	0.10	0.05	0.07	0.07	0.13	0.12	0.13	3.62	0.34	0.31	0.34	14.78
30767.....	0.27	0.15	0.04	0.96	0.28	0.13	0.04	0.26	0.37	0.20	0.06	2.05	0.51	0.44	0.37	33.16
30826.....	0.15	0.10	0.12	0.60	0.19	0.11	0.15	0.17	0.30	0.24	0.27	3.15	0.80	0.67	0.76	25.61
40057.....	0.15	0.10	0.04	0.26	0.22	0.16	0.08	0.29	0.25	0.19	0.10	2.38	0.30	0.24	0.16	12.69
40106.....	0.08	0.06	0.04	0.10	0.14	0.09	0.06	0.13	0.16	0.14	0.11	3.11	0.44	0.44	0.39	17.08

TABLE 8—*Continued*

NAME	$\chi(I)$				$\chi(V)$				$\chi(B)$				$\chi(U)$			
	$R_{\eta}^{2/3}$	$\frac{1}{2}R_{\eta}$	2 kpc	Model	$R_{\eta}^{2/3}$	$\frac{1}{2}R_{\eta}$	2 kpc	Model	$R_{\eta}^{2/3}$	$\frac{1}{2}R_{\eta}$	2 kpc	Model	$R_{\eta}^{2/3}$	$\frac{1}{2}R_{\eta}$	2 kpc	Model
40162.....	0.06	0.03	0.06	0.52	0.08	0.05	0.06	0.08	0.08	0.05	0.08	4.69	0.16	0.13	0.16	28.57
40178.....	0.15	0.10	0.10	0.59	0.19	0.12	0.12	0.38	0.27	0.21	0.21	4.82	0.44	0.40	0.40	23.81
40186.....	0.33	0.33	0.15	0.51	0.38	0.40	0.20	0.46	0.56	0.56	0.37	1.76	0.81	0.81	0.69	6.03
40187.....	0.09	0.02	0.09	0.42	0.11	0.02	0.11	0.22	0.10	0.02	0.10	1.87	0.08	0.03	0.08	7.47
40224.....	0.06	0.04	0.00	0.20	0.07	0.07	0.07	0.03	0.21	0.21	0.22	3.33	0.74	0.76	0.81	16.27
40335.....	0.08	0.05	0.51	0.27	0.08	0.06	0.55	0.07	0.18	0.19	0.40	2.91	2.13	2.38	2.05	55.66
40345.....	0.19	0.11	0.08	1.17	0.17	0.11	0.08	0.59	0.25	0.17	0.13	2.01	0.35	0.32	0.32	17.30
40350.....	0.10	0.08	0.05	0.54	0.13	0.09	0.06	0.22	0.19	0.17	0.11	3.45	0.24	0.22	0.17	16.24
40392.....	0.17	0.15	0.08	0.40	0.31	0.27	0.12	0.47	0.35	0.31	0.19	2.04	0.48	0.46	0.39	8.10
40408.....	0.13	0.07	0.05	0.57	0.19	0.11	0.04	0.23	0.15	0.09	0.07	2.11	0.61	0.57	0.55	30.82
40425.....	0.09	0.00	0.15	0.12	0.09	0.04	0.15	0.07	0.07	0.04	0.10	11.02	0.75	1.01	0.75	...
40430.....	0.23	0.21	0.11	0.41	0.34	0.31	0.13	0.37	0.36	0.34	0.22	1.62	0.64	0.63	0.58	9.15
40500.....	0.23	0.23	0.08	0.39	0.39	0.39	0.12	0.50	0.48	0.48	0.21	0.00	1.06	1.06	0.86	20.03
40515.....	0.14	0.12	0.10	0.44	0.15	0.14	0.10	0.15	0.27	0.26	0.24	4.34	0.55	0.54	0.50	15.70
40522.....	0.06	0.03	0.04	0.16	0.07	0.03	0.05	0.17	0.11	0.08	0.10	3.59	0.18	0.18	0.18	19.73
40569.....	0.12	0.09	0.09	0.64	0.11	0.07	0.07	0.72	0.16	0.13	0.13	3.40	0.34	0.33	0.33	17.11
40586.....	0.10	0.03	0.03	0.85	0.13	0.02	0.02	0.37	0.12	0.04	0.04	2.01	0.98	0.93	0.93	101.87
40603.....	0.11	0.07	0.06	0.40	0.16	0.12	0.08	0.23	0.19	0.15	0.12	5.44	0.25	0.22	0.19	31.37
40651.....	0.27	0.25	0.11	0.71	0.43	0.47	0.15	0.75	0.40	0.38	0.22	1.92	0.63	0.61	0.51	7.92
40674.....	0.08	0.04	0.04	0.48	0.10	0.05	0.05	0.16	0.10	0.06	0.06	2.26	0.10	0.07	0.07	9.67
40686.....	0.03	0.02	0.02	0.43	0.03	0.02	0.02	0.02	0.14	0.14	0.14	15.91	0.75	0.73	0.73	...
40709.....	0.09	0.08	0.04	0.32	0.13	0.12	0.06	0.14	0.28	0.26	0.22	5.48	0.80	0.82	0.79	33.31
40733.....	0.10	0.05	0.05	0.35	0.12	0.08	0.06	0.17	0.14	0.11	0.11	5.31	0.23	0.20	0.20	32.24
40792.....	0.10	0.05	0.05	0.63	0.13	0.07	0.05	0.10	0.17	0.11	0.10	2.99	0.62	0.62	0.63	33.81
40818.....	0.06	0.03	0.03	0.73	0.09	0.01	0.05	0.26	0.07	0.05	0.05	2.52	0.24	0.20	0.20	31.30
40822.....	0.14	0.09	0.09	0.95	0.18	0.11	0.07	0.48	0.16	0.09	0.09	1.69	0.21	0.17	0.17	9.76
40845.....	0.17	0.12	0.05	0.38	0.35	0.15	0.06	0.28	0.21	0.15	0.08	2.03	0.25	0.21	0.17	11.87
40877.....	0.04	0.02	0.02	0.14	0.05	0.02	0.03	0.07	0.07	0.06	0.06	5.73	5.65	5.63	5.63	...
40882.....	0.25	0.21	0.06	0.43	0.25	0.18	0.08	0.40	0.31	0.27	0.10	2.69	0.51	0.50	0.44	28.04
40901.....	0.07	0.06	0.04	0.37	0.12	0.09	0.05	0.31	0.15	0.13	0.11	4.20	0.19	0.18	0.18	18.79

however, a large dispersion in all cases. In Figure 27, an illustration of HDF galaxies and their high spatial frequency component are presented.

## 5. GALAXY SIMULATIONS

To check the robustness of the metric scale and high-frequency power as a function of redshift, simulations of galaxy images at redshifts comparable to the galaxies in the HDF are constructed. The simulated images are also compared with an independent study.

It has been found that some *HST* galaxies that elude the traditional Hubble classification scheme have morphologies similar to local galaxies observed in the rest frame *UV* (Bohlin et al. 1991; Giavalisco et al. 1996). This result is not surprising since the *UV* at 2500 Å maps onto the *V* band at  $z = 1$  and onto the *I* band at  $z = 2$ . However, given that in the HDF 62% of the galaxies that are brighter than  $B_{450} = 25$  mag have redshifts in the range  $0.2 < z \leq 1$  (see Fig. 25), the *V* and *I* HDF images sample rest frame energies at  $\sim 4500$  Å. This suggests that the *VI* data of intermediate redshift galaxies should be compared with the *B*-band data of local galaxies. In the simulations I present here, the F300W and F450W images were not considered because, compared to the rest frame 4500 Å, they correspond to a shorter wavelength range (*UV*) in the rest frame of the galaxy. However, the results of such an experiment can be found in the investigations of Bohlin et al. (1991) and Giavalisco et al. (1996) who used *UV* images of nearby galaxies.

In addition to band shifting, it has been argued that cosmological effects tend to accentuate regions with high-

contrast features (Abraham et al. 1996a; Colley et al. 1996; Ellis 1997). The effects of band shifting and decrease in signal will be explored in this section. One effect that is not considered in these simulations is the presence of an increased number of young stars in high-redshift galaxies. This effect will change the structure of galaxies; however, the goal of these simulations is to investigate the minimum number of parameters that can reproduce what is observed at high redshift. The luminosity evolution will be included in future studies.

### 5.1. Method

To simulate *V*- and *I*-band images of galaxies at the redshifts of the HDF galaxies, *B*-band images of 38 nearby galaxies from the KPNO and CDI samples discussed in § 2.1.1 were artificially redshifted. The simulations include the redshift effects of surface brightness dimming and decrease in angular size; however, no evolutionary models are considered. The aim is to test how different galaxies look if only instrumental and redshift effects are accounted for.

Given the transmission curves of the *B*-band filter (Barden, De Veny, & Carder 1993) and of the *HST* band filters (Biretta 1996) the *B*-band images are roughly mapped onto the *V* band at  $z = 0.35$  and onto the *I* band at  $z = 0.9$ . However the widths of the filter bands do not exactly map onto each other. A redshift of  $z = 0.5$  will map the *B* band between the *V* and *I* bands.

In what follows, I present a description of the procedures to simulate the appearance of a galaxy at redshift  $z$  observed with the *HST*/WFPC2 at a given signal-to-noise

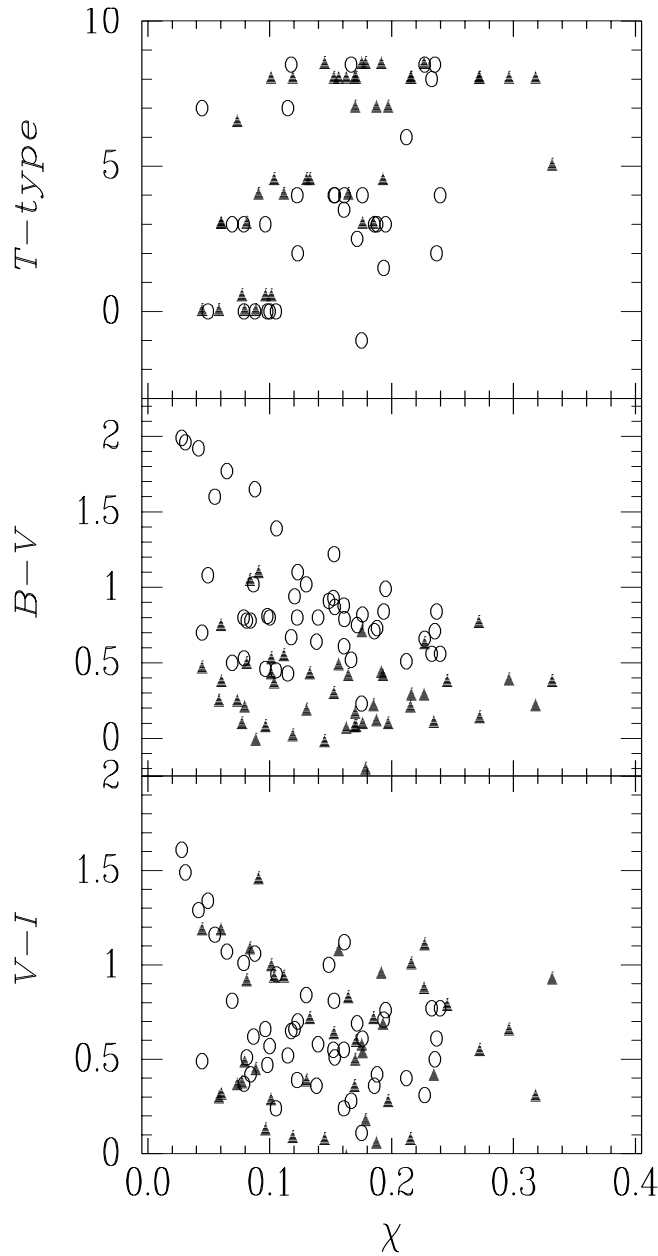


FIG. 26.—Comparison of  $\chi$  between morphological types and optical colors in the HDF. The data are a subset of the HDF sample with redshifts smaller than  $z < 1.2$ . The open circles are galaxies with  $z < 0.8$  and the filled triangles are galaxies with  $z \geq 0.8$ . The  $\chi$  values of the lower redshift range are from the  $V$ -band data and of the higher redshift range from the  $I$ -band data.

ratio and exposure time. The method for transforming a blue band image of a nearby galaxy into an *HST* image of a redshifted galaxy requires calibrating the flux, decreasing the intensity (surface brightness dimming and bandwidth corrections), binning of pixels, and adding noise to conform to the HDF images. The nearby galaxies used in these simulations are listed in Table 9.

The first step in the simulation process is to flux calibrate the nearby galaxy images by relating detected electrons ( $e^-$ ) to flux in *cgs* units. It is useful to keep the signal in detector units, either ADU or electrons, instead of transforming to  $\text{ergs s}^{-1} \text{cm}^{-2}$  because the response of linear devices is proportional to the number of incident photons, which is

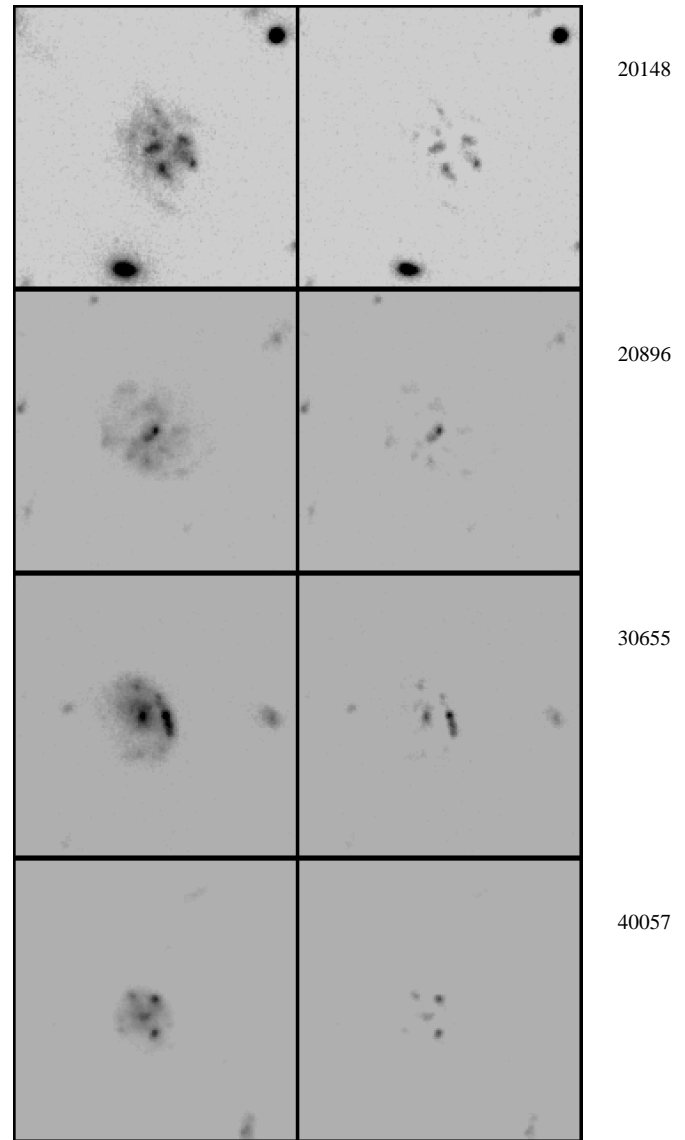


FIG. 27.—Illustration of high spatial frequency images of HDF galaxies.

basically the quantity that is followed with redshift. Let  $N$  ( $e^-$ ) be the sky-subtracted galaxy flux measured as described in § 2.1.1. It is related to the RC3 Johnson  $B$ -band magnitude via

$$B_{\text{RC3}} = -2.5 \log N + Z_0. \quad (12)$$

In essence the zero point ( $Z_0$ ) contains information of the photometric band instrumental throughput, and, to a large extent, of the atmospheric conditions at the time of observation. Since the images used in this experiment were observed under nonphotometric conditions, the calibration ( $Z_0$ ) is artificial in that the measured fluxes are forced to equal the RC3 magnitudes. The values of  $Z_0$  are presented in Table 9. Also presented in Table 9 are the sky surface brightness levels and 10 and 3  $\sigma$  surface brightness limits that were defined for the HDF data in § 2.2.

With the images properly flux calibrated, the next step in the process is to relate the number of photons received at low redshift with the number of photons expected at high redshift. The calculations will consider the instrumental sig-

TABLE 9  
SURFACE BRIGHTNESS AND ZERO POINTS

Name	$\mu_{\text{sky}}$ (mag arcsec <sup>-2</sup> )	$Z_0$ (mag)	$10 \sigma \mu_{\text{lim}}$ (mag arcsec <sup>-2</sup> )	$3 \sigma \mu_{\text{lim}}$ (mag arcsec <sup>-2</sup> )
NGC 1036.....	21.83	29.57	22.79	24.10
NGC 1569.....	21.74	29.98	22.75	24.06
NGC 2403.....	21.45	28.99	18.08	19.39
NGC 2715.....	21.65	30.29	23.14	24.45
NGC 2985.....	21.02	27.90	20.98	22.28
NGC 3031.....	20.30	27.44	21.57	22.88
NGC 3184.....	19.33	30.19	21.91	23.22
NGC 3344.....	21.57	29.13	22.21	23.52
NGC 3368.....	21.29	28.51	21.43	22.74
NGC 3486.....	21.24	29.59	22.52	23.82
NGC 3556.....	21.83	29.25	22.32	23.63
NGC 3631.....	21.37	29.56	22.49	23.79
NGC 3726.....	21.31	29.58	22.62	23.93
NGC 3810.....	21.72	30.11	22.99	24.29
NGC 3893.....	22.01	30.11	23.07	24.37
NGC 3938.....	21.85	30.05	23.06	24.37
NGC 3953.....	22.07	30.25	23.17	24.47
NGC 4030.....	21.27	30.65	23.29	24.60
NGC 4088.....	21.82	29.89	23.05	24.36
NGC 4136.....	21.55	29.81	22.89	24.20
NGC 4189.....	21.54	29.13	22.61	23.92
NGC 4254.....	21.46	29.05	22.50	23.81
NGC 4449.....	20.83	29.22	22.12	23.43
NGC 4486.....	19.86	28.97	21.68	22.98
NGC 4826.....	20.62	28.94	21.94	23.24
NGC 5248.....	21.45	29.04	22.03	23.33
NGC 5364.....	21.34	29.70	22.65	23.96
NGC 5371.....	21.62	29.47	22.42	23.73
NGC 5585.....	20.35	30.04	22.49	23.79
NGC 6015.....	21.05	30.03	22.84	24.15
NGC 6118.....	21.88	30.29	23.17	24.48
NGC 6217.....	19.44	29.02	21.26	22.57
NGC 6384.....	21.09	29.54	22.49	23.80
NGC 6412.....	19.73	28.78	21.75	23.06
NGC 6643.....	20.00	29.30	22.11	23.42
NGC 7448.....	21.70	29.22	21.69	23.00
NGC 7673.....	20.29	29.47	22.25	23.56
ARP 002.....	20.29	29.69	22.46	23.77
ARP 158.....	22.15	30.44	22.91	24.22

natures of the filters and detector in order to make a direct comparison between the HDF data and the nearby galaxy images. The number of electrons ( $\mathcal{N}$ ) detected from a source with flux  $F_v$  (ergs cm<sup>-2</sup> s<sup>-1</sup> Hz<sup>-1</sup>) is

$$\mathcal{N} = F_v t \pi \left( \frac{D}{2} \right)^2 \Delta v \frac{1}{h\nu} Q_v T_v(e^-), \quad (13)$$

where  $t$  is the exposure time in seconds,  $D$  is the diameter of the telescope in cm,  $h = 6.626 \times 10^{-27}$  ergs is Planck's constant,  $T_v$  is the transmission of the filter, and  $Q_v$  is the detector and telescope efficiency.

Given that

$$B_{\text{RC3}} = -2.5 \log (F_v / F_v^\star), \quad (14)$$

where  $F_v^\star = 4260 \text{ Jy} = 4260 \times 10^{-23} \text{ ergs s}^{-1} \text{ Hz}^{-1}$  is the flux of  $\alpha$  Lyrae in the  $B$  band of the  $UBVRI$  photometric system (Bessell 1979), the zero point can be rewritten in terms of the system's characteristics as

$$Z_0 = 2.5 \log (F_v^\star A_0), \quad (15)$$

where

$$A_i = t_i \pi \left( \frac{D_i}{2} \right)^2 \Delta v_i \frac{1}{h\nu_i} (Q_v T_v)_i. \quad (16)$$

The quantity  $A_i$  characterizes the observation with a given set of instruments, telescope, and exposure time; the subscript  $i = 0$  refers to the KPNO and Frei et al. (1996) observations; and the subscript  $i = z$  refers to the *HST*/WFPC2 simulated images. For the local sample the values of  $\log A_0 = Z_0/2.5 + 19.3706$  can be estimated from Table 9 for each of the input data. The *HST*/WFPC2 data of the HDF in the  $V$  and  $I$  bands correspond to  $\log A_z = 34.494$  and  $\log A_z = 34.181$ , respectively. The assumed parameters characterizing the filters are presented in Table 10.

Similar to equation (13), the number of electrons recorded on a pixel of size  $\theta_i$  is given by

$$n = I_v \theta_i^2 A_i (e^- \text{ pixel}^{-1}), \quad (17)$$

where  $I_v$  is the intensity per unit frequency (ergs<sup>-1</sup> cm<sup>-2</sup> Hz<sup>-1</sup> arcsec<sup>-2</sup>).

TABLE 10  
FILTER CHARACTERISTICS

Observatory Name	Filter	$\lambda_i$ (Å)	$\Delta\lambda_i$ (Å)
KPNO .....	<i>B</i>	4334	1061
Lowell .....	<i>B<sub>J</sub></i>	4614	1215
<i>HST</i> /WFPC2 .....	F606W	5935	1497
<i>HST</i> /WFPC2 .....	F814W	7921	1489

The number of electrons detected per pixel from a galaxy at low redshift ( $z = 0$ ) are

$$n(0) = I_v(z=0)\theta_0^2 A_0. \quad (18)$$

The number of electrons detected per pixel from the same galaxy but now placed at high redshift ( $z$ ) are

$$n(z) = I_v(z)\theta(z)^2 A_z, \quad (19)$$

where  $\theta(z)$  is the angle  $\theta_0$  projected at a redshift  $z$ . To obtain the number of electrons detected from a galaxy image as observed at high redshift, all there is left to do is to apply the Tolman prediction (Tolman 1934) that the surface brightness per unit frequency diminishes as  $(1+z)^{-3}$ . The intensity per unit frequency is proportional to  $(1+z)^{-3}$ :  $I_v(z) = I_v(0)(1+z)^{-3}$ . Two factors of  $(1+z)$  are due to the decrease in angular size and one factor is due to time dilation. The total intensity emitted in a finite bandwidth  $\Delta\nu(0)$ , which is received in the bandwidth  $\Delta\nu(z)$ , is then  $I(z) = I(0)(1+z)^{-4}$ .

We now return to equations (18) and (19), which relate the number of photons for low- and high-redshift sources. The intensity per unit frequency as a function of redshift is now substituted into equation (19). Finally, the ratio between the simulated number of electrons from a distant galaxies and the number of electrons from a nearby galaxy is

$$\frac{n(z)}{n(0)} = (1+z)^{-3} \left[ \frac{\theta(z)}{\theta_0} \right]^2 \frac{A_z}{A_0}. \quad (20)$$

When using equation (20) two assumptions are made. One assumption previously discussed is the redshift range in which these simulations are valid. In practice the redshifts are constrained by the filter characteristics. Since the zero redshift galaxies are observed through *B*-band filters [ $\lambda(0) \sim 4500$  Å] and the high-redshift galaxies are observed through the *V* and *I* bands [ $\lambda(z) \sim 6000$  Å and  $\lambda(z) \sim 8000$  Å], then the relation

$$\lambda(z) = \lambda(0)(1+z); \quad (21)$$

constrains the validity of  $n(z)$  to the redshifts  $z = 0.33$  when mapping the *B* band on the *V* band and  $z = 0.77$  when mapping the *B* band on the *I* band. The second assumption in estimating the number of photons emitted by the source is that the intensity per unit frequency is well approximated by the integrated intensity divided by the filter bandpass.

$$I_v = \frac{I}{\Delta\nu}.$$

This is a reasonable approximation as long as the spectral energy distribution of the source does not change drastically beyond the rest frame bandwidth  $\Delta\nu(0)$ . For instance, in the case of active galactic nuclei, strong emission lines located right at the edges of the rest frame filter bandpasses

will be included in the simulated high-redshift galaxy images. However, if the real imaging data were obtained at the appropriate redshift but through a filter with a narrower or different shape of bandwidth such that the emission line is not contained, the comparison between the simulation and the data will be invalid.

The next step in the simulations is to resize each pixel to that of the *HST*/WFPC2. In equation (20),  $n(z)$  is the number of electrons detected per pixel. The size of this pixel refers to the projected size at a redshift  $z$  of the original pixel ( $\theta_0$ ). Each pixel  $\theta_0$  corresponds to a physical length  $R$  at a distance  $d_0$

$$\theta_0 = \frac{R}{d_0}. \quad (22)$$

At a distance  $d_z$  where redshift effects start to become important, the physical scale  $R$  will subtend an angle

$$\theta(z) = R(1+z)/d_z. \quad (23)$$

For  $q_0 \neq 0$ ,  $d_z$  can be written as

$$d_z = \frac{c}{H_0 q_0^2 (1+z)} [q_0 z + (q_0 - 1)(\sqrt{1 + 2q_0 z} - 1)]. \quad (24)$$

From equations (22), (23), and (24) it follows that

$$\theta(z) = \theta_0 \left( \frac{1+z}{1+z_0} \right)^2 \frac{d_0}{d_z}, \quad (25)$$

where the redshift of the nearby galaxy has been explicitly included ( $z_0 \sim 0$ ) and  $d_0$  and  $d_z$  are the proper distances to the galaxy at redshifts  $z_0$  and  $z$ , respectively.

To recreate the WFC data with its  $\theta_{WF} = 0''.1$  pixel size, the image is demagnified by a factor  $m$  equal to

$$m = \frac{\theta_{WF}}{\theta(z)}, \quad (26)$$

$$= \frac{\theta_{WF}}{\theta_0} \left( \frac{1+z_0}{1+z} \right)^2 \frac{d_0}{d_z},$$

where  $\theta(z)$  has been replaced with the expression in equation (25).

The summed intensity within a square of  $m \times m$  pixels is assigned to a single pixel. For example, consider a galaxy whose recessional velocity is  $v_z = 1000$  km s<sup>-1</sup>, typical of our local sample, imaged with a pixel scale  $\theta_1 = 0''.68$  pixel<sup>-1</sup>. A 1 kpc-sized length corresponds to  $10''.25$ . At a redshift of  $z = 0.35$ , the same size length maps onto an angle of  $0''.22$ . When imaging this simulated galaxy with a pixel scale  $\theta_{WF} = 0''.1$  pixel<sup>-1</sup>, on each axis the magnification factor given in equation (26) is  $m = 10.25/0.22 \times 0.1/0.68 = 6.9$  pixels. As in this example, in general the fraction  $m$  is not an integer so that the intensities within a single original pixel are interpolated given the value of the neighboring pixels. In this study the demagnification was done with the IRAF task magnify.<sup>8</sup>

<sup>8</sup> Note, however, that these models ignore the effects of blurring of the *HST* point-spread function. As expected, when convolving the simulated images with an *HST*/WFPC2 PSF the values of  $\chi$  decrease. The distribution of  $\chi - \chi_c$  has a median of 0.06, where  $\chi_c$  is the value of  $\chi$  when convolved with the *HST*/WFPC2 PSF and  $\chi$  is the value of the simulated image ignoring convolution. The dispersion amounts to  $\sigma_{\chi - \chi_c} \simeq 0.08$ .

The final step in the simulations is to add background noise. So far the simulated image is practically noiseless. Although the original data contained instrumental noise and Poisson photon noise from the source and the background, they amount to a small signal compared to that of the galaxy and are therefore neglected: it is assumed that the simulated image contains only source signal (see, however, § 5.2). To conform to the noise in the HDF data, Poisson photon noise is generated for the sky levels and exposure times measured in the HDF images with the IRAF task MKNOISE. The sky levels per  $0''.1$  pixel are  $8022e^-$  in the  $V$  band and  $5369e^-$  in the  $I$  band (Williams et al. 1997) and the readout noise is  $5e^-$  per frame. The number of frames is 103 in the  $V$  band and 58 in the  $I$  band (see Table 1). Finally, the image is converted from electrons to ADU with a gain of  $7e^- \text{ ADU}^{-1}$ .

### 5.2. Results

The method described in the previous section to transform a  $B$ -band image of a galaxy at  $z \sim 0$  into a WFC image of a galaxy at redshift  $z$  was applied to 36 galaxies from the local sample. I simulated their appearances as seen at three redshifts: 0.35, 0.5, and 0.9. At  $z = 0.35$  and  $z = 0.50$  the simulations are of images in the F606W filter for a total integration time of 30.3 hr, and at  $z = 0.90$ , in the F814W filter for 34.3 hr. An illustration of the resulting images of seven galaxies is presented in Figure 28. As expected, the simulations show the increase in the background level and the decrease in angular resolution with the most conspicu-

ous features being the cores of the galaxies. Consequently, with decreasing signal galaxies are identified and classified based largely on information contained in their cores. All have shapes that can be recognized with their original forms except for Arp 002, which is also the faintest in absolute luminosity and the closest. Galaxies like Arp 002 remain largely undetected at large redshifts unless they have higher luminosities for some reason. Unlike Arp 002, giant galaxies at high redshifts should be detectable in the HDF data if they were similar.

A useful quantity to know is the sky brightness. This is determined by measuring the median value ( $m$ ) in  $e^-$  of a source-free region in the frame:

$$\mu_{\text{sky}} = -2.5 \log (m/\theta_0^2) + Z_1. \quad (27)$$

Here  $\theta_0$  is the pixel size in arcsec pixel $^{-1}$  of the original image. The sky surface brightness values, which are shown in Table 9, provide a rough estimate of the level of the faintest features that can be recognized. The surface brightness levels and surface brightness limits vary largely from image to image, providing the range in noise shown in Figure 20. In contrast, the galaxy images in the HDF originate from a single patch in the sky and from the same set of imaging data; therefore, the quality of the distant galaxy images is more uniform compared to the simulations.

### 5.3. Comparison with Other Work

Two-dimensional simulations of the light distribution of galaxies might consider each pixel individually, correcting

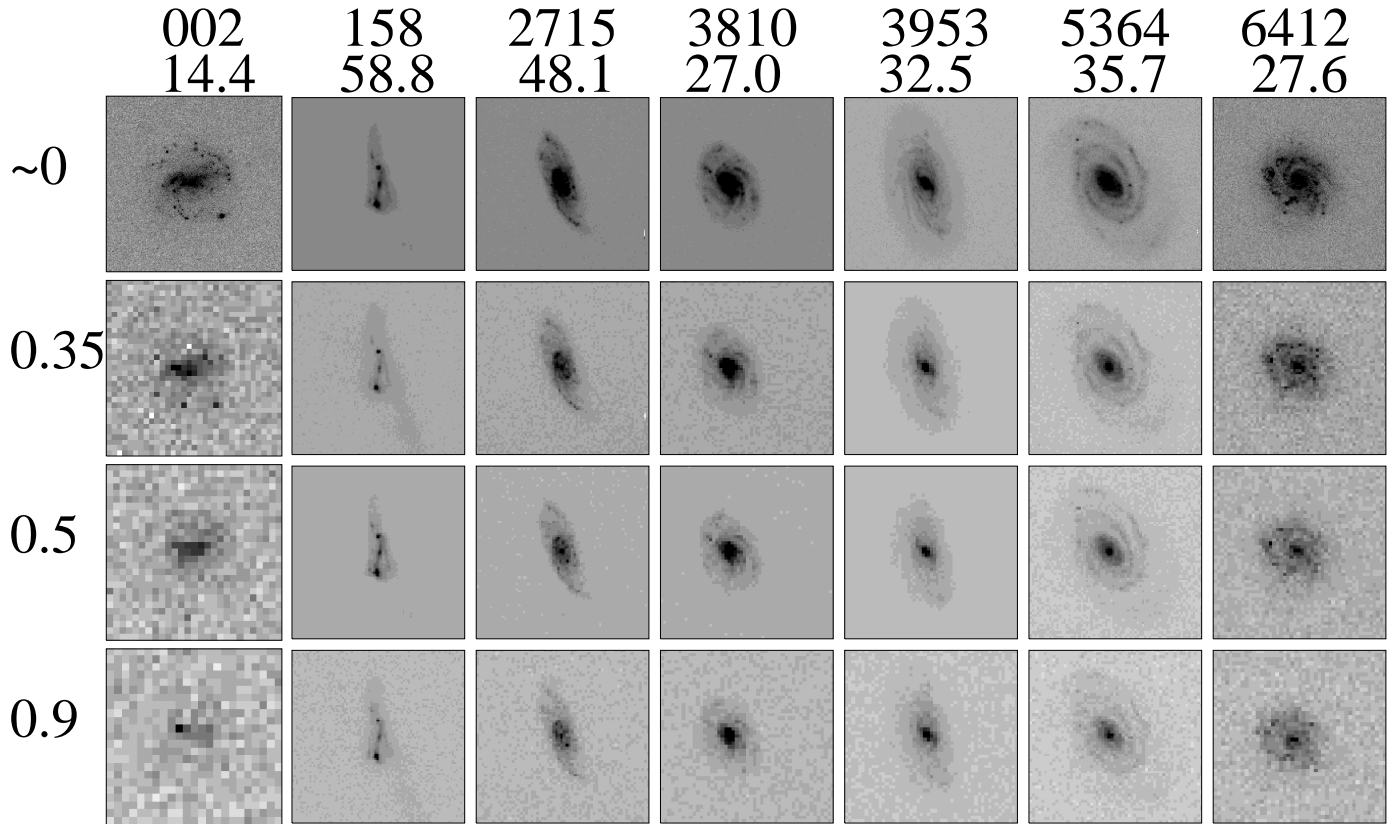


FIG. 28.—Illustration of simulated images. Each column contains a different galaxy, the number of which is indicated at the top of each column. The first two columns refer to Arp 002 and Arp 158, and the rest of the columns refer to NGC galaxies. The rows represent different redshifts that increase toward the bottom. At  $z \sim 0$  each frame covers a different size in kiloparsecs as indicated underneath each galaxy identification number. Frames of an individual galaxy and its simulations cover the same size in kiloparsecs. Black and white correspond, respectively, to the median plus four and minus five standard deviations of the background.



for the change in the spectral energy distribution if necessary. In this study, I do not consider this *selective k*-correction since the comparisons are made directly to the galaxy's  $\sim 4500 \text{ \AA}$  rest frame spectrum. However, to have an overall idea of the errors in the simulations when this correction is neglected, I compare the simulations with those of Abraham et al. (1996a, 1996b) who did consider pixel-by-pixel *k*-corrections.

The simulations are compared exclusively with those of Abraham et al. (1996a, 1996b) to keep it as straightforward as possible since we both use the same images as input for the simulations to recreate *I*-band *HST*/WFC data at redshifts in the range  $0.2 < z < 1$ . Another more practical reason is the availability of a set of simulated two-dimensional galaxy images kindly provided by R. Abraham.

Using the  $B_J$ -band data of the CDI sample of local galaxies discussed in § 2.1.1, Abraham et al. (1996b) simulate galaxy images at redshifts 0.3, 0.5, and 0.7 as observed with the WFC in the Medium Deep Survey (MDS). To conform to the MDS data, the simulations correspond to *I*-band images (F814W filter) with a total integration time of 2.8 hr and pixel scale  $0''.1$ . Each pixel in the galaxy image is treated as a separate source with its spectral energy distribution (SED) determined from the color and interpolated between a suite of SEDs for morphological types: E/S0, Sab, Sbc, and Sdm.

Following the same procedures described in § 5.1, I simulated MDS data using 20 CDI  $B_J$ -band galaxy images. Other than *K*-correction, the two sets of simulations differ from each other in the values assumed of the cosmological parameters. Abraham et al. (1996b) assume  $H_0 = 70 \text{ km s}^{-1} \text{ Mpc}^{-1}$  and  $q_0 = 0.05$ , whereas in this study  $H_0 = 65 \text{ km s}^{-1} \text{ Mpc}^{-1}$  and  $q_0 = 0.5$ . Another difference is that in this study the rest frame *B* band is simulated, whereas the simulations of Abraham et al. (1996b) are for the observed *I* band, which at the redshifts considered correspond to roughly  $6100 \text{ \AA}$  at  $z = 0.3$ ,  $5300 \text{ \AA}$  at  $z = 0.5$ , and  $4700 \text{ \AA}$  at  $z = 0.7$ . Therefore, the simulations should resemble each other the closest at  $z = 0.7$ .

Following the method outlined in § 3 the simulated galaxies' metric size and power at high spatial frequency  $\chi$  were determined and are presented, respectively, in Figures 29 and 30. The metric radius measured from the simulations done as discussed in this study [ $R_\eta(z)$ ] are consistent with the metric radius measured from the simulations of Abraham et al. (1996b) [ $R_\eta^K(z)$ ] (Fig. 29), the difference being less than 2 kpc. At the redshift range considered here, 2 kpc corresponds roughly to 1–4 WFC pixels. In the case of  $\chi$ , the difference in  $\chi^K(z) - \chi(z)$  is large compared to their values. Despite this fact, Figure 30 shows that  $\chi^K(z)$  and  $\chi(z)$  agree with each other in the sense that larger values of  $\chi^K(z)$  correspond to larger values of  $\chi(z)$ . The largest departures are for  $\chi > 0.2$  where  $\chi^K(z) < \chi(z)$ . This is consistent with the way in which the simulations were done since the SED-corrected images correspond to longer rest frame wavelengths than the simulations done without SED corrections. Consequently, the decrease of  $\chi^K(z)$  at  $z = 0.3$  and  $z = 0.5$  with respect to  $\chi(z)$  is similar to the decrease in  $\chi$  measured on local galaxy images at  $\sim 4500$  and  $\sim 7000 \text{ \AA}$  in § 3.2.2 and Figure 18. In conclusion, the metric radius is a robust quantity in that its value remains almost unaffected by whether SED corrections are considered or not. Although the high spatial frequency power is susceptible to corrections of the SED the general trend that high values of  $\chi$

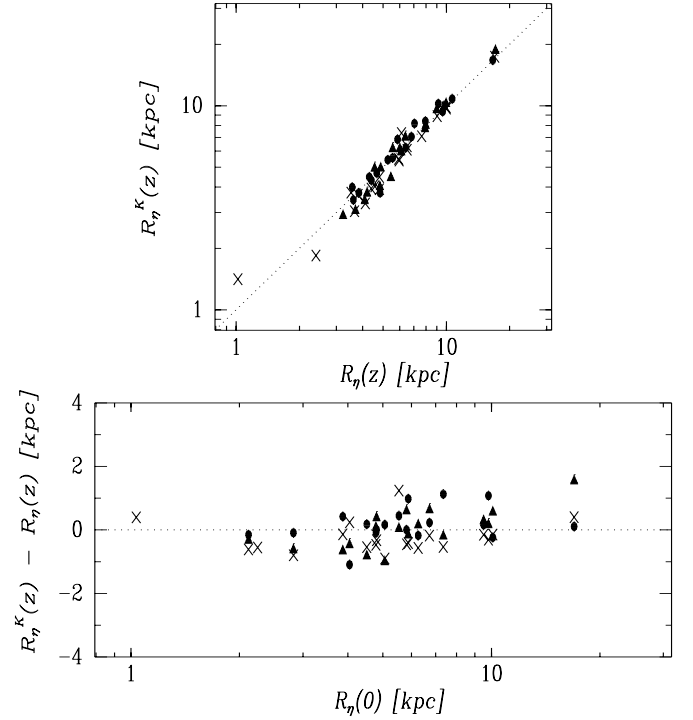


FIG. 29.—Comparison of simulations: galaxy metric sizes. Galaxies at  $z = 0.3$  (crosses),  $0.5$  (filled triangles), and  $0.7$  (filled circles) are presented. *Top*: Metric radius in kiloparsecs measured on the simulations done in this study [ $R_\eta(z)$ ] along the horizontal axis and the simulations of Abraham et al. (1996a, 1996b) assuming a pixel SED *K*-correction [ $R_\eta^K(z)$ ] along the vertical axis. The line with a slope of 1 is drawn for reference. *Bottom*:  $R_\eta(0)$  measured in the original image of the galaxy at redshift  $z \sim 0$  along the horizontal axis and the difference  $R_\eta(z) - R_\eta^K(z)$  along the vertical axis.

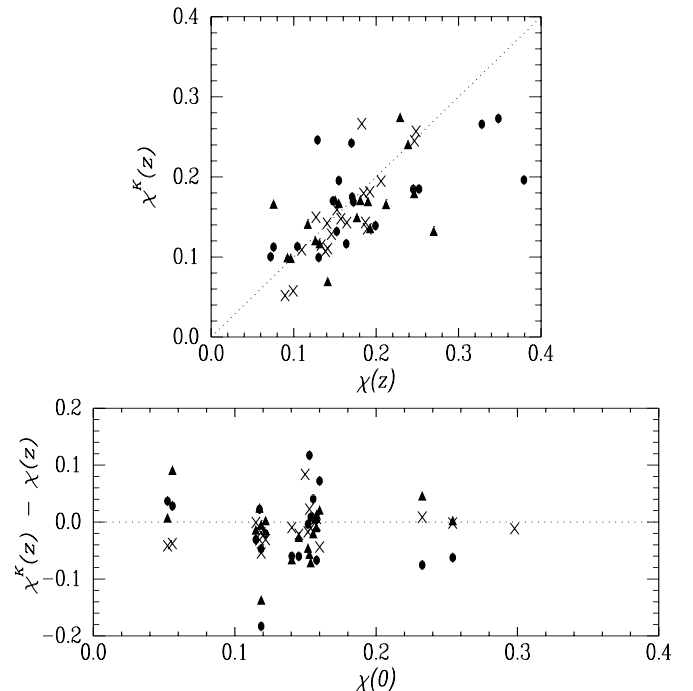


FIG. 30.—Same as Fig. 29 but the high spatial frequency power  $\chi$  is compared instead of the metric radius.

TABLE 11  
SIMULATIONS OF HDF GALAXIES

NAME (1)	$R_\eta$ (arcsec)			$\chi$		
	$z = 0.35$ (2)	$z = 0.5$ (3)	$z = 0.9$ (4)	$z = 0.35$ (5)	$z = 0.5$ (6)	$z = 0.9$ (7)
NGC 1036.....	0.20	0.30	0.10	0.15	0.35	...
NGC 2403.....	0.50	...	...	0.18	...	...
NGC 2715.....	2.30	1.70	1.60	0.17	0.15	0.17
NGC 2985.....	0.80	0.70	0.60	0.07	0.09	0.10
NGC 3031.....	0.80	0.60	0.60	0.07	0.11	0.11
NGC 3184.....	1.40	1.30	1.20	0.18	0.16	0.18
NGC 3344.....	1.10	0.90	0.80	0.18	0.19	0.08
NGC 3368.....	1.00	0.80	0.80	0.08	0.06	0.07
NGC 3486.....	0.80	0.70	0.60	0.16	0.16	0.15
NGC 3556.....	2.20	1.90	1.70	0.25	0.23	0.27
NGC 3631.....	1.20	1.10	1.30	0.16	0.16	0.16
NGC 3726.....	2.00	1.70	1.50	0.16	0.17	0.17
NGC 3810.....	1.20	1.00	0.80	0.17	0.15	0.16
NGC 3893.....	0.90	0.70	0.70	0.20	0.16	0.16
NGC 3938.....	1.40	1.20	1.00	0.17	0.15	0.16
NGC 3953.....	2.40	2.10	1.80	0.12	0.15	0.12
NGC 4030.....	1.30	1.10	1.00	0.10	0.14	0.18
NGC 4088.....	1.50	1.20	1.00	0.27	0.29	0.22
NGC 4136.....	0.80	0.70	0.60	0.14	0.19	0.21
NGC 4189.....	1.10	1.00	0.90	0.19	0.18	0.16
NGC 4254.....	1.70	1.60	1.40	0.19	0.20	0.19
NGC 4449.....	0.30	...	...	0.27	...	...
NGC 4486.....	1.10	1.00	0.80	0.02	0.03	0.03
NGC 4826.....	0.90	0.80	0.70	0.12	0.16	0.21
NGC 5248.....	1.50	1.50	1.40	0.13	0.13	0.17
NGC 5364.....	2.90	2.30	2.00	0.13	0.14	0.17
NGC 5371.....	4.50	3.90	3.40	0.12	0.12	0.11
NGC 5585.....	0.60	0.90	0.50	0.19	0.12	0.11
NGC 6015.....	1.50	1.20	1.00	0.16	0.17	0.15
NGC 6118.....	3.20	2.80	2.30	0.13	0.14	0.15
NGC 6217.....	1.40	1.20	1.20	0.18	0.22	0.23
NGC 6384.....	2.70	2.20	1.90	0.12	0.13	0.12
NGC 6412.....	1.50	1.40	1.20	0.20	0.21	0.25
NGC 6643.....	2.00	1.70	1.60	0.20	0.18	0.20
NGC 7448.....	1.70	1.50	1.40	0.18	0.19	0.21
NGC 7673.....	0.60	0.50	0.50	0.30	0.34	0.37
ARP 002.....	0.80	0.60	0.80	0.32	0.26	0.86
ARP 158.....	1.60	1.50	1.60	0.75	0.21	0.28

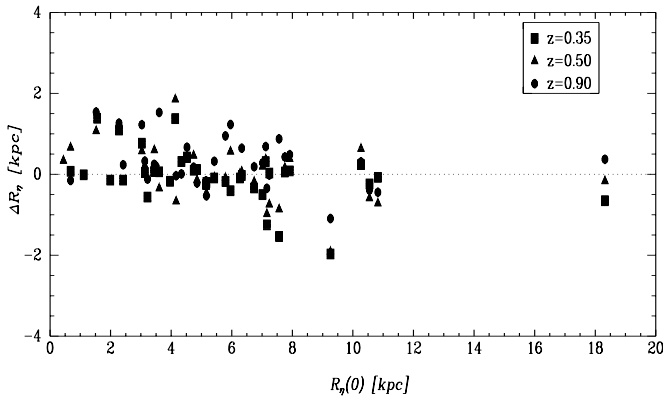


FIG. 31.—Comparison of simulations and original nearby data: metric radii. The difference  $\Delta R = R_z - R_0$  is plotted for  $z = 0.35$  (squares),  $z = 0.50$  (triangles), and  $z = 0.90$  (circles).

correspond to high values of  $\chi^K$  is still present.

#### 5.4. Hubble Deep Field

The results of simulations that reproduce HDF images of galaxies are presented in Table 11, which contains for the three redshift ranges  $z = 0.35, 0.5, 0.9$  the metric radius  $R_\eta$  in columns (2)–(4) and the power at high spatial frequencies  $\chi$  in columns (5)–(7). Note that if the *HST*/WFPC2 PSF is used, the values of  $\chi$  decrease typically by 0.06. The metric size can be recovered to better than  $\pm 2$  kpc as shown in Figure 31, which amounts to 1–4 pixels. The spread is larger with increasing redshift, and at the highest simulated redshift,  $z = 0.9$ , the distribution has an offset toward higher values in  $\Delta R$ .

It is expected that the reduced signal-to-noise ratio, relative increase in background, and cosmological surface brightness dimming tend to accentuate the visibility of high-

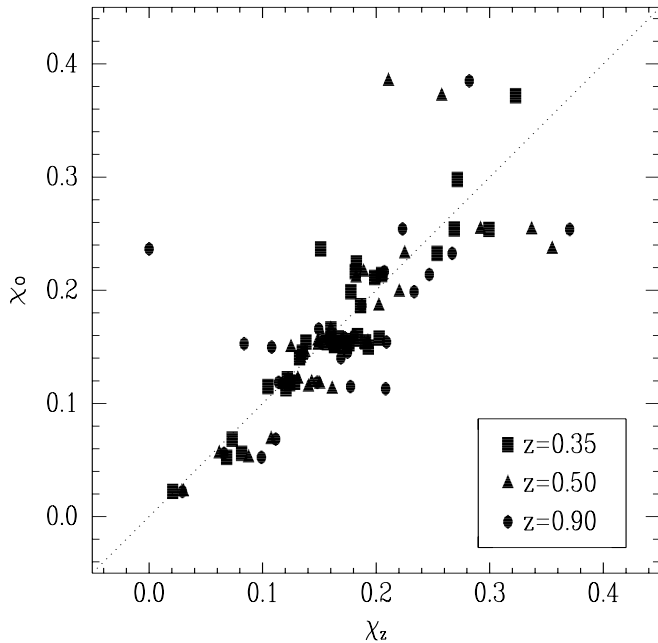


FIG. 32.—Comparison of simulations and original nearby data:  $\chi$  values. The values of  $\chi_z$  are plotted against  $\chi_o$  for  $z = 0.35$  (squares),  $z = 0.50$  (triangles), and  $z = 0.90$  (circles).

contrast features (Ellis 1997). The simulations corroborate this expectation showing that in general the values of  $\chi$  increase slightly with redshift (see Fig. 32). It is worth emphasizing that these effects will artificially increase the likelihood of identifying high-redshift galaxies as irregulars.

## 6. DISCUSSION

The purpose of the sample of nearby galaxies is to populate extensively the  $\chi$ -parameter space. It is hypothesized that the parameter  $\chi$  is related to the current star formation rate in galaxies (see Fig. 16). As expected, galaxies with small values of  $\chi$  ( $\chi \approx 0.05$ ) have red colors in the range  $0.8 \lesssim (B-V)_T^0 \lesssim 1$  and low star formation rates as traced by the equivalent widths of H $\alpha$ . On the other hand, galaxies with colors bluer than  $(B-V)_T^0 \lesssim 0.65$  and with H $\alpha$  EW  $\gtrsim 20$  Å have systematically higher values of  $\chi$  (albeit within a narrow range in  $\chi$ ,  $0.1 \lesssim \chi \lesssim 0.4$ , with a few outliers at  $\chi > 0.4$ ).

Compared to the work of Isserstedt & Schindler (1986, hereafter IS86), who find that the average value of  $\chi$  around 4500 Å<sup>9</sup> is  $\langle \chi \rangle = 0.15$  for a nearby sample of late-type spirals and irregular galaxies, in this study I find  $\langle \chi \rangle_{B_J} = 0.11$ ,  $\langle \chi \rangle_g = 0.13$ , and  $\langle \chi \rangle_B = 0.20$  in the  $B_J$ ,  $g$ , and  $B$  bands, respectively. The sample of IS86 contains spiral and irregular galaxies and is therefore comparable to the  $B$ -band and  $g$ -band data. The values of  $\chi$  in these three samples are in good agreement with each other in spite of the differences in methods and filter bands used in determining  $\chi$ .

### 6.1. Modeling $\chi$

Although in the nearby sample the dynamic range of  $\chi$  (0–0.4) is small, it is consistent with measured star formation rates and simple model predictions. The quantity that  $\chi$

measures is the ratio of luminosities of a new generation of stars ( $L_{\text{new}}$ ) and of the total stellar population ( $L_{\text{total}}$ ) at a given wavelength<sup>10</sup>

$$\chi = \frac{L_{\text{new}}}{L_{\text{total}}} . \quad (28)$$

A rough estimate of  $\chi$  can be obtained assuming the birth of a single stellar population on top of an older population of stars. The luminosity in newly born stars ( $L_{\text{new}}$ ) is simply the integral of the luminosity-weighted IMF. The total luminosity ( $L_{\text{total}}$ ) is the sum of the new and a number ( $N$ ) of older generations of stars ( $L_{\text{total}} = L_{\text{new}} + \sum_i^N L_{\text{old},i}$ ).

For the old stellar population, the contribution of the giant stars to the total luminosity can be significant. Tinsley (1980) presents values of the bolometric luminosity in giants in terms of the bolometric luminosity of dwarf stars:  $L_{\text{giant}}^{\text{bol}} = G L_{\text{dwarf}}^{\text{bol}}$ . For a stellar population that is 10 Gyr old Tinsley finds that  $G \sim 6$ . From the results of Turnrose (1976),  $G$  in the central regions of spiral galaxies in the  $V$  band is  $\sim 0.8$  in NGC 0628 and  $\sim 0.2$  in NGC 1637 and NGC 2903. Given that at shorter wavelengths giant stars contribute less to the integrated light of galaxies, to estimate  $\chi$  in the  $B$ -band, values of  $G$  lower than Tinsley's bolometric value should be considered. In Table 12 I present values of  $\chi$  for  $G$  ranging from 0 to 6 with the most likely value being  $G \lesssim 1$ . Using the IMFs of Miller & Scalo (1979) and Rana (1987), the stellar mass-luminosity relation in the  $B$  band, and assuming that all the older generations of stars have the same age, I estimate the values of  $\chi$  from

$$\chi \sim \frac{1}{1 + N(1 + G)(L_{\text{dwarf}}/L_{\text{new}})} . \quad (29)$$

Note that with this last assumption,  $G$  is a constant and  $N$  now represents the ratio of masses in the old and new stellar populations. The age of the old stellar population is only used to set the upper mass limit in the luminosity function integral of  $L_{\text{dwarf}}$ . The results are presented in Table 12. Column (1) gives the ratio of the luminosity of dwarf to giant stars, and columns (2)–(5) give the values of  $\chi$  for a number of generations of older stars ( $N$ ).

The estimated values of  $\chi$  depend strongly on the age of the burst,  $N$ , and  $G$ , so these theoretical values should not be taken too seriously. However two conclusions can be

TABLE 12  
THEORETICAL  $\chi$  VALUES

$G$ (1)	$\chi$			
	$N = 1$ (2)	$N = 5$ (3)	$N = 10$ (4)	$N = 100$ (5)
0.5.....	0.41	0.12	0.06	0.007
1.....	0.33	0.09	0.05	0.005
2.....	0.26	0.06	0.03	0.003
3.....	0.21	0.05	0.03	0.002
5.....	0.15	0.03	0.02	0.002

<sup>9</sup> IIIa-J plates and GG385 filter

<sup>10</sup> This is true if  $L_{\text{new}}$  is distributed predominantly at high spatial frequencies and  $L_{\text{total}}$  is distributed predominantly at low spatial frequencies.

drawn from this simple calculation. First, in most cases the estimated values of  $\chi$  are in the right ball park to the measured values ( $0 \lesssim \chi \lesssim 0.4$ ). Second, in this simple approximation extreme values of  $\chi$ , i.e.,  $\chi \gtrsim 0.2$ , require extreme conditions. In other words, large values of  $\chi$  are predicted if the starburst involves large amounts of the mass of the galaxy or if the galaxy is very young.

### 6.2. Star Formation History

Following the work of IS86, we can estimate the star formation history, characterized by the ratio of the current star formation rate to the past star formation rate averaged over the age of the disk, denoted  $b$  by Scalo (1986):

$$b = \frac{\text{SFR}}{\langle \text{SFR} \rangle}.$$

The star formation rate can be expressed as

$$\text{SFR} \sim L_n(M/L)_n \tau_n^{-1},$$

where  $(M/L)_n$  is the mass-luminosity relation of a newly born population of stars up to a time  $\tau_n$  and can be estimated as

$$(M/L)_n = \frac{\int_M^m m \xi(\log m) T^* d \log m}{\int_M^m L(m) \xi(\log m) T^* d \log m},$$

where  $\xi(\log m)$  is the IMF,  $m$  is the mass,  $T^* = \tau(m)/\tau_n$  for  $\tau(m) < \tau_n$ , and  $T^* = 1$  for  $\tau(m) > \tau_n$ . For three different mass ranges  $(M/L)_n$  is given in Table 13. There are large differences in  $(M/L)_n$  depending on the adopted form of the IMF. The Miller & Scalo (MS) IMF is adopted in what follows to compare the stellar birthrates as closely as possible to that of Kennicutt et al. (1994) and IS86.

The past average star formation rate can be expressed as

$$\langle \text{SFR} \rangle = L_T(M/L)\tau^{-1},$$

where  $(M/L)$  is the mass-luminosity ratio of the galaxy (Faber & Gallagher 1979) and  $\tau$  is the age of the galaxy that is taken to be the Hubble time  $\tau = 10^{10}$  yr ( $\tau = 2/3H_0^{-1}$  Peebles 1994). Finally the  $b$  ratio can be written in terms of the quantity  $\chi$  as

$$\begin{aligned} b_\chi &= \frac{L_n}{L_T} \frac{\tau}{\tau_n} \frac{(M/L)_n}{(M/L)}, \\ &= \chi \frac{\tau}{\tau_n} \frac{(M/L)_n}{(M/L)}. \end{aligned} \quad (30)$$

The stellar birthrate from H $\alpha$  is given by (Kennicutt 1983, 1998)

$$b_{\text{H}\alpha} = \frac{L_{\text{H}\alpha}/K}{L_B(M/L)} \tau, \quad (31)$$

where  $K = 1.26 \times 10^{41}$  ergs s $^{-1}$  is a constant that relates the H $\alpha$  flux and the star formation rate ( $\text{SFR} [M_\odot \text{ yr}^{-1}] = L_{\text{H}\alpha}/K = L_{\text{H}\alpha}/1.26 \times 10^{41}$  ergs s $^{-1}$ ) and  $L_B$  is the  $B$ -band luminosity of the galaxy.

The inferred birthrates from the H $\alpha$  luminosity  $L_{\text{H}\alpha}$  and  $\chi$  can be directly compared. There are 78 galaxies in the sample of nearby galaxies with observed H $\alpha$  emission that

on average have  $\langle L_{\text{H}\alpha} \rangle = 8.5 \times 10^{40}$  ergs s $^{-1}$ ,  $\langle L_B \rangle = 3.9 \times 10^{43}$  ergs s $^{-1}$ ,  $\langle T\text{-type} \rangle = 4$ ,  $\langle M/L \rangle = 4.7$ , and  $\langle \chi \rangle = 0.14$ . The resulting birthrates using equations (30) and (31) are  $\langle b_\chi \rangle = 0.17$  and  $\langle b_{\text{H}\alpha} \rangle = 0.14$ . Despite the large uncertainties in the quantities involved in determining  $b$ , both estimates agree well with each other.

Assuming that galaxies in the CDI + KPNO sample represent the typical colors of nearby galaxies (see § 2.1.1) then locally the star formation history is approximately  $b \sim 0.6$  ( $\langle \chi \rangle = 0.13$ ). This value agrees very well with that determined by IS86 and by Kennicutt (1983).

Within the timescales of interest, the ratio  $\tau_n/(M/L)_n$  changes more slowly than  $\tau/(M/L)$ , and therefore the determination of  $b$  depends strongly on the  $M/L$  ratio of the galaxy (if galaxies are formed at the same time  $\tau$ ). Therefore to follow the evolution of star formation with cosmic time, it is clear that the  $M/L$  ratio needs to be further investigated on large samples of galaxies and at many redshifts.

The star formation history  $b$  is directly related to  $\chi/(M/L)$ . Assuming a fixed timescale  $\tau_n$  during which the star formation episode occurred, then  $b \propto \chi/(M/L)$ . The  $M/L$  ratios of the HDF galaxies are not known, and instead of assigning them based on their visual morphological classification, the product  $b(M/L)$  is considered instead of  $b$  alone.

In Figure 33, the quantity  $\chi[\propto b(M/L)]$  is shown at different redshift bins for the data (Figs. 33a–33d) and simulations (Figs. 33f and 33g). The median ( $\chi_{1/2}$ ) and quartiles of the nearby sample ( $z \sim 0$ ) and the HDF sample at different redshifts are presented in Table 14. Compared to the nearby galaxies (Fig. 33a), the HDF data within the redshift range  $z < 1.1$  (Figs. 33b and 33c) have values of  $\chi$  similar to the nearby sample. However, compared to the simulations there is a slight increase in the expected values of  $\chi$  (Figs. 33f and 33g). The simulations use a sample of the CDI + KPNO that was chosen intentionally to have large values of  $\chi$  (Fig. 33e). It was expected that this CDI + KPNO subsample represented the HDF galaxies that, as claimed elsewhere (Driver et al. 1995), are irregular galaxies undergoing large rates of star formation. However the HDF data at  $z \leq 1.1$  are no more flocculent than the simulated nearby sample. When including the effects of the *HST*/WFPC2 PSF of a 0.06 decrease in  $\chi$ , a better agreement exists between the HDF data and the simulations; however, the HDF data are still not more flocculent than the simulated data. Finally, HDF galaxies at higher redshifts ( $z > 1.1$ ) (Fig. 33d) have a distribution of  $\chi$  that compared to the lower redshift HDF galaxies is flatter and with a tail toward higher values of  $\chi$  (see also Fig. 25).

The nearby sample of galaxies has typically  $\chi \sim 0.12$ . The  $B$ -band data have  $\chi \sim 0.20$ , the  $B_J$ -band data  $\chi \sim 0.11$ , and the  $g$ -band data  $\chi \sim 0.13$ . For the redshift range  $z \leq 0.6$  the median  $\chi \sim 0.13$ , for the redshift range  $0.6 < z \leq 1.1$  the median  $\chi \sim 0.12$ , and for  $z \geq 1.1$  the median  $\chi \sim 0.16$ . Therefore, the HDF galaxies with  $B \leq 25$  are as flocculent as our nearby sample of galaxies.

The nearby galaxies used in the simulations having the highest values of  $\chi$  tend to be galaxies at small distances from our Galaxy (NGC 1569, NGC 2403, NGC 4449). These galaxies that fall in the category of dwarf galaxies are also the closest to us and become undetectable in the simulations at redshifts larger than 0.3 (see Table 11). Incidentally, these tend to be the galaxies with the highest star formation rates. Therefore, the lack of very high  $\chi$  values in

TABLE 13  
( $M/L$ )<sub>n</sub> RATIOS

IMF	(M/L) <sub>n</sub>		
	$m_n = 10 M_\odot$ $\tau_n = 21 \times 10^6$	$m_n = 9 M_\odot$ $\tau_n = 25 \times 10^6$	$m_n = 8 M_\odot$ $\tau_n = 30 \times 10^6$
(M/L) <sub>n</sub> MS .....	0.010	0.014	0.023
(M/L) <sub>n</sub> Rana .....	0.047	0.071	0.113

the HDF compared to the CDI + KPNO sample can be understood because a population of dwarf galaxies at high redshifts will fall below the detection limit that defines our HDF sample ( $B_{AB} \leq 25$ ).

### 6.3. Galaxy Sizes

The metric radii as a function of distance of the nearby and distant galaxy samples are plotted in Figure 34. The distances of the nearby galaxies are determined from their heliocentric velocities from the RC3 and NED.<sup>11</sup> The gal-

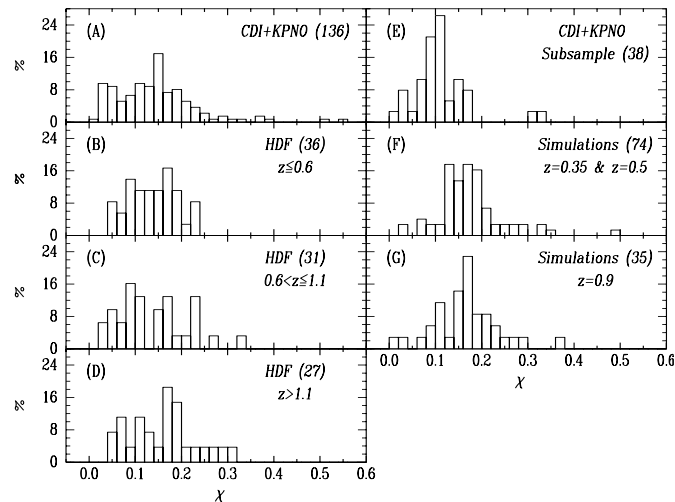


FIG. 33.—Data and simulations of  $\chi$ . Data (a)–(d) are shown on the left panels and the simulations (f) and (g) at high redshifts are shown on the right panels except for the CDI + KPNO subsample (e), which are the data used for the simulations. The data shown include (a) the nearby sample (CDI + KPNO), and the HDF galaxies within three redshift bins: (b)  $0.1 < z \leq 0.6$ , (c)  $0.6 < z \leq 1.1$ , and (d)  $z > 1.1$  as indicated. The simulations include the subsample of 38 galaxies in the CDI + KPNO at redshifts (f)  $z = 0.35$  and  $z = 0.5$  and at (g)  $z = 0.9$  as indicated. The number of galaxies in each panel is shown in parentheses.

TABLE 14

$\chi$	$\chi$			
	$z \sim 0$	$z \leq 0.6$	$0.6 < z \leq 1.1$	$z > 1.1$
$\chi_{1/2}$ <sup>a</sup> .....	0.14	0.14	0.12	0.17
$\chi_{1/4}$ <sup>b</sup> .....	0.08	0.10	0.08	0.10
$\chi_{3/4}$ <sup>c</sup> .....	0.19	0.17	0.19	0.20

<sup>a</sup> Median

<sup>b</sup> 25% of the sample have values of  $\chi$  below  $\chi_{1/4}$ .

<sup>c</sup> 75% of the sample have values of  $\chi$  below  $\chi_{3/4}$ .

<sup>11</sup> The NASA/IPAC Extragalactic Database (NED) is operated by the Jet Propulsion Laboratory, California Institute of Technology, under contract with the National Aeronautics and Space Administration.

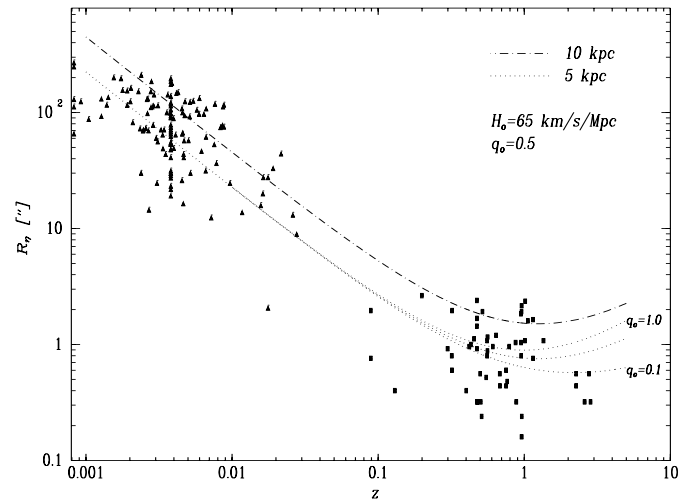


FIG. 34.—Metric radius as a function of redshift. Nearby galaxies are plotted as triangles and distant galaxies as squares. For the nearby galaxies the radii are from Tables 3, 4, 5 and as measured in the  $g$ ,  $B_J$ , and  $B$  bands, and the distances are derived from the heliocentric velocities. The distant galaxies are the filled squares and are from the  $V$  band. The clustering of data at 17 Mpc ( $z \sim 0.035$ ) are Virgo cluster galaxies. Overplotted are two reference lines corresponding to physical sizes of 5 kpc (dotted line) and 10 kpc (dot-dashed line) assuming  $H_0 = 65 \text{ km s}^{-1} \text{ Mpc}^{-1}$  and  $q_0 = 0.5$ . Also shown are the 5 kpc-sized curves for  $q_0 = 0.1$  and  $q_0 = 1.0$  as indicated.

axies with the smallest distances are often smaller than 5 kpc. As has been mentioned before, these tend to have large star formation rates, and when simulated at high redshifts they are not detected beyond redshifts  $z > 0.35$ . Most of the galaxies at redshifts between 0.2 and 0.9 have sizes between 5 and 10 kpc.

The measured sizes of distant galaxies show different distributions depending on their redshifts. If one assumes the nearby sample of galaxies as the parent population, a Kolmogorov-Smirnov test finds that the sizes of HDF galaxies with  $z \leq 0.6$  are consistent with the nearby sample. In contrast a K-S test on the HDF galaxies with  $0.6 < z < 1.1$  finds that it is consistent with the nearby sample at a 2% significance level. That is to say, the sizes of the high-redshift HDF samples are different from that of the nearby galaxy sample. This suggests that there are size selection effects at higher redshifts. The high-redshift HDF sample contains a larger number of very small and very large galaxies compared to the low-redshift samples, in both the HDF and the nearby samples.

### 6.4. Birthrates and Galaxy Sizes

The pieces of information distilled from the images of galaxies are the high spatial frequency power and the metric radius. To investigate how the flocculency is distributed among galaxies with different sizes, in Figure 35  $\chi$  is plotted against  $R_g$  in kiloparsecs. Although the nearby sample and the HDF sample are very similar, there is a notable difference among the HDF galaxies depending on their redshifts. Among the HDF galaxies with  $z \leq 0.6$ , the smallest of them tend to have larger values of  $\chi$  than the HDF galaxies with  $z > 0.6$  and in some cases the nearby galaxies. As expected, dwarf galaxies undergoing enhanced star formation rates are small but have large values of  $\chi$ . In Figure 35, the open squares indicate three nearby galaxies that are considered

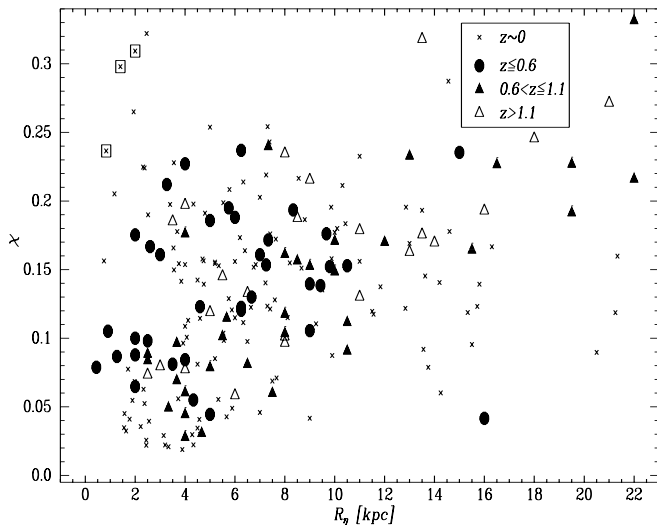


FIG. 35.—Metric radius ( $R_g$ ) and high spatial frequency power ( $\chi$ ). The small crosses are the nearby galaxies at  $z \sim 0$ , the filled circles are the HDF galaxies with redshifts  $z \leq 0.6$ , the filled triangles are the HDF galaxies with redshifts in the range  $0.6 < z \leq 1.1$ , and the open triangles are the HDF galaxies with redshifts  $z > 1.1$ . The open squares indicate examples of three nearby dwarf galaxies undergoing enhanced star formation rates: NGC 4449, NGC 1036, and NGC 7468.

prototypes of dwarf galaxies undergoing high rates of star formation. These are NGC 1569 ( $R_g, \chi$ ) = (0.3, 0.5), NGC 4449 (1.4, 0.3), NGC 1036 (0.8, 0.2), and NGC 7468 (2.0, 0.3). Few if any of the HDF galaxies populate the region delimited by these nearby dwarf galaxies, which suggests that the HDF galaxies that are more lumpy are not small. Another feature in Figure 35 is that there are no large galaxies with low values of  $\chi$ .

Allowing for different values of  $q_0$  results in at most 5%–8% of the HDF galaxies occupying the same locus as these nearby dwarf galaxies. In conclusion most of the flocculent galaxies in this sample of the HDF are not dwarfs undergoing strong bursts of star formation in their disks but can be identified instead with giant galaxies undergoing similar star formation rates as observed locally. If there exists a large population of dwarf galaxies undergoing intense star formation, they are not very flocculent.

## 7. CONCLUSIONS

The degree of flocculency  $\chi$  in galaxies can be measured with an extremely simple method based on surface photometry in one band. The method developed to measure this quantity depends on two properties of the galaxy: the size of the largest star-forming regions and the intensity profile.

The quantity  $\chi$  traces the star formation history as  $\chi$  is correlated with optical colors and H $\alpha$  EWs. A simple physical interpretation of a feature in the morphology of galaxies is achieved: flocculency has been objectively and quantitatively related to the star formation rate.

It has been claimed elsewhere that the number of irregular galaxies is larger in the HDF than what is observed locally (Driver et al. 1998). I find that only when comparing the extreme tail of the distribution in  $\chi$  does the above statement apply to the data used in this study. I find that the number of galaxies with high values of  $\chi$  in the HDF galaxies with redshifts below  $z \sim 1$  is similar to what is mea-

sured locally: the percentages of galaxies with  $\chi > 0.15$  are 46% both in the HDF galaxies with  $z \leq 1$  and in the CDI + KPNO sample (see Fig. 33 and Tables 3, 4, 5, and 8). The metric radii of the HDF galaxies with the largest values of  $\chi$  are all larger than the median of 5 kpc in the HDF, whereas for the same range in  $\chi$  the nearby galaxies have all radii in the range 5–10 kpc. These galaxies tend to have large intrinsic radii. Consistent with what Bouwens et al. (1998a, 1998b) find, the number of dwarf irregular galaxies contributing to the irregular type galaxies in the HDF is uninterestingly small.

At redshifts lower than  $z \sim 1$ , the intrinsic sizes of nearby and distant galaxies are comparable to each other. The median radius of the nearby sample is 5 kpc and the median radius of the HDF sample is 4.9 kpc. This result can be compared with the work of Roche et al. (1998), Mutz et al. (1994), and Bouwens et al. (1998a, 1998b). Consistent with our results, they find that galaxies with magnitudes brighter than  $I \lesssim 22$  and redshifts lower than  $z \lesssim 0.8$  have little if any variation of their sizes with increasing redshift and magnitude.

At redshifts higher than  $z \sim 1$ , it appears that the intrinsic sizes and  $\chi$  values are smaller than at lower redshifts. To investigate this trend, this study should be extended to fainter magnitude limits and higher redshift ranges. If this trend is confirmed, this result signifies that the brightest sources at redshifts higher than  $z \sim 1$  are compact galaxies, and if further their masses are small it will give supporting evidence for a hierarchical scenario of galaxy formation.

## 8. FUTURE WORK

The main conclusion of this study is that the HDF galaxies with redshifts  $z \lesssim 1$  do not show more flocculency than what is expected from a sample of nearby galaxies. Two-dimensional data such as multiband colors, narrow-band imaging, or integral field units if enough photons are available could in principle point out the star-forming sites and their intensities. This can resolve whether the high star formation rates inferred from the blue colors of galaxies at high redshifts are centrally concentrated (AGN) or spread throughout the disk of galaxies as we observe nearby.

At the turn of the millennium it will be possible to observe star formation processes in situ and their evolution out to look-back times when galaxies are young. These new limits will be reached when large aperture telescopes with near-infrared imaging capabilities and angular resolutions of 0".1, integral field units, and high-order adaptive optic systems are available.

To take advantage of this technologically bright future, the study of morphologies of galaxies needs further work. In this work, I have quantified a property in galaxies: the flocculency. We can easily flag objects that are flocculent, but it is difficult for us to measure its degree. There are a number of different methods that could be used to measure this same property: wavelets, pixel correlation functions, etc. In that respect, this study is meant to provide the first step in quantifying it and applying it out to high redshifts and different bandpasses.

In addition, large campaigns to measure mass distributions (e.g., DEEP) and emission-line spectra (e.g., CFRS, CNOC) out to  $z \sim 1$  are needed to verify that the imaging data and the physical processes are tied together in the same way as in the local universe. These techniques to measure the star formation rate can be extended to redshifts

as high as  $z \sim 4$  with the *Next Generation Space Telescope* (Dressler et al. 1996).

Finally, we are left with the following question: What is a good operational definition of a high-redshift galaxy? Currently, objects listed in catalogs may be a combination of high surface brightness regions, or each one of these regions may be an individual galaxy. The results of counts, color, and redshift distributions will depend on refining our ability to tackle this problem.

Support for this work was provided by the National Science Foundation through grants NSF/AURA GF-1004-95 and NSF/AURA GF-1003-96 from the Association of Universities for Research in Astronomy, Inc., under NSF Cooperative Agreement AST 89-47990, from Fundación Andes under project C-12984; by the National Science Foundation through grant 8921756 from the Space Tele-

scope Institute, which is operated by AURA, Inc., under NASA contract NAS 5-26555; and by the National Science Foundation under a cooperative agreement with the Center for Astrophysical Research in Antarctica (CARA), grant number NSF OPP 89-20223. CARA is a National Science Foundation Science and Technology Center. I am grateful to my advisor R. Kron for constant support and to K. Cudworth, J. Frieman, S. Kent, E. Kibblewhite, R. Abraham, M. Sawicki, D. Koo, J. Gallagher, B. Madore, R. Giacconi, D. Lazzati, A. Olinto, and R. Miller for helpful discussions about this work. I would like to thank the anonymous referee for very useful comments. Many thanks to L. Reams and G. Oertel, M. Roth, C. Heinz, and J. Stockstill. Special thanks to M. Mountain and F. Gillett for moral and financial support during the last stages of this work. Thanks also to my family: Anna Maria and Kazuki, Monica, Mémée and Ray, and especially Mark.

## APPENDIX

### SIZES OF STAR-FORMING REGIONS

A consistent definition of a galaxy's characteristic length is operationally important, especially if the sizes of galaxies and large H II regions within them can be expressed in terms of it. For the purposes of this study, it is reasonable to concentrate on scale lengths that are explicitly related to the star formation process in galaxies and therefore attempt to define the sizes of star-forming regions.

There is no evidence for uniformity in the sizes of H II regions. However, the typical size of the H II regions found in a given disk galaxy is correlated with the absolute luminosity of the galaxy: more luminous galaxies have larger star-forming regions (van den Bergh 1981; Kennicutt & Hodge 1984; Kennicutt 1988; Elmegreen et al. 1994). It is therefore not surprising that in Figure 36 I find that galaxies with larger characteristic lengths  $R_\eta$  have larger sizes of star-forming regions  $D_c$ . In Figure 36 the characteristic lengths are in units of kiloparsecs using the redshift values in Table 2 and  $D_c$ ; the sizes of star-forming regions are from Elmegreen et al. (1994) who measured the area of the largest regions of star formation in all the galaxies of the Sandage and Bedke Atlas of Galaxies (Sandage & Bedke 1988). The data of Figure 36 are presented in Table 15. A power-law fit of the logarithm of the metric radii to the logarithm of the sizes of star-forming complexes ( $D_c$ ) (see Table 15) is

$$D_c = 0.4R_\eta^{0.6}, \quad (\text{A1})$$

with an rms = 0.18 and a reduced  $\chi^2 = 0.18$ .

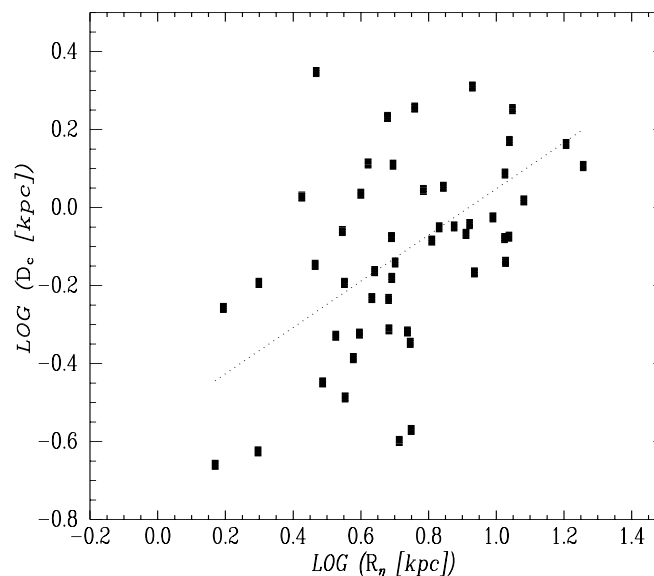


FIG. 36.—Sizes of star-forming sites  $D_c$  and metric radius  $R_\eta$ . The dotted line is the result of a linear fit through all the points. See § 3.2 for a discussion of the fit.

TABLE 15  
SIZES OF GALAXIES AND H II REGIONS

Name	Filter	$D_c$ (kpc)	$R_d$ (kpc)
NGC 1569.....	B	0.1	0.2
NGC 2403.....	B	0.6	2.0
NGC 2403.....	g	0.6	3.6
NGC 2541.....	g	0.9	3.5
NGC 2903.....	g	0.7	4.9
NGC 3031.....	g	0.6	1.6
NGC 3079.....	J	2.0	8.5
NGC 3147.....	J	1.3	4.2
NGC 3198.....	g	0.7	5.0
NGC 3319.....	g	1.1	2.7
NGC 3344.....	J	0.3	5.2
NGC 3351.....	J	0.1	3.8
NGC 3486.....	J	0.5	3.4
NGC 3596.....	J	0.5	5.5
NGC 3631.....	J	1.1	4.0
NGC 3726.....	J	1.1	7.0
NGC 3810.....	J	0.7	4.4
NGC 3893.....	J	0.6	4.3
NGC 3938.....	J	0.8	6.5
NGC 3953.....	J	0.9	8.3
NGC 4123.....	J	0.9	9.8
NGC 4136.....	J	0.3	3.6
NGC 4144.....	J	0.2	1.5
NGC 4242.....	J	0.5	4.8
NGC 4258.....	g	1.7	4.8
NGC 4303.....	g	0.5	5.6
NGC 4321.....	g	0.9	6.8
NGC 4394.....	g	0.5	3.9
NGC 4414.....	g	0.4	3.1
NGC 4487.....	J	1.1	6.1
NGC 4559.....	g	0.9	7.5
NGC 4593.....	J	1.0	12.1
NGC 4651.....	g	0.4	3.8
NGC 4725.....	g	0.8	10.6
NGC 4861.....	J	1.3	5.0
NGC 5033.....	g	2.2	2.9
NGC 5055.....	g	0.3	5.6
NGC 5204.....	J	0.2	2.0
NGC 5248.....	J	1.8	5.7
NGC 5334.....	J	0.7	10.7
NGC 5364.....	J	1.5	10.9
NGC 5371.....	J	1.3	18.1
NGC 5585.....	J	0.7	2.9
NGC 5669.....	J	0.7	8.6
NGC 5850.....	J	1.8	11.2
NGC 5985.....	J	1.5	16.1
NGC 6015.....	J	0.8	4.9
NGC 6118.....	J	0.8	10.9
NGC 6217.....	B	0.6	4.8
NGC 6384.....	J	1.2	10.6
NGC 6643.....	B	0.9	8.1

A result similar to equation (A1) can be independently derived as follows. Elmegreen et al. (1994) find that the sizes of the largest star-forming complexes are related to the absolute luminosity ( $M_B$ ) of the galaxies as

$$\log D_c = 0.178 - 0.136M_B .$$

In addition, Persic & Salucci (1991) find that the exponential disk scale length  $R_d$  is a function of the absolute luminosity:

$$R_d \simeq 6.5 \sqrt{\frac{L_B}{L_B^*}} \text{ kpc} ,$$



where  $L_B^*$  corresponds to a magnitude of  $M_B^* = -21.2$ . From the above relations, it follows that the size of the largest star-forming complex can be related to  $R_\eta$  using equation (5) evaluated at  $\eta = \frac{1}{3}$ :

$$D_c \simeq 0.16 R_\eta^{0.68}. \quad (\text{A2})$$

Equations (A1) and (A2) show that the sizes of the largest star-forming regions in a galaxy scale with the Petrosian radii as a power in the range 0.6–0.7.

## REFERENCES

- Abraham, R. G., Tanvir, N. R., Santiago, B. X., Ellis, R. E., Glazebrook, K., & van den Bergh, S. 1996a, *MNRAS*, 279, 47  
 Abraham, R. G., Valdes, F., Yee, H. K. C., & van den Bergh, S. 1994, *ApJ*, 432, 75  
 Abraham, R. G., van den Bergh, S., Glazebrook, K., Ellis, R. E., Santiago, B. X., Surma, P., & Griffiths, R. E. 1996b, *ApJS*, 107, 1  
 Arp, H. C. 1966, *ApJS*, 14, 1  
 Babul, A., & Ferguson, H. C. 1996, *ApJ*, 458, 100  
 Bahcall, J. N., & Soneira, R. M. 1980, *ApJS*, 44, 73  
 Barden, S., De Veny, J., & Carder, E. 1993, *NOAO Newsletter*, 36  
 Battistini, P., Nònoli, F., Federici, L., Fusi Pecci, F., & Kron, R. G. 1984, *A&A*, 130, 162  
 Bessell, M. S. 1979, *PASP*, 91, 589  
 Bevington, P. R. 1969, *Data Reduction and Error Analysis for the Physical Sciences* (New York: McGraw-Hill)  
 Binney, J., & Tremaine, S. 1987, *Galactic Dynamics* (Princeton: Princeton Univ. Press)  
 Biretta, J. ed. 1996, *WFPC2 Instrument Handbook*  
 Bohlin, R. C., et al. 1991, *ApJ*, 368, 12  
 Bouwens, R., Broadhurst, T., & Silk, J. 1998a, *ApJ*, 506, 557  
 ———. 1998b, *ApJ*, 506, 579  
 Burkhead, M. S., & Matuska, W. 1980, *AAS Photo. Bull.*, 23, 13  
 Busko, I. C. 1996, in *Proc. Fifth Astronomical Data Analysis Software and Systems Conference* (Tucson: Univ. Arizona Press), Vol. 101, 139  
 Buta, R. 1992, in *Proc. 27th Rencontre de Moriond, Physics of Nearby Galaxies, Nature of Nurture?*, ed. T. X. Thuan, C. Balkowski, & J. Tran Thanh Van (Gif-sur-Yvette: Editions Frontières), 3  
 Caldwell, N., Rose, J., Franx, M., & Leonardi, A. 1996, *AJ*, 111, 78  
 Calzetti, D. 1997, *AJ*, 113, 162  
 Cohen, J. G., Cowie, L. L., Hogg, D. W., Songaila, A., Blandford, R., Hu, E. M., & Shoppell, P. 1996, *ApJ*, 471, L5  
 Colley, W., Rhoads, J. E., Ostriker, J. P., & Spergel, D. N. 1996, *ApJ*, 473, L63  
 Cowie, L. L. 1996, <http://www.ifa.hawaii.edu/cowie/tts/tts.html>  
 Cowie, L. L., Hu, E. M., & Songaila, A. 1995, *AJ*, 110, 1576  
 de Vaucouleurs, G., de Vaucouleurs, A., Corwin, H. G., Buta, R. J., Paturel, G., & Fouqué, P. 1991, *Third Reference Catalogue of Bright Galaxies* (New York: Springer) (RC3)  
 de Vaucouleurs, G., & Pence, W. D. 1978, *AJ*, 83, 1163  
 Devereux, N. A., & Hameed, S. 1997, *AJ*, 113, 599  
 Devereux, N. A., & Young, J. S. 1991, *ApJ*, 371, 515  
 Djorgovski, S., & Spinrad, H. 1981, *ApJ*, 251, 417  
 Doi, M., Fukugita, M., & Okamura, S. 1993, *MNRAS*, 264, 832  
 Dressler, A., Oemler, A., Jr., Sparks, W. B., & Lucas, R. A. 1994, *ApJ*, 435, L23  
 Dressler, A., et al. 1996, *Report of The HST and Beyond Committee*, ed. A. Dressler, *Exploration and the Search for Origins: A Vision for the Ultraviolet-Optical-Infrared Space Astronomy* (Washington, DC: Association of Universities for Research in Astronomy)  
 Driver, S. P., Fernández-Soto, A., Couch, W. J., Odewahn, S. C., Windhorst, R. A., Philipps, S., Lanzetta, K., & Yahil, A. 1998, *ApJ*, 496, L93  
 Driver, S. P., Windhorst, R. A., Ostrander, E. J., Keel, W. C., Griffiths, R. E., & Ratnatunga, K. U. 1995, *ApJ*, 449, L23  
 Ellis, R. 1997, *ARA&A*, 35, 389  
 Elmegreen, B. C., & Elmegreen, D. 1990, *ApJ*, 355, 52  
 Elmegreen, D., Elmegreen, B. G., Lang, C., & Stephens, C. 1994, *ApJ*, 425, 57  
 Faber, S. M., & Gallagher, J. S. 1979, *ARA&A*, 17, 135  
 Ferguson, H. 1996, <http://www.stsci.edu/ftp/science/hdf/hdf.html>  
 Ferguson, H., & Babul, A. 1998, *MNRAS*, 196, 585  
 Frei, Z., Guhathakurta, P., Gunn, J., & Tyson, J. A. 1996, *AJ*, 111, 174  
 Gallagher, J. S., Bushouse, H., & Hunter, D. A. 1989, *AJ*, 97, 700  
 Gallagher, J. S., Hunter, D. A., & Tutukov, A. V. 1984, *ApJ*, 284, 544  
 Giallisco, M., Livio, M., Bohlin, R. C., Macchetto, D., & Stecher, T. P. 1996, *AJ*, 112, 369  
 Glazebrook, K., Ellis, R., Santiago, B., & Griffiths, R. 1995, *MNRAS*, 275, L19  
 Gullixson, C. A., Boeshaar, P. C., Tyson, J. A., & Seitzer, P. 1995, *ApJS*, 99, 281  
 Gwyn, S. D. J., & Hartwick, F. D. A. 1996, *ApJ*, 468, L77  
 Hodge, P. W. 1987, *PASP*, 99, 915  
 Hubble, E. 1926, *ApJ*, 64, 321  
 Hunter, D. A., Gallagher, J. S., & Rautenkranz, D. 1982, *ApJS*, 49, 53  
 Isserstedt, J., & Schindler, R. 1986, *A&A*, 167, 11 (IS86)  
 Jedrzejewski, R. 1987, *MNRAS*, 226, 747  
 Kauffmann, G., & Charlot, S. 1998, *MNRAS*, 294, 705  
 Kennicutt, R. C., Jr. 1983, *ApJ*, 272, 54  
 ———. 1988, *ApJ*, 334, 144  
 ———. 1992, *ApJ*, 388, 310  
 ———. 1993, in *The Environment and Evolution of Galaxies*, ed. J. M. Shull & H. A. Thronson (Dordrecht: Kluwer), 533  
 ———. 1994, *ApJ*, 344, 685  
 ———. 1998, *ApJ*, 498, 541  
 Kennicutt, R. C., Jr., & Hodge, P. W. 1984, *PASP*, 96, 944  
 Kennicutt, R. C., Jr., Tamblyn, P., & Congdon, C. W. 1994, *ApJ*, 435, 22  
 Kent, S. M. 1985, *ApJS*, 59, 115  
 Kjaergaard, P., Jorgensen, I., & Moles, M. 1993, *ApJ*, 418, 617  
 Koo, D., & Kron, R. G. 1992, *ARA&A*, 30, 613  
 Koopmann, R. A., & Kenney, J. D. P. 1998, *ApJ*, 497, L75  
 Kron, R. G. 1995, in *The Deep Universe*, ed. B. Bingeli & R. Buser (Berlin: Springer)  
 Lacey, C. G., & Fall, S. M. 1985, *ApJ*, 290, 154  
 Larson, R., & Tinsley, B. 1978, *ApJ*, 219, 46  
 Lazzati, D. 1995, *Ph.D. thesis*, Università degli Studi di Milano  
 Lowenthal, J. D., et al. 1997, *ApJ*, 481, 673  
 Manucci, F., & Beckwith, S. V. W. 1995, *ApJ*, 442, 569  
 Massey, P. 1997, *A User's Guide to CCD Reductions with IRAF*  
 Massey, P., Armandroff, T., De Veny, J., Claver, C., Harmer, C., Jacoby, G., Schoening, B., & Silva, D. 1996, *Direct Imaging Manual for Kitt Peak* (<http://www.noao.edu/kpno/docs.html>)  
 Mihalas, D., & Binney, J. 1981, *Galactic Astronomy* (San Francisco: Freeman)  
 Miller, G. E., & Scalo, J. M. 1979, *ApJS*, 41, 513  
 Morgan, W. W. 1958, *PASP*, 70, 364  
 ———. 1959, *PASP*, 71, 394  
 Morgan, W. W., & Mayall, N. V. 1957, *PASP*, 69, 291  
 Mutz, S. B., et al. 1994, *ApJ*, 434, L55  
 Naim, A., Lahav, O., Sodrè, L., Jr., & Storrie-Lombardi, M. C. 1995a, *MNRAS*, 275, 567  
 Naim, A., et al. 1995b, *MNRAS*, 274, 1107  
 O'Connell, R. W., & Marcum, P. 1997, in *HST and the High Redshift Universe*, ed. N. R. Tanvir, A. Aragón-Salamanca, & J. U. Wall (Singapore: World Scientific)  
 Odewahn, S. 1997, <http://astro.caltech.edu/sco/sco1/talks/Talks.html>  
 Odewahn, S. C., Windhorst, R. A., Driver, S. P., & Keel, W. C. 1996, *ApJ*, 472, L13  
 Okamura, S., Kodaira, K., & Watanabe, M. 1984, *ApJ*, 280, 7  
 Oke, J. B., & Gunn, J. E. 1983, *ApJ*, 266, 713  
 Osterbrock, D. E. 1989, *Astrophysics of Gaseous Nebulae and Active Galactic Nuclei*  
 Pahre, M. A., Djorgovski, S. G., & Carvalho, R. R. 1996, *ApJ*, 456, L79  
 Peebles, P. J. E. 1994, *Principles of Physical Cosmology* (Princeton: Princeton Univ. Press)  
 Persic, M., & Salucci, P. 1991, *ApJ*, 368, 60  
 Petrosian, V. 1976, *ApJ*, 210, L53  
 Quirk, W. J., & Tinsley, B. M. 1973, *ApJ*, 179, 69  
 Rana, N. C. 1987, *A&A*, 184, 104  
 Rana, N. C., & Wilkinson, D. A. 1986, *MNRAS*, 218, 497  
 Roche, N., Ratnatunga, K., Griffiths, R. E., Im, M., & Naim, A. 1998, *MNRAS*, 293, 157  
 Sandage, A. 1975, *Galaxies and the Universe, Stars and Stellar Systems IX*, ed. A. Sandage, M. Sandage, & J. Kristian (Chicago: Univ. Chicago Press), 1  
 ———. 1986, *A&A*, 161, 89  
 Sandage, A., & Bedke, J. 1988, *Atlas of Galaxies* (Washington, DC: GPO)  
 Sandage, A., & Perlmutter, J.-M. 1991, *ApJ*, 370, 455  
 Sandage, A., & Tammann, G. A. 1981, *A Revised Shapley-Ames Catalog of Bright Galaxies* (Washington, DC: Carnegie Institution)  
 Sawicki, M. J. 1997, <http://www.astro.utoronto.ca/sawicki/HDFcatalog.out>  
 Sawicki, M. J., Lin, H., & Yee, H. K. C. 1997, *AJ*, 113, 1  
 Scalo, J. M. 1986, *Fundam. Cosmic Phys.*, 11, 1  
 Schade, D., Lilly, S. J., LeFèvre, O., Hammer, F., & Crampton, D. 1996, *ApJ*, 464, 79  
 Searle, L., Sargent, W. L. W., & Bagnuolo, W. G. 1973, *ApJ*, 179, 427  
 Smith, L. F., Mezger, P. G., & Biermann, P. 1978, *A&A*, 66, 65  
 Steidel, C. C., Giallisco, M., Dickinson, M., & Adelberger, K. L. 1996, *AJ*, 112, 352

- Takamiya, M., Kron, R. G., & Kron, G. E. 1995, *AJ*, 110, 1083  
Tammann, G. A., Yahil, A., & Sandage, A. 1979, *ApJ*, 234, 775  
Thuan, T. X., & Gunn, J. E. 1976, *PASP*, 88, 543  
Tinsley, B. M. 1980, *Fundam. Cosmic Phys.*, 5, 287  
Tolman, R. C. 1934, *Relativity Thermodynamics and Cosmology* (Oxford: Clarendon)  
Turnrose, B. 1976, *ApJ*, 210, 33  
Valdes, F. 1982, *Faint Object Classification and Analysis System (KPNO Internal Publication)*  
van den Bergh, S. 1981, *AJ*, 86, 1464  
———. 1989, *AJ*, 97, 1556  
van den Bergh, S., Abraham, R. G., Ellis, R. S., Tanvir, N. R., Santiago, B. X., & Glazebrook, K. G. 1996, *AJ*, 112, 359  
Whitmore, B. C. 1984, *ApJ*, 278, 61  
Williams, R. E., et al. 1997, *AJ*, 112, 1335  
Yee, H. K. C. 1991, *PASP*, 103, 396